Theoretical Studies on Control and Synchronization of Coupled Nonlinear Systems

A Dissertation Presented for the
Doctor of Philosophy
Degree
The University of Tennessee, Knoxville

Niketh Shyam Nair
August 2018

Copyright © 2018 by Niketh Shyam Nair
All rights reserved.

ACKNOWLEDGEMENTS

First, I would like to thank my advisor, Dr. Yehuda Braiman, for his support, guidance, and unwavering encouragement throughout my time as his student. I have been very lucky to have an advisor who allowed and encouraged me to approach problems in my own way as well as taught me to not undervalue the results of my work. I must also thank Dr. Erik Bochove of Air Force Research Lab, who taught me never to take an equation for granted. I am grateful to Dr. Alejandro Aceves, Dr. Bo Liu, Dr. Will Ray, and Dr. Bruce MacLennan for many valuable discussions and pieces of advice. I would like to also thank Dr. William Hamel, Dr. Zhili Zhang, and Dr. Travis Humble, for being on my committee.

I would also like to thank my parents, Rekha and Shyam, and my partner, Efe, for their constant support and encouragement.

Finally, this work would not be possible without the support of the Office of Naval Research, Air Force Research Laboratory, Air Force Office of Scientific Research, HERE program of Oak Ridge National Laboratory (ORNL), SULI program of ORNL, ASTRO program of ORNL, and the Air Force Research Laboratory Scholars Program. Material and images from [1]–[4] are used with permission from SPIE, the Optical Society of America, Springer, and IEEE. Oak Ridge National Laboratory is managed by UT-Batelle, LLC for the U.S. Department of Energy under Contract DE-AC05-00OR22725. Opinions, interpretations, conclusions, and recommendations are those of the author and are not necessarily endorsed by the U.S. government.

ABSTRACT

Many natural and engineered systems—including but not limited to laser arrays, neuronal networks, and superconducting circuits—can be modeled as a set of coupled nonlinear oscillators. The generic study of collective behavior in coupled nonlinear oscillators has led to fundamental advances in a wide variety of fields. In this dissertation, we apply the study of coupled nonlinear oscillator systems to two engineering problems.

We study the conditions necessary to passively phase lock large arrays of semiconductor diodes in a scalable design. We approach this problem from two angles. First, we develop a novel coupled mode theory model for the electric field in a compound resonator made up of an array of waveguides of non-uniform lengths coupled using an external cavity. Second, we use and extend Master Stability Function (MSF) theory to find the stability of approximately synchronous states of arrays of weakly coupled semiconductor lasers, modeled using the Lang-Kobayashi equations. We show that if the external cavity can be represented using a decayed non-local coupling network, it may be possible to synchronize arrays of hundreds or thousands of lasers. We also present a novel derivation of the Lang-Kobayashi equations from the first-principles coupled mode theory model that we have developed. Finally, we show how our extension of MSF theory can be applied to more general coupled oscillator networks and even to a model for associative memory in neural networks.

We present new designs and design principles for ternary cryogenic memory cells based on arrays of inductively coupled Josephson junctions. We show how reading, writing and resetting are implemented using single flux quantum (SFQ) current pulse inputs and outputs from the circuit. We further show how both destructive readout and nondestructive readout can be implemented. The memory states are based on non-local trapping of flux quanta between the junctions in the array. The states correspond to the stable fixed-point solutions of the equations of motion for the circuit.

TABLE OF CONTENTS

Chapter One Introduction 1
1.1 Motivation: Coupled nonlinear dynamical systems....1
Synchronization and other collective phenomena 1
Chapter Two Coherent beam combining of laser diode arrays 3
2.1 Motivation....3
2.2 Resonator modes of external cavity-coupled laser arrays 4
Cavity modes....6
The coupled mode model 10
Example: a waveguide array coupled through a self-Fourier cavity 13
Discussion 19
Section appendix 19
2.3 Mode selection and synchronization of coupled single-mode laser diode arrays 20
Introduction....20
Analysis and results....23
Master stability functions 25
In-phase and anti-phase synchrony 32
Conclusions 36
2.4 Derivation of the coupled Lang-Kobayashi equations from coupled mode theory 40
Deriving the Lang-Kobayashi equations using the coupled mode model....41
Conclusions 44
2.5 Transverse modes of coupled nonlinear oscillator arrays....45
Finding the transverse modes in systems with additive coupling 46
Finding the transverse modes in systems with delayed diffusive coupling...48
Application: Semiconductor lasers 49
Conclusions 56
2.6 An application to associative memory dynamics....56
Mode selection in oscillatory neuron networks 56
Associative memory model....62
Conclusion....63
Chapter Three Cryogenic computing with Josephson junctions....67
3.1 Motivation....67
3.2 Background: Josephson junctions and the model for a resistively shunted Josephson junction 67
Derivation of the Resistively Shunted Junction (RSJ) equation 68
Inductively coupled Josephson junctions 70
3.3 A ternary memory circuit 71
Memory cell operation 72
Non-destructive readout 82
Conclusions 84

Chapter Four Discussion 87
4.1 Coherent beam combining of laser diode arrays 87
4.2 Cryogenic memory circuits 88
Works cited 90
Vita 104

LIST OF TABLES

Table 2.1. Parameters of semiconductor laser model 50
Table 3.1. Properties of fixed-point states of the circuit.....76
Table 3.2. Numerically calculated access energies for all possible state transitions of the circuit. These values were calculated from WRspice simulations.....82
Table 3.3. Numerically calculated access times for all possible state transitions of the circuit. These values were calculated from WRspice simulations. 82

LIST OF FIGURES

Figure 2.1. Schematic picture of compound resonator. 7
Figure 2.2. Schematic picture of a single amplifier in the array. $A_{in,n}$ is the incoming field to the nth amplifier and $A_{out,n}$ is the outgoing field from the n th amplifier. r is the outcoupling facet reflectivity and r' is the reflectivity of the back of the amplifier. 8
Figure 2.3. Eigenvalue spectrum as a function of frequency for a self-Fourier cavity with inter-cavity spacing corresponding to a frequency of 300 THz (wavelength 1 micron) and identical 5 cm waveguides (left) and disordered waveguides with length mean 5 cm and standard deviation of 100 μm (right). 14
Figure 2.4. Eigenvalue spectrum as a function of frequency for a self-Fourier cavity with inter-cavity spacing corresponding to a frequency of 300 THz (wavelength 1 micron) and disordered waveguides with length mean 5 cm and standard deviation of 100 m and various facet reflectivity values . The same laser length set is used for each plot. 16
Figure 2.5. Leading eigenvalue magnitude of a self-Fourier cavity is plotted as a function of disorder for wavelengths of 1 m, 2 m, and 4 m. Each point is averaged from 500 randomly generated arrays. Mean laser length is 5 cm with a standard deviation 17
Figure 2.6. Synchronization of leading eigenvector as a function of disorder for wavelengths of 1 μm, 2 μm, and 4 μm. Each point is averaged from 500 randomly generated arrays. Mean laser length is 5 cm with a standard deviation σ 18
Figure 2.7. Leading mode eigenvectors (left) and array phases (right) of arrays with coupling matrices (a) , (b) , (c) , and (d) . We use here and and simulate the dynamics in the presence of noise. In the phase dynamics plot, the color represents the cosine of the phase of each laser. We observe that the synchronized clusters of the array dynamics correspond to the maxima and minima of the eigenvectors.....26
Figure 2.8. Max/min diagram for a single laser and an array of 10 lasers. The blue lines denote maximal values of the carrier number N and the red lines denote minimal values of the carrier number. The value of d_x for 10 laser array is .9. The largest eigenvalue for the 10 laser coupling matrix in this case is $\lambda_1 \approx 7.3$. So $\kappa'(\kappa^f) \approx \kappa^f * (7.3)/10$. The labeled events scale consistently in the two bifurcation plots. These plots were generated using a continuation method with steps in κ^f of $.01\text{ns}^{-1}$ with simulation time of 200ns at each step. 30
Figure 2.9. Average phase synchrony of large arrays of lasers. Each point corresponds to a simulation of delayed Lang-Kobayashi equations for diode

laser array with randomized initial conditions (we started averaging process after 800ns simulation for convergence to occur). We observe both stable CW and unstable chaotic phase synchronization of diode laser array. Lines denoting regions of effective coupling are related to the degree of synchronization in the system. For very large arrays achieving phase synchronization requires either very weak or very strong (and possibly unrealistic) coupling κ^f between the diodes in the array. 31

Figure 2.10. Projections of the attractors on the $|E|,\Delta$ plane at various points in the continuation shown in Figure 2.8 are plotted for single lasers and selected lasers within the synchronized array of lasers. For the single laser, note that $\kappa' = \kappa^f$. We also include numerical estimates for the maximal Lyapunov exponent for each attractor (calculated from the single laser dynamics during the continuation). For parts (a-c), the behavior of the single laser and the 10-laser array are almost identical. However for part (d) when the single laser is hopping between the ECM solutions, the array of lasers remains near only one of the ECM solutions. Note that these plots are taken from the continuation simulations. 33

Figure 2.11. Trajectories of $\cos\phi_j$ of an array of $M = 30$ lasers in the presence of noise coupled through the matrix $\mathbf{K}_1$ with $d_x = .8$. As $\kappa' = \kappa^f \frac{\lambda_1}{M}$ is increased, the behavior becomes more complex. In (a) we observe synchrony on the cw solution. In (b) there is quasiperiodic synchronization with a very high degree of synchrony. In (c) there is chaotic synchronization with a slightly lower but still high (above 95%) synchronization. In (d) the chaotic synchrony is still high, but is starting to become less perfect. 35

Figure 2.12. Trajectories of $\cos\phi_j$ of an array of $M = 30$ lasers in the presence of noise coupled through the matrix $\mathbf{K}_2$ with $d_x = .8$. As $\kappa' = \kappa^f \frac{\lambda_1}{M}$ is increased, the behavior becomes more complex, though with the bifurcation happening later than the same system with $\mathbf{K}_1$. In (a) and (b) we observe synchrony on the cw solution. In (c)-(f) the behavior becomes increasingly more chaotic, but maintains general antiphase behavior that corresponds to the leading $\mathbf{K}_2$ mode (i.e. the first 15 lasers are out of phase with the second 15 lasers). 37

Figure 2.13. Average synchrony $S = < \frac{|\sum_{i=1}^{M} E_i|^2}{M \sum_{i=1}^{M} |E_i(t)|^2} >$ is plotted for arrays of 10 lasers without noise with varying levels of disorder and coupling strength and with coupling decay constant $d_x = .9$. ω_i is Gaussian-distributed about zero

with standard deviation σ. The delay time is $\tau = 3\text{ns}$. Each point is averaged from 30 simulations with different randomized initial conditions and different random instances of disorder. 38
Figure 2.14. Trajectories of $\cos\phi_j$ of an array of $M = 30$ lasers in the presence of noise and disorder of $\sigma\tau = .3$ coupled through the matrix $\mathbf{K}_1$ with $d_x = .8$. In (a) we observe partial synchrony on the cw solution with non-negligible phase-mismatch. In (b) there is better synchrony on the cw solution, though the frequency to which the system has converged is much higher than in (a). In (c) there is quasiperiodic synchronization synchronization. In (d) there is higher frequency quasiperiodic synchrony. In (e), the synchrony begins to become chaotic. In (f) there is chaotic synchronization. 39
Figure 2.15. First four coupling eigenvalues λ_{1-4} as a function of d_x for a 60 laser array. For $d_x < 1$, $\lambda_1 < M$ and $\gamma^{sum} < 1$. We can see that when $d_x = 1$ the coupling matrix becomes singular and the coupling is perfectly all-to-all. 51
Figure 2.16. The first four eigenvectors of for a 60 laser array with $d_x = .3$. The horizontal axis represents the position in the array and the vertical axis is the value of the vector array entry for that laser. The modes are similar for other values of d_x. We denote the modes by an approximate wavenumber n with the leading mode (with largest in magnitude eigenvalue) being the $n = 1$ mode. Since the matrix G is a symmetric matrix, these modes are orthogonal. 52
Figure 2.17. Root loci of first four mode stability functions of a 60 laser array with and ns. denotes the eigenvalue and denotes average row sum. The eigenvalues are ordered in decreasing order. The first mode has the largest eigenvalue and the last mode has the least eigenvalue. 53
Figure 2.18. Phase plots of arrays of 60 lasers coupled by (a) $\mathbf{K}_1$, (b) $\mathbf{K}_2$, (c) $\mathbf{K}_3$, and (d) $\mathbf{K}_4$. Here, $d_x = .3$ and $\kappa^f = 10\,\text{ns}^{-1}$. The color represents phase value between 0 and 2π. Note that the convergence to the leading mode is not exact; there is just resemblance in clustering. 55
Figure 2.19. The first eigenvectors of the matrices for (a-1), (b-1), and (c-1) are shown with corresponding Hindmarsh-Rose simulations ((a-2), (b-2), and (c-2)) and the corresponding Kuramoto oscillator simulations ((a-3), (b-3), and (c-3)) using these matrices. Note that the mode structure corresponds to the number of synchronized clusters. 59
Figure 2.20. The time-series for 30 neurons are plotted with and , illustrating two-spike bursting in synchronized clusters, using the first four mode adjacency matrices , . Note that the mode structure corresponds to the number of synchronized clusters. 60
Figure 2.21. The first four eigenvectors of the matrices for (a), (b), (c) and (d) are shown with corresponding KL eigenvectors (for Hindmarsh-Rose) and (for Kuramoto) calculated from simulations. In all of these cases, the

correlation matrices are very close to singular. In fact, the only KL eigenvectors that correspond to any of the matrix eigenvectors are the dominant ones-- that is, the system selects only the leading mode; not a superposition of leading modes. 61
Figure 2.22. Initial state eigenvectors $\vec{V}_1$ and dominant Karhunen-Loeve eigenvectors for the last 10 oscillations v_1 are plotted for various numbers of imprinted memories M. The memories are randomly generated from uniform distributions of binary values. The initial vector corresponds to one of the memories. Note that in all cases, the memory remains stable, despite the distortion for $N = 100$ (d). In this case, $\text{sign}(\cos(\vec{\theta})) = \text{sign}(\vec{V}_1))$, though it is difficult to see. 64
Figure 2.23. The average classification error is shown against number of flipped bits in the initial condition (averaged over 50 trials). We can see that for up to 5 flipped bits, convergence still occurs perfectly for most values of M. Also, convergence seems to be more accurate with lower values of M. 65
Figure 3.1. State transition diagram for a trit. Red arrows correspond to the 'write 0' command, golden arrows correspond to the 'write 1' command, and blue arrows correspond to the 'write 2' command. Each state is accessible from any other state and can overwrite itself. 72
Figure 3.2. A ternary memory cell based on three inductively coupled Josephson junctions. The appropriate inputs for this circuit are SFQ pulses of 2ps width. Note that the shunt resistances specify only the *added* parallel resistances to the junctions, which include default resistance and capacitances. 73
Figure 3.3. Regions of stability are plotted for three states as the DC bias current is varied (one at a time) for each junction. The parameters we have chosen (, , and) are such that small variances in DC (on the order of) should not destabilize any state. 77
Figure 3.4. The input voltages are plotted above phases relative to that of the second junction for the command to write '0.' Writing '0' is accomplished by sending an SFQ pulse into the third junction in the circuit. The time-series are generated from WRSpice simulations. 78
Figure 3.5. The input voltages are plotted above phases relative to that of the second junction for the command to write '1.' Writing '1' is accomplished by sending an SFQ pulse into the first junction in the circuit. The time-series are generated from WRSpice simulations. 79
Figure 3.6. The input voltages are plotted above phases relative to that of the second junction for the command to write '2.' Writing '2' is accomplished by sending an SFQ pulse into the middle junction in the circuit. The time-series are generated from WRSpice simulations. 80
Figure 3.7. The input voltages are plotted above the resulting output voltages. In (a) a 2ps SFQ pulse is sent into the third junction for the write '0' command and the output is plotted for simulations with initial condition in the '0,' '1,' and '2' states. In (b) a 2ps SFQ pulse is sent into the first junction for the

write ‘1’ command and the output is plotted for simulations with initial condition in the ‘0,’ ‘1,’ and ‘2’ states. In (c) a 2ps SFQ pulse is sent into the second junction for the write ‘2’ command and the output is plotted for simulations with initial condition in the ‘0,’ ‘1,’ and ‘2’ states. 81
Figure 3.8. A ternary memory cell with NDRO is shown. Write functions and ‘0,’ ‘1,’ and ‘2,’ states are the same as in the DRO circuit, however the read function and output node is different. Reading is accomplished by sending an SFQ pulse (2ps width) into the point labeled ‘SFQ input 4.’ 83
Figure 3.9. The input voltages are plotted above phases relative to that of the second junction. In each plot, an SFQ pulse is sent into the read input node. In (a) the cell is in the ‘0’ state. In (b) the cell is in the ‘1’ state. In (c) the cell is in the ‘2’ state. Note that the states do not change when the pulse is sent. The read function is therefore non-destructive. 84
Figure 3.10. The input voltages are plotted above the resulting output voltages. In each plot, an SFQ pulse is sent into the read input node. In (a) the cell is in the ‘0’ state. In (b) the cell is in the ‘1’ state. In (c) the cell is in the ‘2’ state. Note that the resulting output voltage amplitude is different for each state. This ensures that this read function works correctly.....85

CHAPTER ONE
INTRODUCTION

1.1 Motivation: Coupled nonlinear dynamical systems

Synchronization and other collective phenomena

Systems of many connected simple dynamical units often exhibit collective or macroscopic behavior that cannot occur in any individual unit when uncoupled[5]–[7]. Such behavioral phenomena are often referred to as being 'emergent'[8]. Examples of emergent behavior include flocking and herd formation of animals[9], [10], wave pattern formation of neurons for muscle control[11], laser synchronization [12], [13] (and lasing itself[14], [15]), and possibly even consciousness in brains[16]–[19]. For such systems, the individual dynamical units often exhibit complex and high-dimensional behavior[20], [21]. In fact, in engineered complex systems such as arrays of lasers [12] and arrays of coupled Josephson junctions[22], [23], it is difficult to force the systems to come to coherent low-dimensional states. In this dissertation, we search for ways to enable or encourage low-dimensional or emergent behavior in populations of coupled complex dynamical units.

In particular, we discuss collective behavior in coupled nonlinear systems—each of the same variety—that evolve in continuous time. An individual continuous time nonlinear system can be represented by the following nonlinear differential equation

$$\frac{d\mathbf{X}}{dt} = \mathbf{F}(\mathbf{X}(t),t))$$

where $\mathbf{X}(t)$ s a vector or function that represents the state of the system and $\mathbf{F}$ is a nonlinear operator that represents the infinitesimal evolution of $\mathbf{X}$.

The word 'coupled' refers to some type of communication between the individual units in the system such that the state of one system, represented by a vector $\mathbf{X}_i$, is continuously influenced by the state of the other systems $\mathbf{X}_j$. When the systems are coupled, they can be described by the following equation (for N coupled systems):

$$\frac{d}{dt}\mathbf{X}_i = \mathbf{F}(\mathbf{X}_i) + \sum_{j=1}^{N} K_{ij}\mathbf{C}(\mathbf{X}_j,\mathbf{X}_i) \qquad (1.1)$$

where $\mathbf{X}_i$ is a vector that represents the state of the ith system, $\mathbf{C}(\mathbf{X}_j,\mathbf{X}_i)$ represents the effect of the jth system on the ith system, K_{ij} represents the

strength of interaction between the j th and i th system, and $\mathbf{F}(\mathbf{X}_i)$ is a nonlinear function that represents the evolution of the i th system. For example, if the i th system is totally unconnected to any other systems or even itself, it would evolve with dynamics $d\mathbf{X}_i / dt = \mathbf{F}(\mathbf{X}_i)$. The matrix $\mathbf{K}$ whose elements are K_{ij} can be thought of as the adjacency matrix of a network that couples the systems. Note that in some cases in this document, we discuss systems with time-delays or slight parametric disorder such that the functions $\mathbf{C}$ and $\mathbf{F}$ must be modified from the form in (1.1). However the essential form, which is a linear superposition of the self-evolution term $\mathbf{F}$ and coupling terms proportional to $K_{ij}\mathbf{C}$ is still present. An initial condition $(\mathbf{X}_1(0), \mathbf{X}_2(0), \ldots, \mathbf{X}_N(0))^T$ is of course required for this problem to be well defined.

Perhaps the earliest work done to understand the type of system in question was by C. Huygens[24] in 1665. Huygens noticed how the motion of pendulum clocks would anti-phase synchronize when they were hung from the same wooden bar. This result has been a foundational example of self-organized synchronization and also has recently been rigorously verified experimentally [25], [26]. Other historically relevant examples of synchronization include Van Der Pol's study of synchronization of triode oscillations [27], [28], Rayleigh's study of pipe organ synchrony [29]–[31], and synchronous fireflies[7], [32], [33]. Modern problems of interest that are often addressed as examples of coupled dynamical systems include neuronal/neural networks[34]–[37], power grids[38], lasers[12], [13], [39], social networks[40], ecosystems[41], chemical reactions[42], [43], and coupled Josephson junctions[22], [23].

Here, we will present two examples of engineering problems that require an understanding of how to control coupled nonlinear dynamical systems. We will show how it is possible to use dynamical systems theory to solve the engineering problems, and further how the peculiarities of the solutions could lead to results that are more general. The first example is the semiconductor laser diode array. We study the system from a basic physics perspective, show how it can be represented as a set of coupled nonlinear dynamical systems, and show how the fundamental problem of laser synchronization can be addressed using this representation. The second example is the Josephson junction array. We show how this system can be represented as a set of coupled nonlinear dynamical systems, and show how to exploit its dynamical properties to design a useful circuit.

CHAPTER TWO

COHERENT BEAM COMBINING OF LASER DIODE ARRAYS

Subsections 2.2, 2.3, 2.5, and 2.6 are edited versions of papers that were first-authored by the author of this dissertation. Section 2.2 develops a first-principles model of a general coupled laser array and a new way to find the resonator modes of the coupled laser array[1]. Section 2.3 shows how a it is possible to use a formalism from nonlinear dynamics, MSF theory, to understand how large arrays of weakly coupled semiconductor lasers can be synchronized and controlled [2]. Section 2.4 is a verification of the coupled resonator model developed in section 2.2 that shows how the coupled Lang-Kobayashi equations can be derived from the first principles model using realistic assumptions. Section 2.5 is a development of MSF theory that underlies the results presented in section 2.3 [3]. Finally section 2.6 shows how it is possible to use the modification of MSF theory presented from section 2.3 and 2.5 to develop a new model for an associative memory network using coupled nonlinear oscillators[4].

2.1 Motivation

The development of high-power (kW to MW) coherent light-sources is a fundamental problem in the directed energy industry [44]. At high power levels, the beam quality of many types of lasers is limited by thermo-optic effects that distort the beams and reduce the beam quality and hence efficiency of the lasers[44], [45]. Therefore, building single high-power lasers may not be the optimal solution for developing a high-power coherent source. Combining the beams of many low-power lasers with good beam quality is a possible solution to this problem.

Possible beam combining methods include wavelength (also known as spectral) beam combining and coherent beam combining. In wavelength beam combining, the lasers in the array operate at unique wavelengths so that their spectra do not overlap (and hence the waves do not interfere). A collimating lens, grating and out-coupling mirror are used to focus the light into a single diffraction-limited spot. This leads to a beam with high spatial brightness (brightness within a given spatial interval in the far-field), but low spectral brightness (brightness within a given spectral band). The number of beams that it is possible to combine using this method is limited by the spectral line-width of each laser [46], [47]. Wavelength beam combining has been demonstrated with up to 45 broad area laser diodes and an output power of about 216 W [48].

Coherent beam combining requires that the lasers are all at the same wavelength and that the phase of each laser is synchronized with the rest of the lasers in the array. When the beams from an array of lasers are in-phase, there

is constructive interference of the light-waves along the optical axis from the lasers, the power density along the axis scales proportionally to the square of the number of lasers N. This N^2 scaling comes from the vector addition of the beams. For a set of N complex electric fields $E_i = \Re(E_i) + i\Im(E_i)$ that are identical ($E_i = E_j = E_{single}$ for all i and j), the following relation holds:

$$I_{array} = |\sum_{i=1}^{N} E_i| = |\sum_{i=1}^{N} \Re(E_i) + i\Im(E_i)|$$

$$= \left(\sum_{i=1}^{N} \Re(E_i)\right)^2 + \left(\sum_{i=1}^{N} \Im(E_i)\right)^2 = N^2(\Re(E_i)^2 + \Im(E_i)^2) = N^2 I_{single}$$

However, it is clear from the above equation that when if lasers are out of phase, the scaling is less than ideal and $I_{array} < N^2 I_{single}$. Further, if the amplitudes of the lasers are not identical, the power scaling will also be suboptimal.

There are three primary classes of coherent beam combining methods: active feedback methods, passive phasing methods, and nonlinear optics methods. Active feedback methods involve detecting optical path-length differences between array elements in the array and modulating the phases or adjusting the position of the elements or an optical element that couples them to correct the errors [44], [49]. Passive phasing methods involve using a static external resonator or cavity to feed part of the light output of the laser array back into elements of the array in such a way that a phase-synchronous coherent state self-organizes [1], [50]–[55]. This project pertains to passive phasing technique and theory. We believe that understanding principles behind passive phasing could be useful in developing more successful active phasing techniques because passively phased states could be used as set-points for active control systems.

In this project, we study analytically and numerically the conditions necessary to passively phase lock large arrays of external cavity-coupled semiconductor laser diodes in a scalable design. By developing mathematical formalisms and performing numerical simulations, we will study how the geometry of the external cavity used for coupling can affect the collective behavior of the lasers in the array and lead to synchrony. We will further show how the principles we develop for lasers can be applied to other systems.

2.2 Resonator modes of external cavity-coupled laser arrays

Passive phasing of arrays of lasers for coherent beam combining allows for generation of high-brightness coherent beams[44]. As the number of sub-cavities increases, the differences in the lasers (such as length differences in fiber lasers)

make it difficult to find such a stable mode that corresponds to phased behavior. Although each sub-cavity has its own mode structure when uncoupled, when connected to an external cavity the mode structure is not conserved[45], [56].

Past work has treated the case of weak coupling of laser arrays to an external cavity. When the coupling between the lasers and the external cavities is sufficiently weak, it is possible to use the modes of the sub-cavities and couple them. Since each sub-cavity is only weakly coupled to the outside system, the internal mode structure is still relevant and can be used in the description of the whole systems mode structure and dynamics[12], [13], [57]–[62]. However, for strongly coupled systems the relevant mode structure is that of the whole cavity[45], [63], [64]. Whole resonator modes have been employed in describing laser arrays with transverse coupling[65]. Specifically, coupled mode theory using whole cavity modes has been used extensively in describing multi-stripe broad-area laser arrays[66]–[68], multi-core fiber lasers[69], VCSELs[70], [71], transversely coupled semiconductor lasers[72], [73], and arrays of other transversely coupled waveguides[74]–[76].

In this chapter we look at systems of lasers coupled through an external resonator with no transverse coupling. A coupled mode description including both transverse and longitudinal dynamics has been used to study such a system of two lasers[77]. Systems of N lasers have also been studied using iterated maps[78], [79]. The nonlinear Schrodinger equation has also been used to model longitudinal dynamics of N-laser systems with external coupling[50]. Also, a coupled mode description has been developed that addresses transverse behavior for fixed longitudinal modes[80].

The cavity losses are a collective property of the cavity architecture and field structure. In a compound laser structure, the cavity losses are sensitive to small frequency and phase changes in the field distribution. Therefore, in our analysis we consider the entire cavity modes. Each mode is specified by a frequency and vector of complex amplitudes. We show how these modes can be used to construct a dynamical model for a system of lasers. The cold cavity description as it is derived is valid for arrays of waveguides with non-overlapping waveguide modes. It is possible to use other types of mode coupling such as through polarization fields. We also assume a single polarization in the lasers. As an example, we look at the cold-cavity modes of an array of waveguides coupled through the self-Fourier cavity.

In subsection “Cavity Modes” we derive the round-trip propagator for the compound cavity and show how the modes are found from the propagator. In subsection “Coupled Mode Model” we show how we can use the modes of the derived propagator to define a coupled mode expansion of Maxwell's equations. In our system, the modes are coupled through interaction between the gain

medium and the fields. Finally in subsection “Example: a waveguide array coupled through a self-Fourier cavity” we treat an array of five waveguides coupled through a self-Fourier cavity and show how the mode structure changes with disorder in waveguide lengths.

Cavity modes

A schematic diagram of the laser array is shown in Figure 2.1. Each laser cavity can have a unique length and the external cavity, specified by a Green's function, is of arbitrary architecture.

We begin by considering field in the compound resonator. Let Ψ be the state-vector of the field. We can express Ψ in terms of a superposition of mode fields in each laser so that we have

$$\Psi(x,y,z,t)=\sum_j a_j(t)\psi_j(x,y,z)=\sum_j a_j(t)\begin{bmatrix}\psi_{j,1}(x,y,z)\\ \psi_{j,2}(x,y,z)\\ \vdots\\ \psi_{j,N}(x,y,z)\end{bmatrix}$$

where $\psi_j(x,y,z)$ is the j th *total* cavity mode and a_j is the j th amplitude of that mode. It is important to emphasize the fact that the total cavity mode is a mode of the *entire array* and describes behavior of each laser in the array simultaneously. The state of the n th laser in the j th mode is then $\psi_{j,n}(x,y,z)$. Each mode $\psi_j(x,y,z)$ must satisfy the Helmholtz equation and corresponding boundary conditions[45]. The boundary conditions come from the geometry of the compound resonator. We are making the assumption that each amplifier operates on a single transverse-mode. Each mode is a *vector* of N dimensions with the n th element representing the modal field of the the n th waveguide.

The Helmholtz equation gives the following eigenvalue equation at a frequency ω in the n th waveguide

$$\nabla_T^2\psi_n(x,y)+\frac{\omega^2}{c^2}n_n^2(x,y)\psi_n(x,y)=\beta_n^2\psi_n(x,y)$$

where $\psi_n(x,y,z)=\psi_n(x,y)e^{\pm i\beta_n z}$ is a mode field for the array, β_n is the modal propagation constant for the n th waveguide, $n_n(x,y)$ is the index of refraction of the n th waveguide, and ∇_T^2 is the transverse Laplace operator[81]. This is an eigenvalue equation yielding multiple solutions for $\psi_n(x,y)$ and β_n for each ω. Note that for every positive value of β_n, there is a solution of the opposite sign. The solutions may be bound or unbound. We assume that there is only one bound solution. As a solution, we obtain:

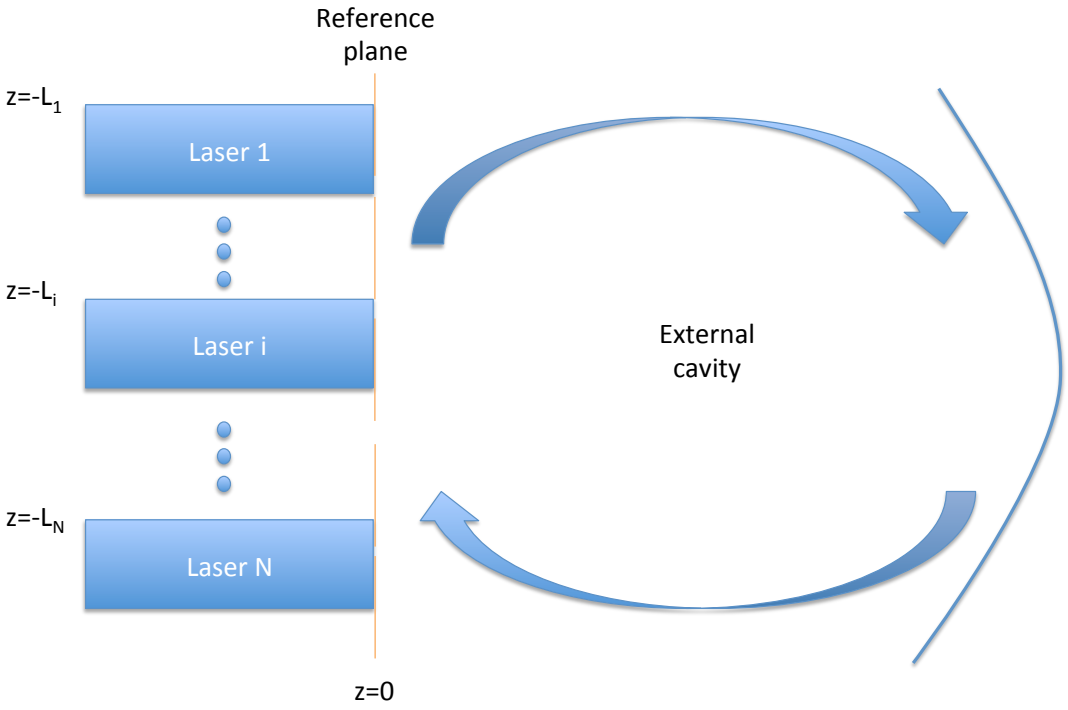


Figure 2.1. Schematic picture of compound resonator.

$$\psi_n(x,y,z) = \psi_n(x,y)[F_n e^{i\beta_n(\omega)z} + B_n e^{-i\beta_n(\omega)z}]$$

where F_n and B_n are determined from the boundary conditions at $z = -L_n$ and at $z = 0$. The solution $\beta(\omega)$ can be written as

$$\beta_n(\omega) = \frac{\omega}{c} n_{\text{eff},n}(\omega)$$

where $n_{\text{eff},n}$ is a scalar quantity representing an effective index of refraction for the sub-cavity. Since the gain bandwidth limits the range of frequencies, we can assume that $\beta_n(\omega)$ is linear in ω and let $n_{\text{eff},n}$ represent effective adjustment to the constant of proportionality.

The coefficients F_n and B_n represent the forward propagating and backward propagating parts of the mode field (respectively) and can be determined from the boundary conditions at $z = -L_n$ and at $z = 0$. We take the reference plane ($z = 0$) in this case, to be just inside of the facet of the amplifier. A schematic of this is shown in Figure 2.2.

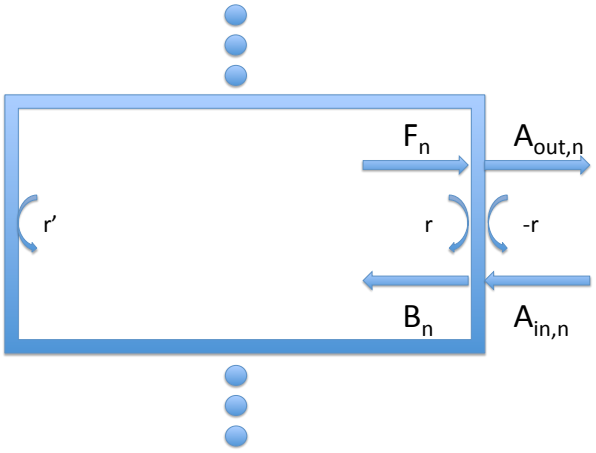


Figure 2.2. Schematic picture of a single amplifier in the array. $A_{in,n}$ is the incoming field to the n th amplifier and $A_{out,n}$ is the outgoing field from the n th amplifier. r is the outcoupling facet reflectivity and r' is the reflectivity of the back of the amplifier.

Neglecting coupling to other modes, which is consistent when deriving cold cavity modes, we obtain the relation

$$F_n e^{-i\beta_n(\omega)L_n} = r' B_n e^{i\beta_n(\omega)L_n}$$

We let $A_{\text{in},n}$ represent the amplitude of the incoming field from the out-coupler and $A_{\text{out},n}$ represent the amplitude of the outgoing field from the out-coupler, as in Figure 2.2. Solving for F_n in terms of $A_{\text{in},n}$ using the boundary conditions shown in the figure, we define the operator $\Gamma_{if}^{n}(\omega)$

$$F_n = \frac{r' + rr'}{e^{-2i\beta_n(\omega)L_n} - rr'} A_{\text{in},n} = \Gamma_{if}^{n}(\omega) A_{\text{in},n}$$

and solving for $A_{\text{out},n}$ in terms of F_n, we define the operator $\Gamma_{fo}^{n}(\omega)$

$$A_{\text{out},n} = \frac{r' - re^{-2i\beta_n(\omega)L_n}}{r' + rr'} F_n = \Gamma_{fo}^{n}(\omega) F_n.$$

This yields the single sub-cavity operator $\Gamma_n(\omega)$

$$A_{\text{out},n} = \Gamma_{fo}^{n}(\omega)\Gamma_{if}^{n}(\omega) A_{\text{in},n} = \Gamma_n(\omega) A_{\text{in},n} \tag{2.1}$$

We let coupling through the external cavity be represented by a matrix $K(\omega)$ whose mn th element represents coupling between the n th and m th laser facet. Typical derivation for $K(\omega)$ is included in the section appendix. We use this derivation for the external cavity operator

$$A_{\text{in},m} = \sum_n K_{mn}(\omega) A_{\text{out},n}.$$

For the reference plane inside the sub cavities, the full roundtrip through the system is

$$F'_m = \Gamma_{if}^{m}(\omega) \sum_{n=1}^{N} K_{mn}(\omega) \Gamma_{fo}^{n} F_n,$$

which in matrix form is

$$F' = \Gamma_{if}(\omega) K(\omega) \Gamma_{fo}(\omega) F = \Gamma_F(\omega) F \tag{2.2}$$

where $\Gamma_{fo}(\omega)$ and $\Gamma_{if}(\omega)$ are diagonal matrices whose n th entries are $\Gamma_{fo}^{n}(\omega)$ and $\Gamma_{if}^{n}(\omega)$ respectively. Also, note that $B_n = \frac{1}{r'} e^{-i\frac{2\omega n_{\text{eff},n} L_n}{c}} F_n$. So, given F, we can find B through

$$B = \Gamma_{bf}(\omega) F \tag{2.3}$$

where $\Gamma_{bf}(\omega)$ is a diagonal matrix whose n th element is $\frac{1}{r'} e^{-2i\beta_n(\omega)L_n}$.

The modes of the cavity are then determined by the set of complex frequencies $\{\omega_j\}$ that satisfy the equation using the roundtrip operator from Eq.(2.2)[82]:

$$\det(I - \Gamma_F(\omega_j)) = 0$$

The N different eigenvectors of the operator $\Gamma_F(\omega_j)$ are the forward propagating amplitudes of the mode fields for ω_j. The backwards amplitudes of the mode fields can be found using Eq.(2.3). So for each ω_j there are N eigenfunctions. To avoid over-indexing, we will let there be N values of j with the same frequency value. So the solution in the nth resonator is

$$\psi_{j,n}(x,y,z) = \psi_{j,n}(x,y)[F_{j,n}e^{i\beta_n(\omega_j)z} + B_{j,n}e^{-i\beta_n(\omega_j)z}]$$

where $\beta_n(\omega_j)$ is now complex since it is linear in ω_j. The field can then be expressed as

$$\Psi(x,y,z,t) = \sum_{j=1}^{\infty} a_j(t)\psi_j(x,y,z) = \sum_{j=1}^{\infty} \tilde{a}_j(t)e^{i\omega_j t}\psi_j(x,y,z) \tag{2.4}$$

where $\psi_j(x,y,z)$ is a vector of wave-guid modes $\psi_{j,n}(x,y,z)$ and $a_j = \tilde{a}_j(t)e^{i\omega_j t}$ so that $\tilde{a}_j(t)$ is a slowly varying amplitude envelope of the jth frequency. From Eq.(2.4), we can see that the imaginary part of ω_j represents modal loss in the cold cavity.

The coupled mode model

For a system with gain, we consider the wave wave equation for a field in the resonator:

$$\frac{n_{tot}^2}{c^2}\frac{\partial^2\Psi}{\partial t^2} = \nabla^2\Psi, \tag{2.5}$$

where n_{tot} is the complex spatio-temporal index of refraction in the active cavity and c is the speed of light[45], [81]. Since there is an array of amplifiers, each amplifier has its own time-dependent index of refraction

$$n_{tot}(x,y,z,t) = \begin{bmatrix} n_{tot}^1(x,y,z,t) & & & \\ & \ddots & 0 & \\ & 0 & \ddots & \\ & & & n_{tot}^N(x,y,z,t) \end{bmatrix}$$

$$= \begin{bmatrix} n^1(x,y,z) & & & \\ & \ddots & 0 & \\ & 0 & \ddots & \\ & & & n^N(x,y,z) \end{bmatrix} + \begin{bmatrix} \Delta n^1(x,y,z,t) & & & \\ & \ddots & 0 & \\ & 0 & \ddots & \\ & & & \Delta n^N(x,y,z,t) \end{bmatrix}$$

$$= n(x,y,z) + \Delta n(x,y,z,t)$$

where n is the cold cavity (time independent) index of refraction in the amplifier array and $\Delta n(x,y,z,t)$ is the time-dependent portion of the index of refraction. We use $n_{tot}(x,y,z,t)^2 = n^2(x,y,z) + 2n\Delta n(x,y,z,t)$, to first order in Δn. We expand Eq.(2.5) in terms of the cavity modes derived in the "Cavity Modes" subsection giving

$$\frac{1}{c^2}(n^2 + 2n\Delta n)\sum_j \frac{d^2 a_j}{dt^2}\psi_j = \sum_j a_j \nabla^2 \psi_j$$

We let $a_j = \tilde{a}_j e^{-i\omega_j t}$, where $\tilde{a}_j$ is slowly varying function of time. Since $\tilde{a}_j$ is the slowly varying component, we have that $\frac{d^2 a_j}{dt^2} \approx -(\omega_j^2 \tilde{a}_j + 2i\omega_j \frac{d\tilde{a}}{dt})e^{-i\omega_j t}$. We then obtain

$$-\frac{1}{c^2}(n^2 + 2n\Delta n)\sum_j [\omega_j^2 \tilde{a}_j + 2i\omega_j \frac{d\tilde{a}}{dt}]e^{-i\omega_j t}\psi_j = \sum_j \tilde{a}_j e^{-i\omega_j t}\nabla^2 \psi_j \,. \qquad (2.6)$$

As in the "Cavity Modes" subsection, we assume ψ_j satisfies the Helmholtz equation, $\nabla^2 \psi_j + \frac{\omega_j^2}{c^2} n^2 \psi_j = 0$. We substitute this relation into Eq.(2.6) and left multiply by $\frac{c^2}{2} n^{-1}$ (n is invertible since it is diagonal). We also eliminate terms proportional to $\Delta n \frac{d\tilde{a}}{dt}$ since both terms are small. We now obtain

$$\sum_j [i\omega_j n \frac{d\tilde{a}_j}{dt} + \Delta n \omega_j^2 \tilde{a}_j]e^{-i\omega_j t}\psi_j = 0$$

For clarity, we repeat that n and Δn are matrices and ψ_j is a vector.

Consider a vector $\phi_i = [\phi_{i,1}(x,y,z),...,\phi_{i,N}(x,y,z)]^T$. Since we assume non-overlapping waveguide fields, we can define the inner product $\phi_i^\dagger \psi_j$ as

$$\phi_i^\dagger \psi_j = \sum_{m=1}^{N} \int_{x,y} \phi_m(x,y)^* \psi_m(x,y) dA \int_z \phi_{i,m}^*(z)\psi_{j,m}(z)dz \qquad (2.7)$$

In fact, any eigenvector for a single frequency a closed resonator has a bi-orthogonal set ϕ_i for which $\phi_i^\dagger \psi_j = \delta_{ij}$ [83]. This is because for each frequency, the resonator has a complete set of eigenvectors (though perhaps with zero eigenvalues for some of the vectors). However for multiple frequencies there is no constraint of bi-orthogonality since each frequency itself has M eigenvectors of dimension N. This means that the modes of different frequencies should interact with one another even in the cold-cavity system.

Left multiplying by $\phi_i^\dagger = [\phi_{i,1}(x,y,z),...,\phi_{i,N}(x,y,z)]$ and integrating, we obtain

$$i\sum_j \frac{d\tilde{a}_j}{dt}\omega_j e^{-i\omega_j t}\int \phi_j^\dagger n\psi_j dV + \sum_j \omega_j^2 \tilde{a}_j e^{-i\omega_j t}\int \phi_j^\dagger \Delta n\psi_j dV = 0 \quad (2.8)$$

We now let C be a matrix such that $C_{ij} = \phi_i^\dagger n\psi_j$, let $Q(t)$ be a time-dependent matrix such that $Q_{ij}(t) = \phi_i^\dagger \Delta n(t)\psi_j$. Note that the indexing here is not related to frequency-- that is, there should be N indices ($j,...j+N-1$) which have the same frequency ω_j, representing the N eigenvectors corresponding to ω_j. Let $\vec{A} = [\tilde{a}_1,...,\tilde{a}_N]^T$, let Ω be a diagonal matrix whose ith element is ω_i. Then Eq.(2.8) becomes:

$$iC\Omega e^{-i\Omega t}\dot{\vec{A}}(t) = -Q(t)\Omega^2 e^{-i\Omega t}\vec{A}(t) \quad (2.9)$$

Note that the matrix $inC\Omega e^{i\Omega t}$ is not guaranteed to be invertible.

We further separate the dynamic part of the index of refraction into a real (') and imaginary (") part: $\Delta n = \Delta n' + i\Delta n''$. The imaginary part of the index of refraction is proportional to the gain in the amplifier: $\Delta n'' = -\frac{\pi c}{\omega}G$, where G is the gain[45]. The real part is proportional to the imaginary constant by the Henry constant: $\Delta n' = \alpha_H \Delta n''$ [84]. We assume saturable gain in the laser, giving

$$\Delta n^j = -(i+\alpha_H)\frac{\pi c}{\omega}G_j = -(i+\alpha_H)\frac{\pi c}{\omega}g\frac{N_j - N_0}{1+s|E_j|^2}. \quad (2.10)$$

where E_j and N_j are the total field and the number of carriers (or population inversion) in the j th amplifier respectively. In the gain saturation expression, g is the differential gain coefficient and s is the saturation coefficient. In this case, ω is a chosen central frequency. We can find the total field by the relation

$$E_j = \sum_{m=1}^{M} \tilde{a}_m(t)e^{i\omega_m t}\psi_{m,j}(x,y,z). \quad (2.11)$$

where the sum is over the modes.

The dynamics of the carriers are expressed as a simple rate equation that includes terms describing positive pump current, carrier decay, and carrier loss through stimulated emission. We can use the following equation:

$$\frac{dN_j}{dt} = J_0 - \gamma_n N_j - g\frac{N_j - N_0}{1+s|E_j|^2}|E_j|^2, \quad (2.12)$$

which is usually used to describe a semiconductor laser in the Lang-Kobayashi model[58]. The equation describes a two-level system. So, using Eqns.(2.9), (2.10), (2.11), and (2.12), we have a dynamical description of the modal interactions in the cavity. Eq.(2.9) can be written more explicitly in matrix form:

$$i\begin{bmatrix} \phi_1^\dagger n\psi_1 & \cdots & \phi_1^\dagger n\psi_M \\ \vdots & \ddots & \vdots \\ \phi_M^\dagger n\psi_1 & \cdots & \phi_M^\dagger n\psi_M \end{bmatrix}\begin{bmatrix} \omega_1 e^{-i\omega_1 t}\tilde{a}_1(t) \\ \vdots \\ \omega_M e^{-i\omega_M t}\tilde{a}_M(t) \end{bmatrix} = -\begin{bmatrix} \phi_1^\dagger \Delta n(t)\psi_1 & \cdots & \phi_1^\dagger \Delta n(t)\psi_M \\ \vdots & \ddots & \vdots \\ \phi_M^\dagger \Delta n(t)\psi_1 & \cdots & \phi_M^\dagger \Delta n(t)\psi_M \end{bmatrix}\begin{bmatrix} \omega_1^2 e^{-i\omega_1 t}\tilde{a}_1 \\ \vdots \\ \omega_M^2 e^{-i\omega_M t}\tilde{a}_M \end{bmatrix} \tag{2.13}$$

So the system of equations is a set of $M+N$ ordinary differential equations. There are M equations corresponding to the M modal amplitude envelopes and N equations corresponding to the carriers in each waveguide. The matrix operator C on the left hand side of Eq. (2.13) is the time-independent mode overlap matrix. The matrix operator $Q(t)$ on the right-hand side shows how the modes interact through the complex nonlinear time-dependent index of refraction. Note that the elements of both of these matrices are inner products as defined in Eq.(2.7). In the final set of equations, we have assumed no z dependence for the index of refraction. So Δn can be treated as a diagonal matrix of scalar complex numbers $\Delta n^n(t)$ as defined in Eq.(2.10).

Example: a waveguide array coupled through a self-Fourier cavity

The self-Fourier cavity is known to support a low-loss in-phase fundamental mode when the lasers in the array are spaced appropriately[85], [86]. The coupling matrix can be found using the method in the subsection appendix. The nm element of the matrix $K^{SF}(\omega)$ is [85]

$$K_{nm}^{SF} = \left(\frac{f}{2z_R} + \frac{zR}{2f}\right)^{-\frac{1}{2}} \exp\left(i(\theta - \frac{\pi}{4}) - \frac{\omega[4ifx_n x_m + 2z_R(x_n^2 + x_m^2)]}{4c(f^2 + z_R^2)}\right)$$

where f is the effective external cavity round-trip focal length, $z_R = \frac{1}{2}\frac{\omega}{c}w^2$ is the Rayleigh length associated with a Gaussian mode of width w and frequency ω, and $\theta = \omega f / c$ is the on-axis phase shift. The spacing between the lasers is d.

The position of the n th laser is $x_n = d(n - \frac{1}{2}(N+1))$. If the spacing is such that

$d = d_0 \equiv (f\frac{c}{\omega} + \frac{\pi^2 w^4 \omega}{fc})^{1/2}$, then the matrix element expression simplifies to [85]:

$$K_{nm}^{SF} \to \left(\frac{f}{2z_R} + \frac{z_R}{2f}\right)^{-\frac{1}{2}} \exp\left[i\left(\theta - \frac{\pi}{4}\right) - \frac{\pi z_R(n^2+m^2)}{f}\right]. \tag{2.14}$$

The matrix corresponding to Eq. (2.14) is singular [85]. Since the above simplification works only for the single frequency ω, we cannot simply assume that the coupling matrix is singular for all modes.

We now consider a self-Fourier cavity used to couple five lasers with operating frequency close to 300 THz (1 micron wavelength). At these frequencies, the

overlap of the lasers affects the properties of the cavity[85]. We use a mode width w of 7 microns. If the mode width is significantly larger at these frequencies, the singularity property of the self-Fourier cavity degrades because mode overlap becomes significant.

Our model allows us to consider the effects of disorder in the laser lengths on coherence in the lowest-loss modes of the full resonator. In order to do this, we must look at the modal amplitude envelopes just outside of the facets of the sub-cavities. These envelopes propagate in free-space to the far-field. If an envelope vector $A_{out}(\omega)$ is in-phase then the far-field is coherent. To find the set of eigenvectors A_{out} for a frequency ω we find the eigenvectors of the roundtrip operator defined by

$$\lambda A_{out}(\omega) = \Gamma_{out}(\omega) K_{SF}(\omega) A_{out}(\omega)$$

where the nn entry of Γ_{out} is the operator $\Gamma_n(\omega)$ defined in Eq. (2.1) and λ is an eigenvalue.

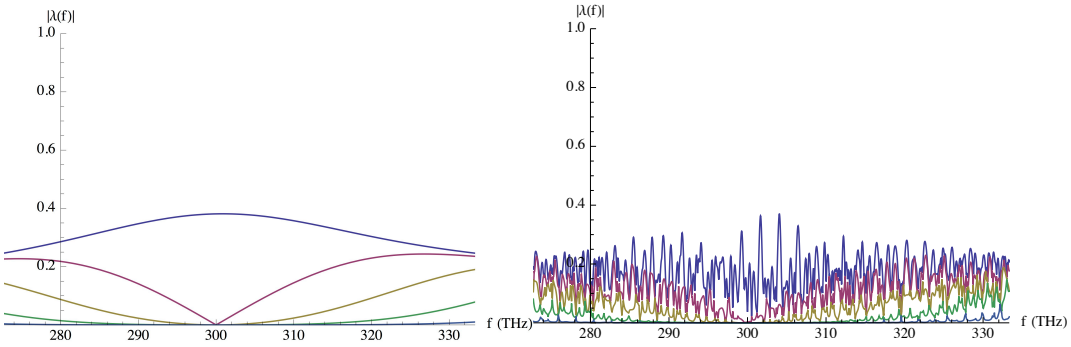


Figure 2.3. Eigenvalue spectrum as a function of frequency for a self-Fourier cavity with inter-cavity spacing corresponding to a frequency of 300 THz (wavelength 1 micron) and identical 5 cm waveguides (left) and disordered waveguides with length mean 5 cm and standard deviation of 100 μm (right).

In Figure 2.3, we show the eigenvalue spectrum as a function of frequency for a cavity with central wavelength of 1 micron and facet reflectivity r of 0 (i.e. perfect transmittance). In the ordered case (left) and the disordered case (right). The eigenvalues $\lambda_i(\omega)$ associated with the eigenvectors $A_{out,i}(\omega)$ represent corresponding losses through a round-trip. The loss through a round-trip is a factor of $1-|\lambda_i(\omega)|^2$. Since we are looking at a cavity with loss in the out-coupler, there will be loss in every mode. The central frequency for the cavity is 300 THz. When the array is disordered, the spectral dependence on frequency becomes

more complicated, however there are still frequencies very close to 300 THz with strong mode discrimination and low-loss modes.

As the facet reflectivity r is increased, the coupling between the waveguides through the external cavity becomes weaker. To understand what this means, we plot in Figure 2.4 the eigenvalue spectrum as a function of frequency for a fixed cavity with a central wavelength of 1 micron and mean length 5 cm with standard deviation of 100 microns, varying the facet reflectivity from 0 to 1. As reflectivity becomes stronger the mode structure of the disordered system becomes more like the ordered system. When reflectivity is 1 of course, the waveguides are no longer coupled to the self-Fourier cavity and the mode structure from the outside-of-facet reference plane is that of the self-Fourier cavity. However, with large non-unity values of r, the effect of disorder on the mode structure of the cavity can be mitigated.

To further understand the effect of disorder on synchronization properties, we choose the frequency ω that corresponds to the inter-cavity spacing d about which the self-Fourier cavity is defined and study the eigenvectors. In Figure 2.3 this corresponds to the lowest frequency where there is only one non-zero eigenvalue. We use frequencies with wavelengths of 1, 2 and 4 microns.

We vary the standard deviation of the disorder in the lengths between 0 and 1 micron. We show the average leading eigenvalue of such an array for the range of disorders in Figure 2.5. As the disorder increases, the leading eigenvalue quickly drops. Once disorder is sufficiently large compared to the wavelength of the lasers, the average absolute value becomes constant.

As the leading eigenvalue decreases, the synchronization level associated with the corresponding eigenvector A^*_{out} also decreases until it reaches on average a constant value. We use the Strehl ratio of the eigenvector $S(A^*_{out}) = \frac{|\sum_{i=1}^{N} A^*_{out,i}|}{\sum_{i=1}^{N} |A^*_{out,i}|}$ to determine whether the mode represents a synchronous state. Once the array is significantly disordered the first eigenvector begins to represent an asynchronous state. For a synchronous leading mode, disorder must be at least an order of magnitude smaller than the wavelength. The relationship between the level of disorder and the Strehl ratio is shown in Figure 2.6.

When the standard deviation of the lengths is larger than one tenth of the wavelength, coherence of the full cavity modes is lost. When the length difference between any two lasers becomes close to a single wavelength, relative phase differences generated in the inner cavity round-trip become non-

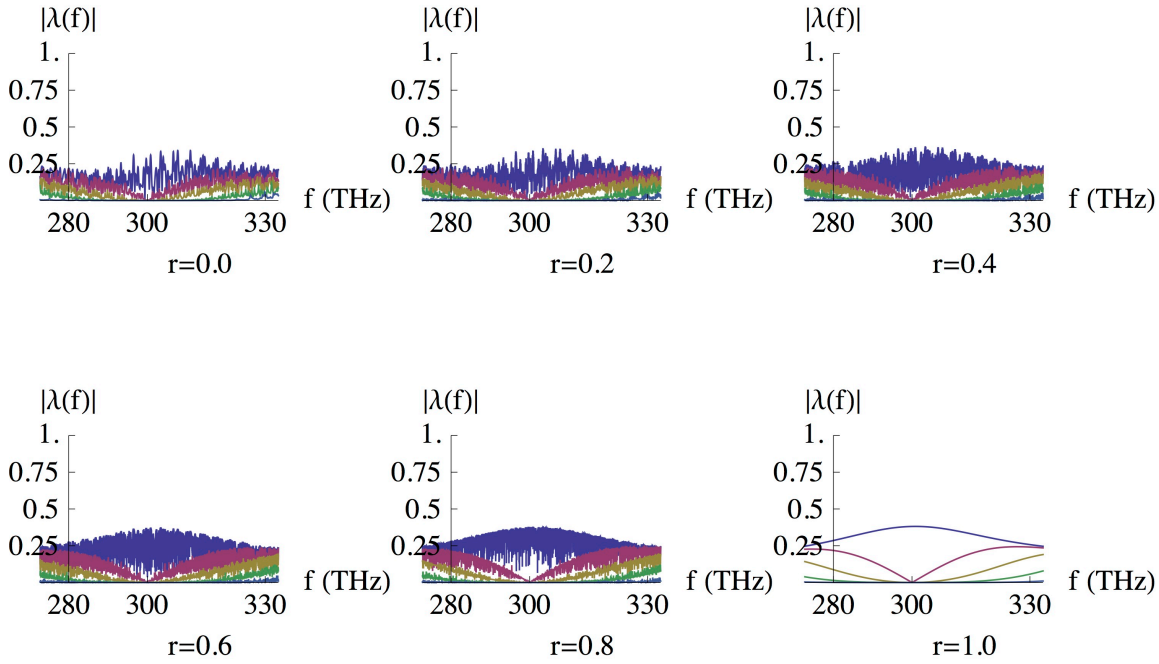


Figure 2.4. Eigenvalue spectrum as a function of frequency for a self-Fourier cavity with inter-cavity spacing corresponding to a frequency of 300 THz (wavelength 1 micron) and disordered waveguides with length mean 5 cm and standard deviation of 100 μ m and various facet reflectivity values r . The same laser length set is used for each plot.

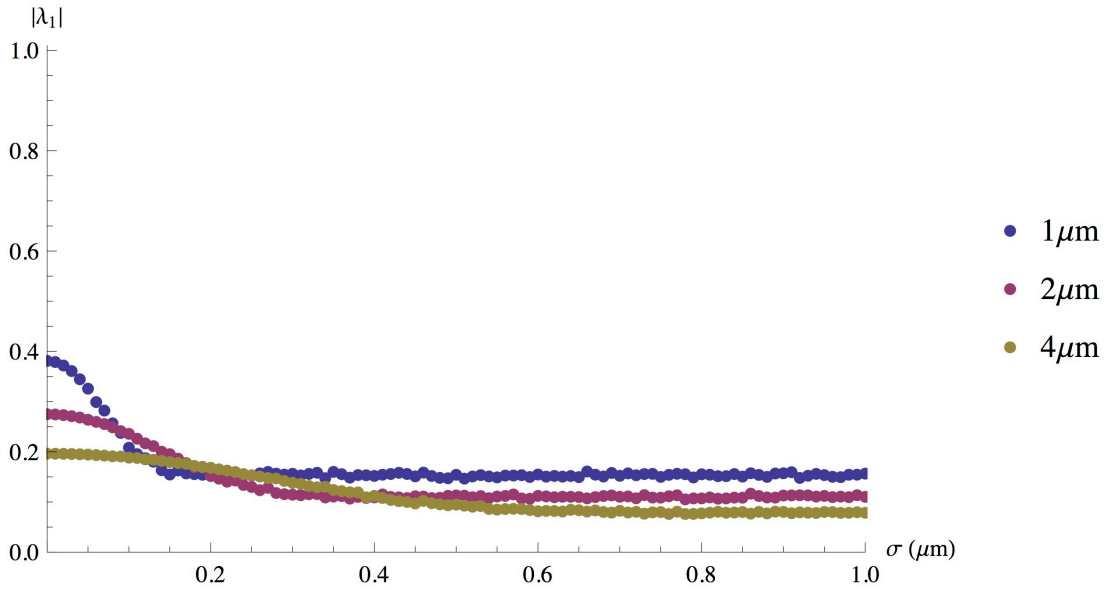


Figure 2.5. Leading eigenvalue magnitude of a self-Fourier cavity is plotted as a function of disorder for wavelengths of 1 μ m, 2 μ m, and 4 μ m. Each point is averaged from 500 randomly generated arrays. Mean laser length is 5 cm with a standard deviation σ .

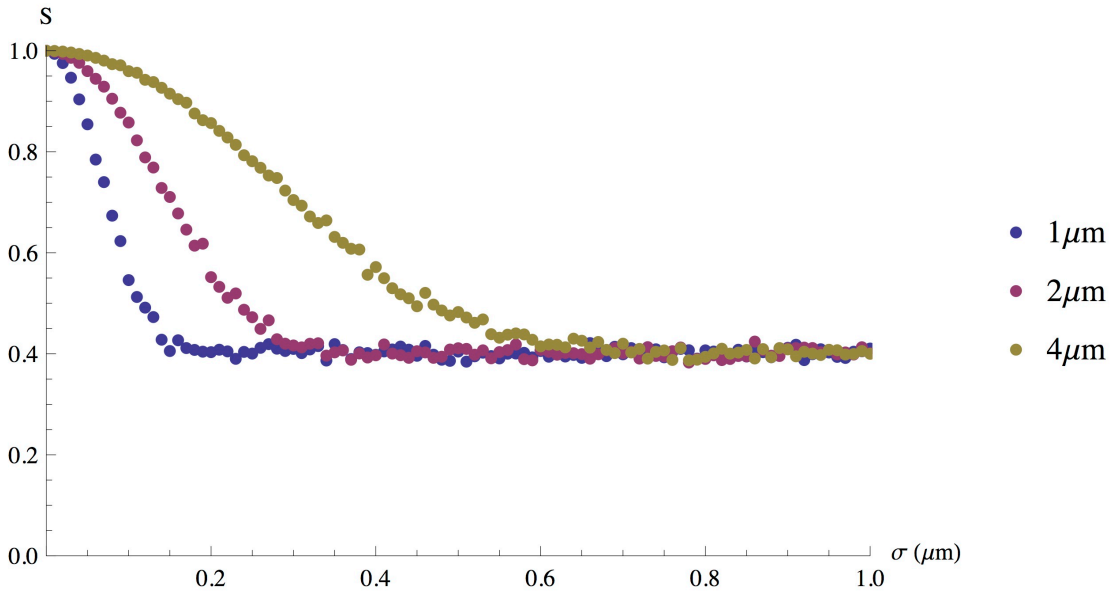


Figure 2.6. Synchronization of leading eigenvector as a function of disorder for wavelengths of 1 μm, 2 μm, and 4 μm. Each point is averaged from 500 randomly generated arrays. Mean laser length is 5 cm with a standard deviation σ.

negligible, so coherence is quickly lost. The relationship between the disorder magnitude and laser wavelength is apparent in Figure 2.6. As the wavelength increases, the cutoff in synchronization increases proportionally. We find that the amplitude envelopes of the mode fields stay the same regardless of disorder, but the phase envelopes become disordered as standard deviation of laser length increases.

Discussion

We have developed a consistent way to find cold-cavity modes for a broad class of laser arrays using Fox-Li analysis [45], [87]. In this paper, we consider an array of waveguides, but the formalism can be generalized. The formalism can also be applied to different types of gain media and overlapping mode fields. The full model (resonator modes along with the mode coupling equations) could be used to design passively phased laser arrays for coherent beam combining, to study dynamical stability, beam quality, and potentially hybrid active/passive phasing methods.

In the Coupled Mode Model section when deriving Eq.(2.8), we assume that the set of cavity modes for a particular frequency has a bi-orthogonal set. This bi-orthogonal set should be the eigenvectors of the backwards full cavity propagator at the same reference plane. Future work in this area should include a thorough investigation of the bi-orthogonality properties of the resonator modes.

We have not yet numerically simulated the dynamical coupled mode part of the model developed in the Coupled Mode Model section. This would allow us to understand the role of nonlinearity in mode coupling and in particular if there are ways to use the nonlinearity to minimize losses by compensating for the disorder through refractive index modification. This is the next step in understanding the model.

Section appendix

The external propagator maps E_{out}, the total output field of the amplifier array onto the individual inputs E_{in}. Let $E_{out}^{\omega}(x,y)$ denote the outgoing field (into the outcoupler) and let $E_{in}^{\omega}(x,y)$ denote the field going into amplifier array from the outcoupler. Let $G_{\omega}(x,y;x',y')$ denote the general Green's function such that \label{eqn:grnfncn}

$$E_{in}^{\omega}(x,y) = \iint G_{\omega}(x,y,x',y') E_{out}^{\omega}(x',y') dx' dy' . \tag{2.15}$$

This Green's function is dependent on the cavity geometry[85], [88]. For an array of lasers on a single frequency, we have $E_{out}^{\omega}(x,y)=\sum_{n=1}^{N}A_{out,n}(\omega)U_n(x,y)$ where $A_{out,n}$ is an amplitude and U_n is a transverse mode pattern. Eq. (2.15) becomes:

$$E_{in}^{\omega}(x,y)=\sum_{n=1}^{N}A_{out,n}(\omega)\iint G_{\omega}(x,y;x',y')U_n(x',y')dx'dy'$$

We let $E_{in}^{\omega}(x,y)=\sum_{n=1}^{N}A_{in,n}(\omega)U_n(x,y)$. Since we assume single transverse mode operation for all lasers, $U_n(x,y)$ represents the principal gaussian transverse mode in the n th laser. Thus we have

$$A_{in,m}(\omega)$$
$$=\sum_{n=1}^{n}A_{out,n}(\omega)\iiiint U_m(x,y)G_{\omega}(x,y;x',y')U_n(x',y')dx'dy'dxdy$$
$$=\sum_{n=1}^{N}K_{mn}(\omega)A_{out,n}(\omega)$$

where the elements of the matrix $K(\omega)$ are modal interaction integrals. Note that $A_{in,n}$ and $A_{out,n}$ are as in Figure 2.2 for the n th amplifier.

2.3 Mode selection and synchronization of coupled single-mode laser diode arrays

Introduction

Synchronization in networks of nonlinear elements has been studied for years and a variety of interesting and exciting phenomena have been revealed [6], [12], [23], [89]–[97]. Examples of network synchronization feature wide variety of spatial and temporal behaviors such as perfect in-phase synchrony (all the elements in array behave in identical manner), intensity synchronization (all the have the same time-dependence of intensities but vary in phases), time-delayed synchronization[93], cluster synchronization (some clusters of the array are synchronized by other elements in the array are not)[91], [94], and other types of synchronized behavior. Time series of synchronized array may show periodic or fixed-point behaviors, chaotic behavior (chaotic synchronization[95]), and chimera states where some clusters are periodically synchronized and others are chaotically synchronized[92], [96].

While there exist a wide variety of experimental systems where phase synchrony is important, it is not always straightforward to relate the theoretical/numerical

descriptions of phase synchrony with experimental findings. Experimentally controlling oscillator network's coupling structure, coupling strength, or even parameter values of network elements is not always possible. Moreover, experimentally accurate theoretical description of the dynamics of some dynamical networks is very challenging due to an inherent trade-off between the experimental reality and theoretical/computational complexity of the problem. Consequently, achieving a satisfactory level of resemblance between the experimental and theoretical/computational outcomes is a challenging task.

Single mode semiconductor diode lasers are one of few examples of nonlinear systems that have been extensively studied both experimentally and theoretically. The equations of motion describing a single semiconductor diode and arrays of coupled diodes have been experimentally verified and extensively tested[12], [58], [59], [98]–[102]. A semiconductor laser diode array can be described as a network of coupled nonlinear oscillators[6], [12], [103]. It is known that weakly nearest-neighbor coupled semiconductor lasers can be phase synchronized[59], [98], [99]. Chaotic synchronization has been demonstrated for systems of two and three lasers[6, and references therein]. For large arrays however, the in-phase solution destabilizes in favor of anti-phase, traveling-wave solutions and, if coupling strength is moderately large, in favor of spatiotemporal chaos. The coupling strength at which this destabilization occurs seems to decrease with array size[59]. This destabilization occurs because as coupling strength increases, the number of fixed-frequency solutions (external cavity modes) increases and the coupled lasers begin to chaotically hop between these fixed-frequency solutions[12], [100], [101], [104], [105]. Also in other coupled oscillator systems with nearest-neighbor configuration, in-phase solutions destabilize with large array size[23], [89].

In the case of perfect global coupling (also referred to as all-to-all or mean-field coupling) it is understood that most large systems including semiconductor lasers will synchronize with appropriate parameters and sufficiently low disorder[6], [36], [89], [106], [107]. However, perfect global coupling can be hard (or impossible) to achieve in experiments because it requires that the coupling between any two elements have no dependence on distance between them. Master-slave centralized type coupling schemes have also been shown to allow for phase-synchronization in semiconductor laser arrays and other systems[13], [108].

A large body of experimental work has been reported for semiconductor laser arrays subject to external cavity feedback[52], [55], [102], [109]–[112]. The motivation of those experiments was to achieve phase locking (phase synchrony) of the array and subsequently achieve as close as possible to diffraction-limited emission from the array. A variety of cavity designs have been studied including V-shape cavity[55], [109], self-Fourier cavity[52], and external Talbot cavity[111]. Some of the experiments were performed using high power, broad-area

semiconductor diodes however a single transverse mode was achieved due to a volume or surface grating inserted in the cavity[55]. In some experiments, commercial quality diodes were employed; consequently, heterogeneity range of the laser diodes was large. Still, an almost perfect diffraction limited beam has been reported from diode laser arrays[55], [109] indicating that largely heterogeneous and noisy diode arrays can robustly and spontaneously phase synchronize, provided the coupling network geometry is appropriately chosen. One could wonder (a) what causes such almost perfect synchrony of the highly heterogeneous array (it is clear that in-phase solution for such array is not possible), and (b) how such almost perfect phase synchrony depends on the size of the array.

While it is customary to assume mathematically simple coupling matrix forms (such as nearest neighbor, nearest two neighbors, rings of nearest neighbors, and perfect global coupling) in studying phase synchronization of large nonlinear arrays, such coupling terms do not always represent real experimental conditions. Here, we adopt a form of coupling that is representative experimental configurations that allow for an excellent degree of phase synchrony. Namely, we use a decayed nonlocal coupling scheme, where the strength of feedback between two lasers decreases as the distance between the lasers increases. This coupling scheme is representative of many experimental schemes[1], [86], [111], [113]–[115]. Based on such typical configurations, we would like to identify and explain the phase synchronization mechanism.

Regarding coupled nonlinear oscillators, mode selection is most closely alluded to in the Master Stability Function (MSF) theory [90]. The MSF has become a reliable way to determine stability of perfectly synchronous (both chaotic and non-chaotic) states of these systems[90] and has also been modified to determine the stability of clustered states[91], [93], [94], synchronization on hyper-networks[116], [117], and synchronization of non-identical systems[118] or nearly-identical systems[108]. However, the MSF is specifically applied to only the first transverse mode of systems where the first mode of the coupling network is perfectly synchronous[90]. It should also be noted that the concept of mode selection is very fundamental to laser physics and our use of this term is not new[1], [45]. However, we believe that this result serves to connection between mode selection in electromagnetic resonators and other continuous systems and the MSF in coupled nonlinear oscillator systems. Here, we use an extension of MSF theory to show how the dynamics of non-synchronous transverse modes can scale with array size. In one of the cases we consider, the first transverse mode is approximately synchronous, as it is a curved Gaussian-type mode. This may also be the most relevant case for experimental laser synchronization. However, we also show that it is possible to predict chaotic anti-phase synchrony.

Employing an extended version of the MSF formalism, we show that an almost perfect (but not in-phase) phase synchronous state (fixed point, periodic limit cycle, and chaotic dynamics) described by non-constant eigenvectors can be realized. We also show how it is possible to generate non-synchronous transverse modes that lead to chaotic anti-phase synchronization. To the best of our knowledge, chaotic anti-phase synchronization has not yet been demonstrated in large arrays of coupled lasers and/or nonlinear oscillators. This result is an example of linear mode selection in a highly nonlinear system.

Analysis and results

An array of M semiconductor lasers can be modeled using an equation of the general form

$$\dot{\mathbf{X}}_i(t) = \mathbf{F}(\mathbf{X}_i(t)) + \frac{\kappa^f}{M}\sum_{j=1}^{M} K_{ij}\mathbf{C}(\mathbf{X}_j(t-\tau),\mathbf{X}_i(t)) . \tag{2.16}$$

where κ^f is the feedback strength. This represents a general system of oscillators coupled through a network with delayed feedback. Much of the work we describe in this paper could be applied to any system of this form. In the case of semiconductor laser arrays, $\mathbf{X}_i$ is the state of the ith laser:

$$\mathbf{X}_i = \begin{bmatrix} r_i(t) \\ \phi_i(t) \\ N_i(t) \end{bmatrix} \tag{2.17}$$

where r_i is the field magnitude, ϕ_i is the phase, and N_i is the number of carriers in the gain medium. The electric field in the ith laser is $E_i = r_i(t)e^{i\phi_i(t)}$. $\mathbf{F}(\mathbf{X})$ is the expression for the time-evolution of the uncoupled laser[58]:

$$\mathbf{F}(\mathbf{X}_i) = \begin{bmatrix} \frac{1}{2}\left(g\frac{N_i(t)-N_0}{1+sr_i^2(t)} - \gamma\right)r_i(t) \\ \frac{\alpha}{2}\left(g\frac{N_i(t)-N_0}{1+sr_i^2(t)} - \gamma\right) + \omega_i \\ J_0 - \gamma_n N_i(t) - g\frac{N_i(t)-N_0}{1+sr_i^2(t)}r_i^2(t) \end{bmatrix} \tag{2.18}$$

where $N_0 = 1.5*10^8$ is the number of carriers in the un-pumped gain medium, $g = 1.5*10^{-8}\,\mathrm{ps}^{-1}$ is the differential gain coefficient[119], [120], $s = 2*10^{-7}$ is the gain saturation coefficient, $\gamma = .05\mathrm{ps}^{-1}$ is the loss, $\alpha = 5$ is the linewidth enhancement factor (also known as the Henry constant)[84], [121], and

$\gamma_n = .5\text{ns}^{-1}$ is the loss term for the carriers. $J_0 = a\gamma_n(N_0 + \frac{\gamma}{g})$ is the pump current, where $a = 4$ is a scalar multiplier denoting the ratio between J_0 and the threshold current. Note that this pump current is far above the threshold current, therefore the nonlinear gain saturation term (proportional to g) plays a role in the dynamics of the system[120]. ω_i is the frequency detuning for the ith laser. The sum term represents feedback from the other lasers in the array to the ith laser:

$$\mathbf{C}(\mathbf{X}_j(t-\tau), \mathbf{X}_i(t)) = \begin{bmatrix} r_j \cos(\phi_j(t-\tau) - \phi_i(t)) \\ \frac{r_j(t-\tau)}{r_i(t)} \sin(\phi_j(t-\tau) - \phi_i(t)) \\ 0 \end{bmatrix}. \quad (2.19)$$

We can also add spontaneous emission noise and carrier inversion noise as in [122], [123]. Λ_i is the noise in the ith laser:

$$\Lambda_i = \begin{bmatrix} \sqrt{R_{sp}}[\Re(\eta_E(t))\cos(\phi_i(t)) + \Im(\eta_E(t))\sin(\phi_i(t))] \\ -\frac{\sqrt{R_{sp}}}{r_i}[\Re(\eta_E(t))\sin(\phi_i(t)) - \Im(\eta_E(t))\sin(\phi_i(t))] \\ \sqrt{N_i(t)}\eta_N(t) \end{bmatrix}$$

where $R_{sp} = 5\text{ns}^{-1}$ is the spontaneous emission rate, η_E is complex uncorrelated Gaussian white noise and η_N is real uncorrelated Gaussian white noise. The resultant equation will then be written as:

$$\dot{\mathbf{X}}_i(t) = \mathbf{F}(\mathbf{X}_i(t)) + \frac{\kappa^f}{M}\sum_{j=1}^{M} K_{ij}\mathbf{C}(\mathbf{X}_j(t-\tau), \mathbf{X}_i(t)) + \Lambda_i(t).$$

The decayed coupling scheme can be described using a matrix of the form

$$K_{ij} = d_x^{|i-j|}. \quad (2.20)$$

where $d_x < 1$. We use the scaling of $\frac{1}{M}$ in Eq. (2.16) to ensure that $\kappa^f \sum_j K_{ij} < \gamma$ for the laser cavities. If this relationship does not hold, then the weak coupling approximation (for which the Lang-Kobayshi equations were derived) is no longer valid. This is because the fields in the gain-free system $\dot{E}_i = -\gamma E_i + \kappa^f \sum_{j=1}^{M} K_{ij} E_i$

should decay to $E_i = 0$ for all i to guarantee that energy conservation is not violated.

We also consider a modified coupling matrix from the one we have presented. The coupling matrix $\mathbf{K}$ described by Eq. (2.20) can be decomposed as $\mathbf{K} = \sum_{i=1}^{M} \lambda_i \vec{V}_i \vec{V}_i^T$ where $\lambda_1 > \lambda_2 > ... > \lambda_M$ are eigenvalues of $\mathbf{K}$, and where $\vec{V}_i$ are the correspondingly ordered eigenvectors. We define the modified coupling matrices $\mathbf{K}_i$:

$$\mathbf{K}_i = \lambda_1 \vec{V}_i \vec{V}_i^T + \lambda_i \vec{V}_1 \vec{V}_1^T + \sum_{j \neq 1,i}^{M} \lambda_j \vec{V}_j \vec{V}_j^T \quad (2.21)$$

These matrices have the same eigenvalue spectrum as the original $\mathbf{K}$ matrix, however the leading eigenvector is different. For example $\mathbf{K}_2$ has the leading eigenvector $\vec{V}_2$. Using $\mathbf{K}_i$, we observe spatial phase organization that corresponds to the ith eigenvector. We show spatial phase organization and corresponding eigenvectors in Figure 2.7. In the figure, it is clear that the relative phase of each laser in the array corresponds to the sign of the corresponding eigenvector element. This result should not be surprising when the lasers are on the continuous-wave solution, which is stable when the nonlinear terms in Eq. (2.18) are small. In this case, the coupling terms proportional to κ^f dominate the equation. Physically, this means that the lasers are simply following the leading mode -- that which decays the slowest in the cold-cavity case. It should be noted that all coupling topology with a power-law type decayed nonlocal coupling (where the laser has maximal feedback to itself and exponentially decaying feedback to adjacent lasers) and constant phase should produce similar spatial modes to those presented in the Figure 2.7. In realistic systems, the property of decaying feedback is common, with phase-shifts being controllable to an extent[1], [86], [113]. Recently it has been demonstrated that using diffractive coupling [124] or optical fibers [102] one can design reconfigurable semiconductor laser networks where the network topology can be more precisely defined and controlled. So it might be possible to generate systems with phase-organized leading modes (i.e. external cavities with coupling matrices similar to $\mathbf{K}_{2,3,4}$), such as in Figure 2.7(b-d).

Master stability functions

To understand why such phase organization occurs in the laser system and whether this behavior can occur in the presence of more nonlinearities, we can derive an extension to the MSF. To find the MSF for a system, it is required that the row-sum of the coupling matrix be constant. Our system does not satisfy this requirement. In cases like this, it can be useful to look for ways to achieve

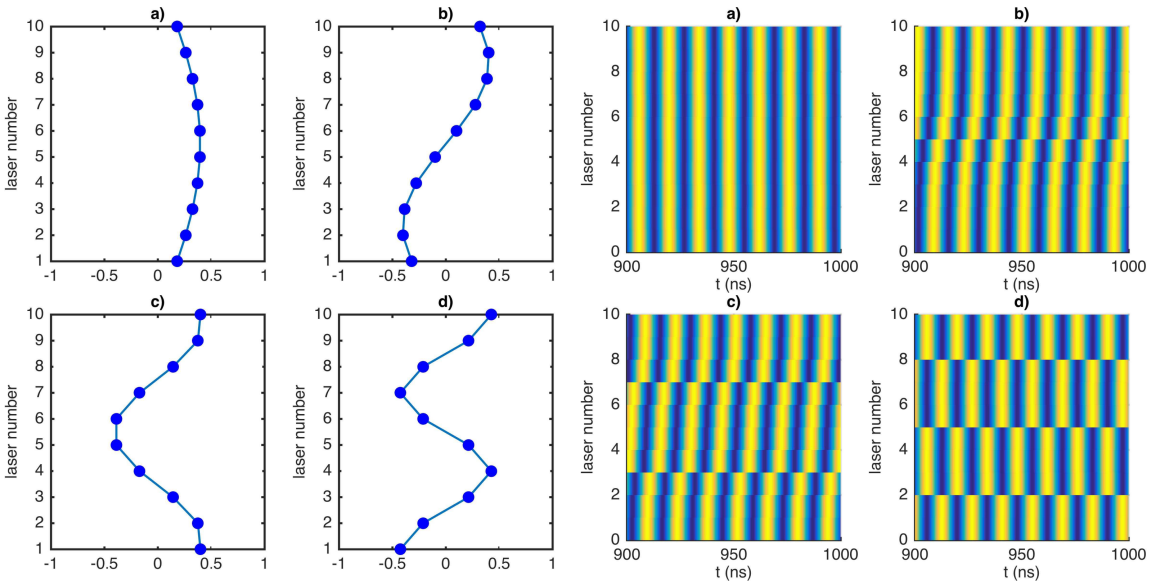


Figure 2.7. Leading mode eigenvectors (left) and array phases (right) of arrays with coupling matrices (a) $\mathbf{K}_1$, (b) $\mathbf{K}_2$, (c) $\mathbf{K}_3$, and (d) $\mathbf{K}_4$. We use here $\kappa^f = 5\text{ns}^{-1}$ and $d_x = .5$ and simulate the dynamics in the presence of noise. In the phase dynamics plot, the color represents the cosine of the phase of each laser. We observe that the synchronized clusters of the array dynamics correspond to the maxima and minima of the eigenvectors.

imperfect forms of synchronization such as cluster synchronization or chimera states [91]–[93], [97]. However, this type of non-synchronous phase organization is not cluster synchronization (or a chimera state), but rather mode selection. We derive a modified MSF that describes states that are parallel to each eigenvector of the coupling matrix; these are the standing modes of the system. In this way we search for a non-synchronous, but *almost perfectly* synchronous state that is described by the leading eigenvector. For the derivation and analysis, we consider arrays of identical lasers ($\omega_i = 0$ for all i) without the presence of thermal or current noise. However, all of the analysis is verified using simulations with non-identical lasers in the presence of noise, and the effects of disorder and noise are studied.

We begin by Taylor expanding to first order Eq. (2.16) about the desired (synchronous) solution $\mathbf{X}^*$, leading to the variational equation

$$\dot{\xi}_i(t) = D_1\mathbf{F}\xi_i(t) + \frac{\kappa^f}{M}\sum_{j=1}^{M} K_{ij} D_1\mathbf{C}\xi_i(t) + \frac{\kappa^f}{M} K_{ij} D_2\mathbf{C}\xi_j(t-\tau) \tag{2.22}$$

where D_1 is the gradient operator with respect to the variables $\mathbf{X}_i$ in Eq. (2.16) and D_2 is the gradient operator with respect to the variables $\mathbf{X}_j(t-\tau)$. This means $D_j\mathbf{F}$ and $D_j\mathbf{C}$ are matrices of derivatives of $\mathbf{F}$ and $\mathbf{C}$ with respect to the variables $\mathbf{X}$ evaluated at the solution $\mathbf{X}^*$. We can let Γ be a diagonal matrix whose ii th element is $\sum_{j=1}^{M} K_{ij}$. The variational equation for the whole array can be written as

$$\dot{\vec{\xi}}(t) = [\mathbf{I}_M \otimes D_1\mathbf{F} + \frac{\kappa^f}{M}\Gamma \otimes D_1\mathbf{C}]\vec{\xi}(t) + \frac{\kappa^f}{M}[\mathbf{K} \otimes D_2\mathbf{C}]\xi(t-\tau) \tag{2.23}$$

where $\mathbf{I}_M$ is the M-dimensional identity matrix. We can let $\mathbf{V}_i^n = \vec{V}_i \otimes e_n$ where $\vec{V}_i$ is the i th eigenvector of $\mathbf{K}$ and e_n is the n th unit vector in a 3-dimensional space (one direction for each dimension of the laser (r, ϕ, N)). For example, the vector $\mathbf{V}_2^1$ would point in the direction of the intensity r of the second modal (eigenvector) direction of the system. We now observe that the set $\{\mathbf{V}_i^n : i \in \{1,..., M\}, n \in \{1,2,3\}\}$ forms a basis for the space of array dynamics. We accordingly define δ_i^n to be the i th mode's n th component:

$$\vec{\xi} = \sum_{i=1}^{M}\sum_{n=1}^{3} \delta_i^n \mathbf{V}_\mathbf{i}^\mathbf{n}$$

so $\delta_i = (\delta_i^1, \delta_i^2, \delta_i^3)^T$ represents the i th mode in the linearized system and $\vec{\delta} = (\delta_1,..., \delta_M)^T$ is the vector of modal variations.

We define a matrix $\mathbf{U}$ whose columns are the vectors $\vec{V}_1,...,\vec{V}_M$. Then we observe that $\mathbf{U}^\dagger\mathbf{K} = \mathbf{D}\mathbf{U}$ where $\mathbf{D}$ is a diagonal matrix whose iith entry is the ith eigenvalue λ_i of $\mathbf{K}$. We then let $\mathbf{U}' = \mathbf{U} \otimes \mathbf{I}_3$. This means that the vector describing variations from synchronization in the directions of the modal basis is: $\mathbf{U}'^\dagger\vec{\xi} = \vec{\delta}$.

It follows that

$\mathbf{U}'^\dagger[\mathbf{K} \otimes D_2\mathbf{C}] = \mathbf{D}\mathbf{U}^\dagger \otimes D_2\mathbf{C}$

$\mathbf{U}'^\dagger[\mathbf{I}_M \otimes D_1\mathbf{F}] = \mathbf{U}^\dagger \otimes D_1\mathbf{F}$

$\mathbf{U}'^\dagger[\Gamma \otimes D_1\mathbf{C}] = \mathbf{G} \otimes D_1\mathbf{C}$.

Here we make the following approximation. If we assume that row-sums of $\mathbf{K}$ are approximately identical (which is not necessarily true), then $\mathbf{G} \approx k_{sum}\mathbf{U}^\dagger$ where k_{sum} is an approximation for the row-sum of the coupling matrix. Since the matrix we use is real and symmetric positive definite, we will use the largest eigenvalue of $\mathbf{K}$, λ_1.

To show that the constant row-sum approximation is reasonable, we consider the operator $\mathbf{G} \otimes D_1\mathbf{C}$:

$$[\mathbf{G} \otimes D_1\mathbf{C}]\vec{\xi} = \mathbf{U}'^\dagger[\Gamma \otimes D_1\mathbf{C}]\sum_j \vec{V}_j \otimes \delta_j = \sum_j [\mathbf{U}^\dagger\Gamma\vec{V}_j] \otimes [\mathbf{I}_3^\dagger D_1\mathbf{C}\delta_j].$$

The ith row of blocks of the above expression is:

$$\sum_j [\vec{V}_i^\dagger\Gamma\vec{V}_j]D_1\mathbf{C}\delta_j. \tag{2.24}$$

We observe that if the row-sums are not constant, there is a coupling between the ith and jth modes that is proportional to $\vec{V}_i^\dagger\Gamma\vec{V}_j$. For the coupling matrix that we use, we find that for all values of d_x, $\vec{V}_i^\dagger\Gamma\vec{V}_i >> \vec{V}_i^\dagger\Gamma\vec{V}_j$ if $i \neq j$. This means that off-diagonal terms are small and the modes are approximately decoupled. It is not the case that $\vec{V}_i^\dagger\Gamma\vec{V}_i = \lambda_i$. However, it is the case that $|\vec{V}_i^\dagger\Gamma\vec{V}_i - \lambda_i| << \lambda_i$ for all i and for all values of d_x that we consider. This is why we let $k_{sum} \approx \lambda_1$.

So the ith block of the transformed Eq. (2.23) is

$$\dot{\delta}_i(t) = [D_1\mathbf{F} + \frac{\kappa^f}{M}\lambda_1 D_1\mathbf{C}]\delta_i(t) + [\frac{\kappa^f}{M}\lambda_i D_2\mathbf{C}]\delta_i(t-\tau) \tag{2.25}$$

The above equation is the equation we use for the modal stability function. The modal stability function is defined as the maximal and submaximal (since this is a delay system) Lyapunov exponents of the equation[90]. This tells us whether the

ith mode will decay. If all of these modes decay ($\delta_i \to 0$ as $t \to \infty$) then perfect synchronization will be be stable.

The linearized equation for a single laser with feedback strength κ^f is

$$\dot{x}(t) = [D_1\mathbf{F} + \kappa^f D_1\mathbf{C}]x(t) + [\kappa^f D_2\mathbf{C}]x(t-\tau) \quad (2.26)$$

The effective coupling for our MSF equation is $\kappa' = \frac{\kappa^f}{M}\lambda_1$ [90]. With the effective coupling, Eq. (2.25) becomes

$$\dot{\delta}_i(t) = [D_1\mathbf{F} + \kappa' D_1\mathbf{C}]\delta_i(t) + [\kappa'\frac{\lambda_i}{\lambda_1} D_2\mathbf{C}]\delta_i(t-\tau). \quad (2.27)$$

We can see that when we consider the first mode of the system (with the eigenvalue λ_1), the Eq. (2.27) is the same as the equation Eq. (2.26). This means that the behavior of the first mode of an array of lasers should mirror the behavior of the single laser. For example, the behavior of lasers in an array with effective coupling $\kappa' = \frac{\kappa^f}{M}\lambda_1 = 5\text{ns}^{-1}$ should be similar to the behavior of a single laser with coupling $\kappa^f = 5\text{ns}^{-1}$.

When we use the $n = 1$ coupling matrix, $\mathbf{K}_1$, the mode associated with λ_1 is a curved almost-synchronous mode as in Figure 2.7. To show that the behavior of the whole array can be mapped onto the single laser behavior, we show in Figure 2.8 max/min diagram for a single laser and an array of 10 lasers. The value of κ^f at the bifurcation transition point from the fixed point solution to oscillating solutions for a single laser is equal to the value of κ' for the array at the corresponding transition point. Also note the similarities between both bifurcation curves. Even though the synchrony may not be perfect (though it is indeed extremely close to phase-locked for $\kappa^f < 12\text{ns}^{-1}$), the bifurcation curve scales according to the effective coupling, as predicted by the similarity between Eqs. (2.26) and (2.27).

In Figure 2.9 we show more definitively that the average phase synchrony of an array with the original coupling matrix $\mathbf{K}_1$ can be predicted by the effective coupling of the array. As the array size grows, the range of coupling strength for which synchronous behavior occurs can be determined by the values of the array effective coupling. Each labeled section of the figure corresponds to a region of dynamics. When $\kappa' < 4.3\text{ns}^{-1}$ the fixed-frequency, fixed-intensity limit cycle is stable. As κ' grows the behavior becomes quasiperiodic and then then chaotic until it desynchronizes once κ' exceeds 16ns^{-1}. The red line in Figure 2.9 is when synchrony through strong coupling occurs. This type of synchronization is

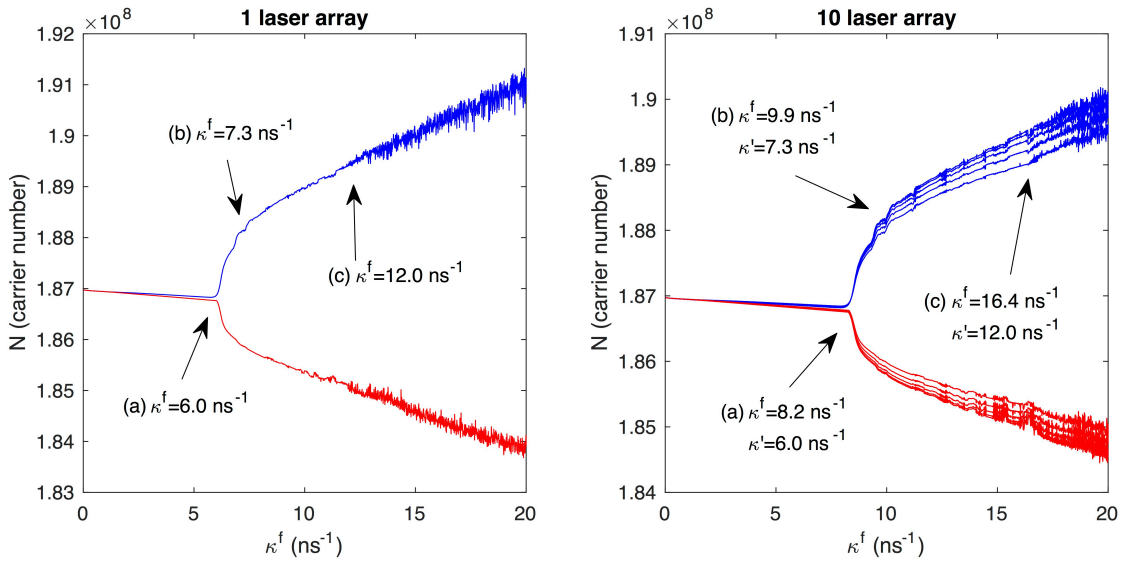


Figure 2.8. Max/min diagram for a single laser and an array of 10 lasers. The blue lines denote maximal values of the carrier number N and the red lines denote minimal values of the carrier number. The value of d_x for 10 laser array is .9. The largest eigenvalue for the 10 laser coupling matrix in this case is $\lambda_1 \approx 7.3$. So $\kappa'(\kappa^f) \approx \kappa^f * (7.3)/10$. The labeled events scale consistently in the two bifurcation plots. These plots were generated using a continuation method with steps in κ^f of $.01\text{ns}^{-1}$ with simulation time of 200ns at each step.

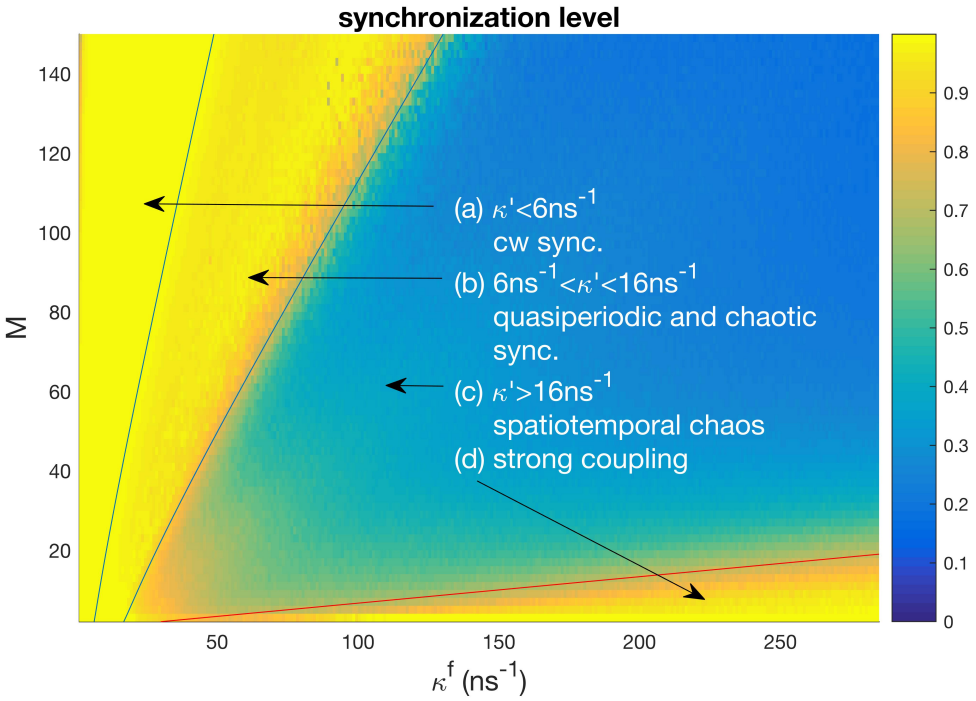


Figure 2.9. Average phase synchrony of large arrays of lasers. Each point corresponds to a simulation of delayed Lang-Kobayashi equations for diode laser array with randomized initial conditions (we started averaging process after 800ns simulation for convergence to occur). We observe both stable CW and unstable chaotic phase synchronization of diode laser array. Lines denoting regions of effective coupling are related to the degree of synchronization in the system. For very large arrays achieving phase synchronization requires either very weak or very strong (and possibly unrealistic) coupling κ^f between the diodes in the array.

similar to the type described in [36] and occurs when the coupling strength exceeds a critical value likely requires an unrealistically large coupling strength value for a set of diode lasers.

It is well-known that in semiconductor lasers, increasing feedback increases the number of the so-called External Cavity Modes (ECMs) [21], [105], [125], [126]. These can be found analytically as the fixed-frequency, fixed-intensity solutions of Eq. (2.16) for a single laser. These modes are created in pairs (one unstable, and one stable `anti-mode'). In fact, as κ^f increases, the number of stable ECMs increases at an approximately linear rate (with one unstable ECM appearing for each stable ECM). Each ECM (stable and unstable) is defined by a unique frequency, which is defined with respect to a central frequency (which is the zero frequency in the local frame of reference). If a laser is on a single stable ECM then it has a fixed intensity and carrier number and its phase rotates at the ECM frequency (i.e. the frequency difference Δ associated with the ECM and the central frequency of the laser). When the coupling strength, κ^f is increased, the number of these ECMs increases. As κ^f is increased, quasiperiodic attractors appear around the unstable ECM solutions. When the number of ECMs becomes large, the trajectories of the ECM solutions get very close together. When this happens, even small perturbations will cause the laser to switch attractors, so that the laser begins to hop between the attractors near the ECMs resulting in chaos [125]. This attractor hopping is illustrated in Figure 2.10(d). The single laser trajectory jumps between many values in the delay-coordinate axis, which is consistent with [21], [105], [125], [126]. However, the 10 laser trajectory does not seem to hop between attractors. It should be noted that the equations (2.16) are multi-stable; it is possible for the system to converge to a different set of attractors than those shown in Figure 2.10 by starting from random initial conditions (instead of the continuation, which is what is shown in the figures).

In-phase and anti-phase synchrony

The expression for the array mode dynamics (Eq. (2.27)) implies that the stability properties of the ECMs for the leading array mode should be identical to those of the single laser. That is, the time-evolution of the lasers should be the same as the single laser with $\kappa^f = \kappa'$ whereas the relative phases of the lasers in the array (i.e. the transverse profile) should follow the mode eigenvector. This is supported by the diagram in Figure 2.8. In Figure 2.11 we show the behavior of the phases of the array with the bifurcations and can observe that the phases of the array appear synchronized (following the $n = 1$ eigenvector for the matrix $\mathbf{K}_1$). When $\kappa' = 3\text{ns}^{-1}$ we observe the continuous-wave solution. Quasiperiodic synchrony can be observed when $\kappa' = 6.0\text{ns}^{-1}$. Chaotic synchrony can be observed when $\kappa' = 9\text{ns}^{-1}$. Once the behavior becomes too chaotic, synchrony

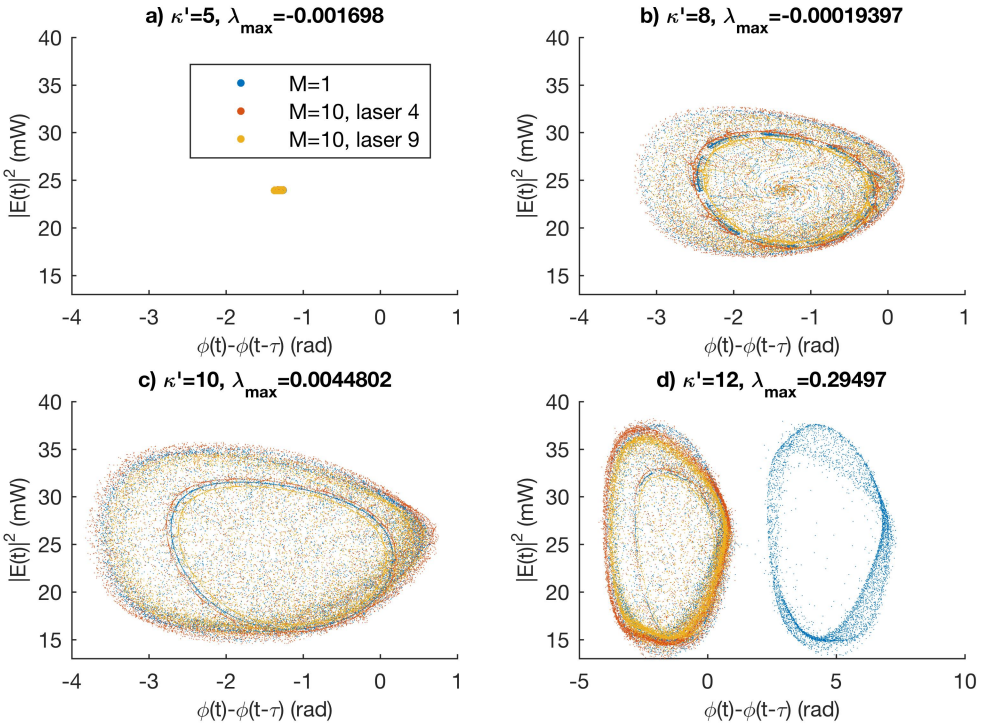


Figure 2.10. Projections of the attractors on the $|E|,\Delta$ plane at various points in the continuation shown in Figure 2.8 are plotted for single lasers and selected lasers within the synchronized array of lasers. For the single laser, note that $\kappa' = \kappa^f$. We also include numerical estimates for the maximal Lyapunov exponent for each attractor (calculated from the single laser dynamics during the continuation). For parts (a-c), the behavior of the single laser and the 10-laser array are almost identical. However for part (d) when the single laser is hopping between the ECM solutions, the array of lasers remains near only one of the ECM solutions. Note that these plots are taken from the continuation simulations.

begins to break down (but is still relatively high when $\kappa' = 12\text{ns}^{-1}$). The behaviors observed here do correspond to those in the bifurcation plot in Figure 2.8. As the number of lasers M increases, the only change in the stability equation (Eq. (2.25)) is the value of κ'. Simulations indicate that the dynamics of synchrony should correspond to this value of κ' independently of M. So for very large M, the κ'^{crit} for which synchrony de-stablilizes is the same as for small M. So as M increases, $\kappa^{f,crit} = M\kappa' / \lambda_1$ should increase (note that for the matrix form we consider, λ_1 is in fact bounded).

We believe that the chaotic synchrony in Figure 2.11 can be thought of as the entire array of lasers behaving as a single unit and we have verified that dynamics of the individual lasers in the array in this regime are similar to those of a single laser. As we showed in Figure 2.10(d), even when the number of ECM solutions for the single laser is large, the lasers are restricted to a small subset of the ECMs. We believe that this restriction is because many of the ECM solutions for the array could be destabilized because of the off-diagonal mode-coupling terms that we neglected in the approximation (Eq. (2.24)).

For the $n > 1$ coupling matrices $\mathbf{K}_n$, the first mode, as shown in Figure 2.7 is not synchronous and should be anti-phase. If indeed the reason for chaotic synchronization is dimensionality reduction through mode selection, then we should be able to observe chaotic dynamics regardless of the leading mode eigenvector shape. Therefore, we use the matrix $\mathbf{K}_2$ in simulations with increased coupling strength. This is shown in Figure 2.12. Since the matrices $\mathbf{K}_1$ and $\mathbf{K}_2$ have identical eigenvalue spectrum, the stability function for this mode should be the same, as in Eq. (2.27) so the temporal dynamics of the mode should be similar. We find that the anti-phase synchronization seems to persist for a larger value of κ' then it would in the $n = 1$ case. We can see that in this case, when $\kappa' = 6\text{ns}^{-1}$ the lasers are still on the CW solution. We believe that this scaling is due to the geometry of the $n = 2$ anti-phase transverse mode (as shown in Figure 2.7 somehow making a subset of the ECM solutions for the system inaccessible. Since the chaos in this system is due to hopping between ECM solutions, when we decrease the number of accessible ECM solutions, the complexity of the dynamics should be reduced as well; i.e. a larger number of ECM solutions (higher κ') should be created in order for the full chaotic trajectory to begin.

To understand whether these in-phase solutions are realistic, we need to understand the effects of disorder in the system. When a frequency shift is added in a single laser (in the form of ω_i in Eq. (2.18), it can be easily shown

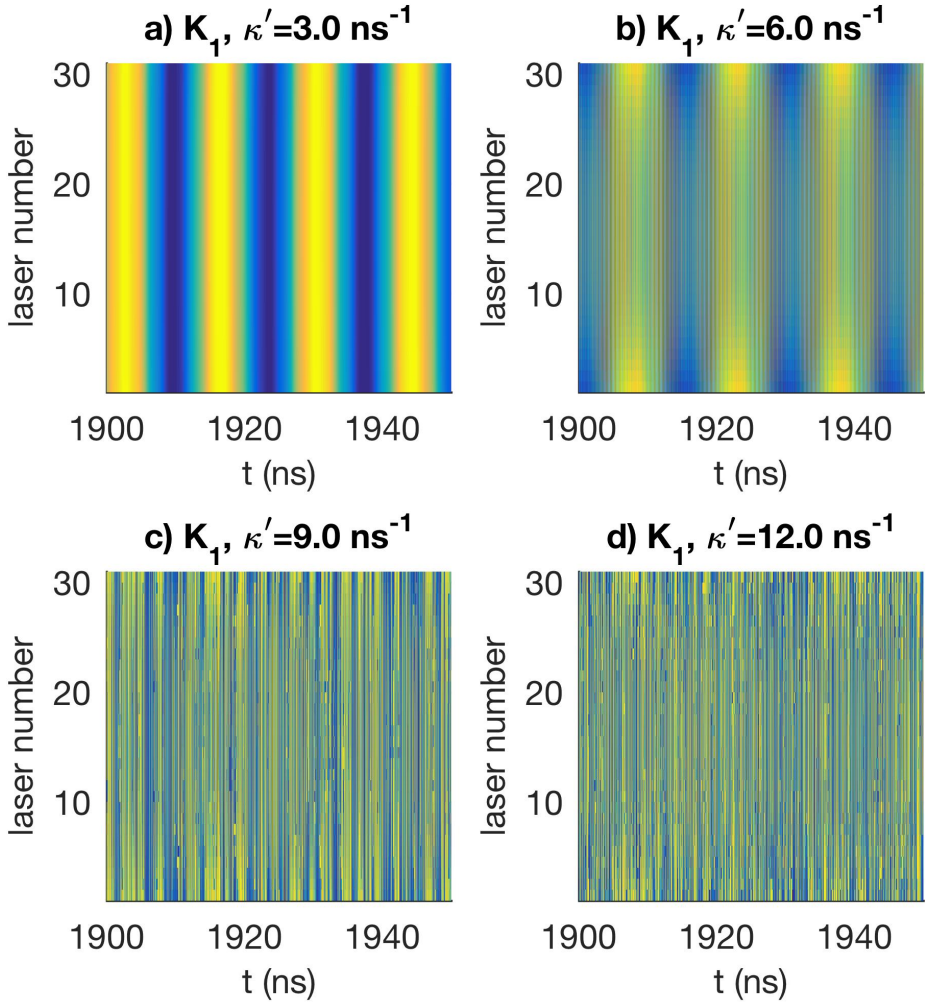


Figure 2.11. Trajectories of $\cos\phi_j$ of an array of $M = 30$ lasers in the presence of noise coupled through the matrix $\mathbf{K}_1$ with $d_x = .8$. As $\kappa' = \kappa^f \frac{\lambda_1}{M}$ is increased, the behavior becomes more complex. In (a) we observe synchrony on the cw solution. In (b) there is quasiperiodic synchronization with a very high degree of synchrony. In (c) there is chaotic synchronization with a slightly lower but still high (above 95%) synchronization. In (d) the chaotic synchrony is still high, but is starting to become less perfect.

analytically that the solutions of Eq. (2.16) shift in frequency by an interval of ω_i. However, when each laser has a unique frequency shift ω_i, the result is less trivial, since the synchronous solution $\mathbf{X}^*$ (that we use to get Eq. (2.22)) is no longer valid (because each uncoupled laser has its own equation). To analytically understand this effect, it might be useful to consider the approach of [108]. This is analysis is not done in this paper.

To show that the in-phase synchrony (when we use $\mathbf{K}_1$ for coupling) is robust to moderate amounts of disorder, in Figure 2.13 we plot phase synchrony as a function of disorder and coupling strength for a 10 laser array with $d_x = .9$. We observe that synchrony is more robust to disorder at larger coupling strengths. This is likely due to an increase in the number of ECM solutions that are compatible solutions for all of the lasers that happens when κ^f is increased. For small κ^f, there is a very small number of stable ECMs. As κ^f is increased, the number of ECMs. Each ECM is defined by a frequency, and when κ^f is large, the number of possible frequencies is also large. Therefore, there could be a greater probability of finding an ECM that is compatible with all of the disordered laser frequencies.

We show in Figure 2.14 that it takes a much larger value of κ' for a disordered array of lasers to reach a chaotic state than for an array of identical lasers (as in Figure 2.11). This seems to support the idea that disorder reduces the number of accessible ECMs in the system (since the cause of chaos in this system is known to be the large number of stable and unstable ECMs).
There is also evidence that the solutions to which the systems converge are slightly different with different instances of disorder (this is not shown, but was observed when multiple simulations were conducted). This is not multi-stability; we believe that this is largely due to different instances of disorder making different ECM solutions inaccessible, thereby leading to a different set of ECMs between which the system travels.

Conclusions

We have shown that a weak nonlocal decayed coupling scheme induces a dominant transverse mode in semiconductor laser arrays that is almost perfectly phase synchronized. This mode is stable and independent on the number of lasers in array consequently very large arrays can be almost perfectly phase synchronized. We have also shown that by changing the coupling matrix, it is possible to induce non-synchronous dominant modes that persist even in the presence of chaotic dynamics. This is an example of the linear phenomenon of mode selection occurring in the presence of chaotic behavior. For both synchronous and non-synchronous states, the dynamics of the single oscillator

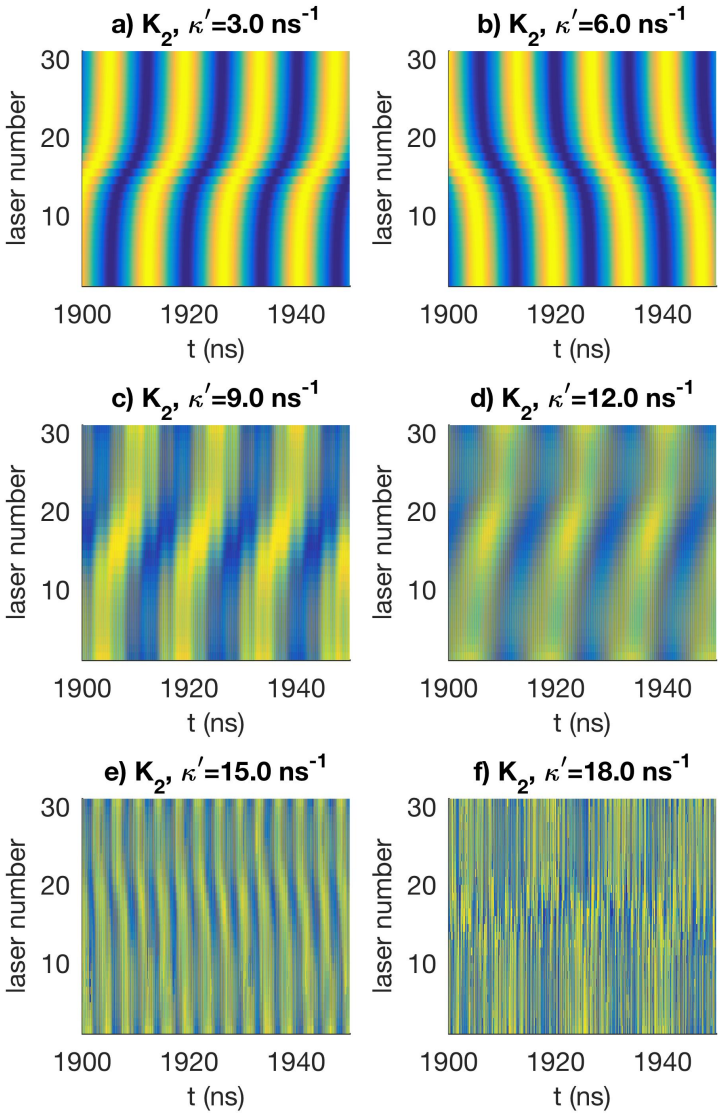


Figure 2.12. Trajectories of $\cos\phi_j$ of an array of $M = 30$ lasers in the presence of noise coupled through the matrix $\mathbf{K}_2$ with $d_x = .8$. As $\kappa' = \kappa^f \frac{\lambda_1}{M}$ is increased, the behavior becomes more complex, though with the bifurcation happening later than the same system with $\mathbf{K}_1$. In (a) and (b) we observe synchrony on the cw solution. In (c)-(f) the behavior becomes increasingly more chaotic, but maintains general antiphase behavior that corresponds to the leading $\mathbf{K}_2$ mode (i.e. the first 15 lasers are out of phase with the second 15 lasers).

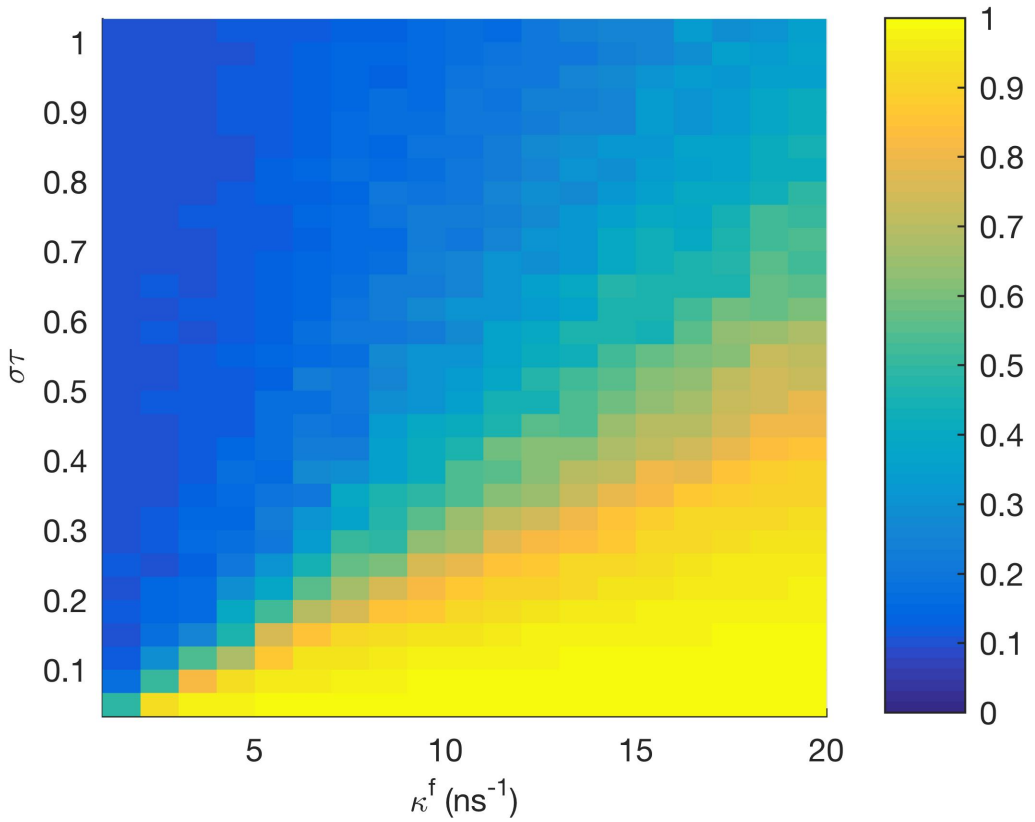


Figure 2.13. Average synchrony $S = < \frac{|\sum_{i=1}^{M} E_i|^2}{M\sum_{i=1}^{M}|E_i(t)|^2} >$ is plotted for arrays of 10 lasers without noise with varying levels of disorder and coupling strength and with coupling decay constant $d_x = .9$. ω_i is Gaussian-distributed about zero with standard deviation σ. The delay time is $\tau = 3\text{ns}$. Each point is averaged from 30 simulations with different randomized initial conditions and different random instances of disorder.

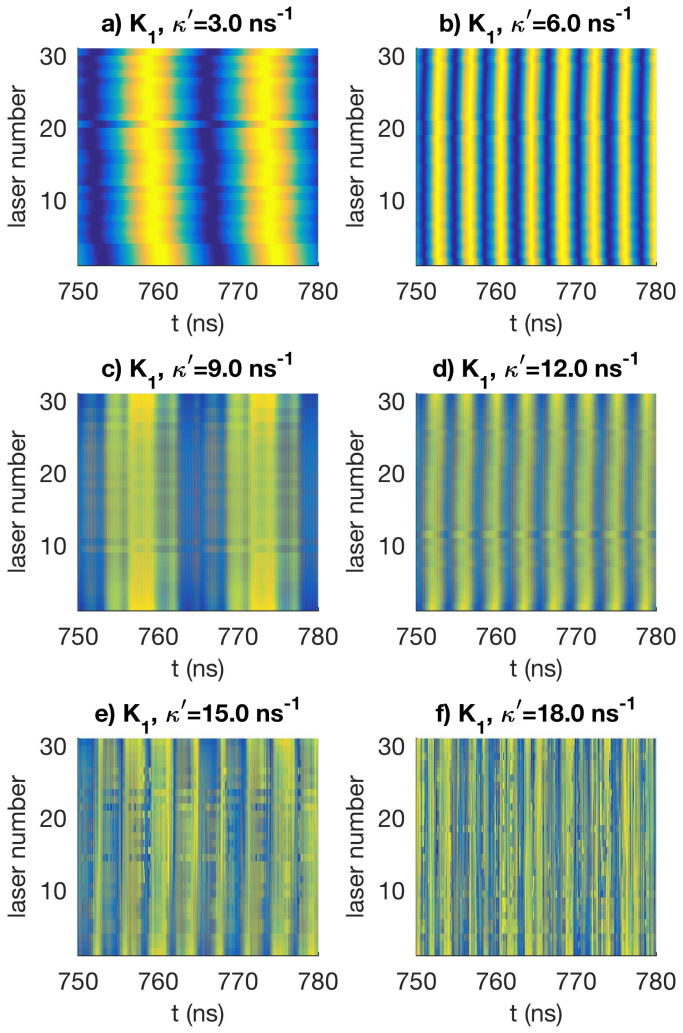


Figure 2.14. Trajectories of $\cos\phi_j$ of an array of $M = 30$ lasers in the presence of noise and disorder of $\sigma\tau = .3$ coupled through the matrix $\mathbf{K}_1$ with $d_x = .8$. In (a) we observe partial synchrony on the cw solution with non-negligible phase-mismatch. In (b) there is better synchrony on the cw solution, though the frequency to which the system has converged is much higher than in (a). In (c) there is quasiperiodic synchronization synchronization. In (d) there is higher frequency quasiperiodic synchrony. In (e), the synchrony begins to become chaotic. In (f) there is chaotic synchronization.

as shown in its bifurcation diagram can scale with array size. The approximately synchronous state that arises with the decayed coupling scheme resembles the leading normal mode of the gain-free laser system (which is linear) and ends up dominating the dynamics in the system with gain assuming that the nonlinearity does not become too strong (i.e. κ' becomes too large).

2.4 Derivation of the coupled Lang-Kobayashi equations from coupled mode theory

We have presented two theoretical results in Sections 2.2 and 2.3 that have not been experimentally validated. In section 2.2 we presented a derivation for a new model for laser dynamics as well as an example of the cold-cavity modes of an array of length-disordered waveguides coupled through a self-Fourier cavity. This analysis was done with minimal assumptions about the type of laser being modeled so that it is possible to use it for most types of external-cavity coupled laser systems. In section 2.3, we specifically considered weakly coupled semiconductor lasers and found that when the coupling matrix is chosen appropriately and coupling strength is sufficiently small, the array of lasers should behave as a single dynamical unit with spatial phase organization described by the leading eigenvector of the coupling matrix. Because each section uses a different modeling approach and neither is experimentally validated, it is important to at least show that the two approaches lead to consistent results. In this section we will show that it is possible to derive the Lang-Kobayashi equations (which are used in section 2.3) from the first-principles coupled-mode model derived in section 2.2.

The use of realistically derived cold-cavity modes for a coupled mode theory treatment of laser dynamics is typically only possible for a small number of lasers [57], [72], [127], in the limit of only a small amount of heterogeneity (or none at all) [65], [66], [71], [75], [85]. This is likely because of the computational and analytical complexity of, first, finding the cold cavity modes for a set of coupled heterogeneous resonators and, second, describing modal interactions for a set of M modes in N lasers. A full numerical treatment of our coupled mode model would require the use of $N+M$ coupled ordinary differential equations and further requires computation of an M-by-M matrix of N-dimensional inner products at each time-step. Note that this is still much less computationally intensive than implementing a direct numerical solution of Maxwell's equations spatially discretized in the coupled laser cavity geometry.

Therefore typically when arrays of more than 2 or 3 lasers are treated, a coupled nonlinear oscillator treatment is used, where rate equations (such as the Lang-Kobayashi equations in the case of semiconductor lasers) are used with phenomenologically defined coupling matrices [13], [39], [2], [62], [106], [128]–

[131]. The coupling networks have simple geometries such as nearest-neighbor coupling, global coupling, master-slave type coupling, or decayed non-local coupling. However, the has been no way of verifying the nature of these coupling terms. The derivation presented in this section show the relationship between the eigenvalue spectrum of the coupling matrix $\mathbf{K}$ of the coupled Lang-Kobayashi system and the complex frequency spectrum whole cavity propagator for the coupled resonator.

Deriving the Lang-Kobayashi equations using the coupled mode model

As in section 2.2, we will model the gain medium (the number of carriers in the gain medium and the gain coefficient) directly using the form from the Lang-Kobayashi equations with saturable gain [58], [119], [120]. It should be noted that in there are forms of the Lang-Kobayashi model that use different variations of these terms[21], [58], [121], [132]—it will be seen in this section that substituting other forms of these terms will lead easily to the other forms of the Lang-Kobayashi rate equations. The novelty of the derivation is the fact that we can reconstruct how the fields from the laser cavities are coupled using the modal derivation. This will provide the relationship between the eigen-spectra of the coupling matrix $\mathbf{K}=[K_{ij}]$ from Equation (2.16) and the whole-cavity round-trip operator from Equation (2.2).

We begin this derivation with the coupled mode model introduced in Equations (2.10)-(2.13). First, from (2.10) is the time-dependent part of the refractive index of the j th laser, Δn^j. This is modified from the version in (2.10) to include internal losses within the laser γ. In semiconductor lasers, this term is due to many factors including scattering and free-carrier absorption [133]. The parameter α_H is the Henry constant, c is the speed of light, g is the amplification rate, s is the gain saturation coefficient, and N_0 is the number of carriers in the gain medium at transparency. The terms included in the parameter G_j are specifically for semiconductor lasers and come from the Lang-Kobayashi equations[134].

$$\Delta n^j = -(i+\alpha_H)\frac{\pi c}{\omega}G_j = -(i+\alpha_H)\frac{\pi c}{\omega}\left(g\frac{N_j - N_0}{1+s\,|E_j|^2} - \gamma \right) \tag{2.28}$$

From (2.12) we use the rate equation for the number of carriers in the j th laser.

$$\frac{dN_j}{dt} = J_0 - \gamma_n N_j - g\frac{N_j - N_0}{1+s\,|E_j|^2}\,|E_j|^2$$

where N_j is the number of carriers in the j th laser's gain medium, γ_n is the carrier loss rate, and J_0 is the current into the laser.

From (2.13) we have the full modal equation for the field modes $a_m = \tilde{a}_m e^{-i\omega_m t}$ (where ω_m is the complex frequency of the mth whole cavity mode):

$$i\begin{bmatrix} \phi_1^\dagger n\psi_1 & \cdots & \phi_1^\dagger n\psi_M \\ \vdots & \ddots & \vdots \\ \phi_M^\dagger n\psi_1 & \cdots & \phi_M^\dagger n\psi_M \end{bmatrix}\begin{bmatrix} \omega_1 e^{-i\omega_1 t}\dot{\tilde{a}}_1(t) \\ \vdots \\ \omega_M e^{-i\omega_M t}\dot{\tilde{a}}_M(t) \end{bmatrix} = -\begin{bmatrix} \phi_1^\dagger \Delta n(t)\psi_1 & \cdots & \phi_1^\dagger \Delta n(t)\psi_M \\ \vdots & \ddots & \vdots \\ \phi_M^\dagger \Delta n(t)\psi_1 & \cdots & \phi_M^\dagger \Delta n(t)\psi_M \end{bmatrix}\begin{bmatrix} \omega_1^2 e^{-i\omega_1 t}\tilde{a}_1 \\ \vdots \\ \omega_M^2 e^{-i\omega_M t}\tilde{a}_M \end{bmatrix} \tag{2.29}$$

Note that the field in the j th laser can be expressed as:

$$E_j = \sum_{m=1}^{M} a_m \psi_m^{\ j} = \sum_{m=1}^{M} \tilde{a}_m e^{-i\omega_m t}\psi_m^{\ j} \tag{2.30}$$

Here, $\psi_m^{\ j}$ is the j th component (for the j th laser) of the mth whole-cavity mode eigenvector. Recall also the Δn is a diagonal matrix whose ith element is Δn^j.

We now assume that the modal eigenvectors $\{\psi_{m\in\{1,\ldots,M\}}\}$ (the right eigenvectors of the whole-cavity round-trip propagator) and $\{\phi_{m\in\{1,\ldots,M\}}\}$ (the left eigenvectors of the whole-cavity round-trip propagator, or the backwards modes) form a mutually orthonormal set for a set of M modes for a single longitudinal frequency (i.e. the *real* part of ω_m is the same for all $m \in \{1,\ldots,M\}$). Note that if M modes forms an orthonormal basis for (one-dimensional, as in Section 2.2) mode amplitudes a set of N lasers, then $M = N$. This single-frequency assumption is also used in most Lang-Kobayashi models. The other assumption is that the time-independent portion of the refractive index is the same for all lasers so that the N-by-N diagonal matrix n can be treated as a scalar value. With these assumptions, (2.29) becomes (after some algebra):

$$\begin{bmatrix} in\omega_1 e^{-i\omega_1 t}\dot{\tilde{a}}_1 \\ \vdots \\ in\omega_M e^{-i\omega_M t}\dot{\tilde{a}}_M \end{bmatrix} = -\begin{bmatrix} \phi_1^\dagger \sum_{m=1}^{M} \Delta n\psi_m \omega_m^2 e^{-i\omega_m t}\tilde{a}_m \\ \vdots \\ \phi_M^\dagger \sum_{m=1}^{M} \Delta n\psi_m \omega_m^2 e^{-i\omega_m t}\tilde{a}_m \end{bmatrix} \tag{2.31}$$

We can express the mode amplitude a_m in terms of the slowly varying mode amplitude $\tilde{a}_m$: $i\omega_m \dot{a}_m = i\omega_m \dot{\tilde{a}}_m e^{-i\omega_m t} + \omega_m^2 e^{-i\omega_m t}\tilde{a}_m$. Adding $\omega_m^2 e^{-i\omega_m t}\tilde{a}_m$ to both sides of (2.31) and multiplying by $-\frac{i}{n\omega_j}$, we have (for the n th row)

$$\dot{a}_n = -i\omega_n a_n + \frac{i}{n\omega_n}\phi_n^\dagger \sum_{m=1}^{M} \Delta n\psi_m \omega_m^2 a_m$$

Now we can left-multiply by ψ_n, recalling the orthonormality of the eigenvector basis.

$$\dot{a}_n\psi_n = -i\omega_n a_n\psi_n + \frac{i}{n\omega_n}\sum_{m=1}^{M}\Delta n\psi_m\omega_m^2 a_m$$

Substituting in (2.28) for Δ_n and letting $\mathbf{G}$ be a diagonal matrix whose j th entry is $G_j = g\frac{N_j - N_0}{1+s|E_j|^2} - \gamma$, we have:

$$\dot{a}_n\psi_n = -i\omega_n a_n\psi_n + \frac{\pi c(1-i\alpha)}{\omega n}\mathbf{G}\sum_{m=1}^{M}\frac{\omega_m^2}{\omega_n}a_m\psi_m \tag{2.32}$$

We can then let $\omega_m = \Omega + i\nu_m$ where $\Omega = \mathrm{Re}(\omega_m)$ and $\nu_m = \mathrm{Im}(\omega_m)$. Now we invoke two assumptions. First is the single-frequency condition—that $\mathrm{Re}(\omega_m)$ is the same for all m. Second is the assumption that the cavity (the compound resonator) has a high Q-factor—that the modal loss rates are small compared to their frequencies so that $|\nu_m| << |\Omega_m|$ for all m.

$$\frac{\omega_m^2}{\omega_n} = \frac{(\Omega^2 - \nu_m^2) + 2i\Omega\nu_m}{\Omega + i\nu_n} = \frac{(\Omega^2 - \nu_m{}^2)\Omega + 2\Omega\nu_n\nu_m + 2i\Omega^2\nu_m - i(\Omega^2 - \nu_m)\nu_n}{\Omega^2 + \nu_n^2}$$

$$= \frac{\Omega^3 - \nu_m{}^2\Omega + 2\Omega\nu_n\nu_m + 2i\Omega^2\nu_m - i\Omega^2\nu_n + i\nu_m^2\nu_m}{\Omega^2 + \nu_n^2} \approx \Omega$$

Note that a more conservative approximation would be $\frac{\omega_m^2}{\omega_n} \approx \Omega + i(2\nu_m - \nu_n)$. We are assuming here that the modal losses are very small. Then (2.32) becomes:

$$\dot{a}_n\psi_n = \nu_n a_n\psi_n - i\Omega a_n\psi_n + \frac{\pi c\Omega(1-i\alpha)}{\omega n}\mathbf{G}\sum_{m=1}^{M}a_m\psi_m$$

Taking the the sum over n of the above equation (and using (2.30)), we have

$$\dot{\vec{E}} = -i\Omega\vec{E} + \sum_{n=1}^{M}\nu_n a_n\psi_n + (1-i\alpha)\frac{M\pi c\Omega}{\omega n}\mathbf{G}\vec{E}$$

We can now let $\mathbf{K} = \sum_{n=1}^{N}\nu_n\psi_n\phi_n^\dagger$. Observe that because of the bi-orthogonality assumption, $\mathbf{K}\vec{E} = \sum_{n=1}^{M}\nu_n\psi_n\phi_n^\dagger\sum_{m=1}^{M}a_m\psi_m = \sum_{n=1}^{M}\nu_n a_n\psi_n$. Therefore the field equation becomes (now letting $\omega \to \frac{2n}{Mc\pi\Omega}$, since it is a defined parameter):

$$\dot{\vec{E}} = \frac{1-i\alpha}{2}\mathbf{G}\vec{E} - i\Omega\vec{E} + \mathbf{K}\vec{E} \tag{2.33}$$

The ith element of (2.33) then defines the ith laser $E_i = r_i e^{i\theta_i}$. We can now make a coordinate transformation $E_i \to E_i e^{-i\Omega t}$ without any loss of generality (the above equation is invariant under such transformations with constant $\Omega \in \mathbb{R}$. For the ith element we have:

$$\dot{E}_i = \frac{1-i\alpha}{2}\left(g\frac{N_i - N_0}{1+s\,|E_i|^2} - \gamma \right) E_i + \sum_{j=1}^{M} K_{ij} E_j$$

Finally, it seems that the equation we have derived is the conjugate of the one we are looking for. Letting $E_i \to E_i^*$, we have:

$$\dot{E}_i = \frac{1+i\alpha}{2}\left(g\frac{N_i - N_0}{1+s\,|E_i|^2} - \gamma \right) E_i + \sum_{j=1}^{M} K_{ij} E_j \tag{2.34}$$

Now we can let $E_i = r_i e^{i\phi_i}$ to get the full phase equation form used in section 2.3:

$$\dot{r}_i = \frac{1}{2}\left(g\frac{N - N_0}{1+sr_i^2} - \gamma \right) r_i + \sum_{j=1}^{M} K_{ij} r_j \cos(\phi_j - \phi_i) \tag{2.35}$$

$$\dot{\phi}_i = \frac{\alpha}{2}\left(g\frac{N - N_0}{1+sr_i^2} - \gamma \right) + \sum_{j=1}^{M} K_{ij} \frac{r_j}{r_i} \sin(\phi_j - \phi_i) \tag{2.36}$$

and the carrier equation

$$\frac{dN_i}{dt} = J_0 - \gamma_n N_i - g\frac{N_i - N_0}{1+sr_i^2} r_i^2 \tag{2.37}$$

The equations (2.35)-(2.37) are identical to (2.16)-(2.19) except there is no time-delay in the coupling term and there is no detuning between the lasers.

The high Q-factor assumption does not imply that the facet reflectivity of the lasers in the array (between the lasers and the out-coupling cavity) is necessarily high. If the Q-factor of a single laser cavity is high, then indeed it is correct that its facet reflectivity must be high, however if the Q-factor of the compound resonator is high, the implication is that the amount of light energy that escapes the full compound resonator is small compared to the energy stored inside it.

Conclusions

The key result from this derivation is that the eigenvalues of the coupling matrix in equation (2.34), $\mathbf{K}$, are the imaginary parts ν_m of the round-trip operator eigen-frequencies ($\omega_m = \Omega + i\nu_m$). This relationship indeed comes from the fact that we assume that the real parts of the propagator mode frequencies Ω are the same. It could also possible to use a different assumption about the frequencies to generate a different type of coupling matrix. This particular assumption should

hold true for a cavity such as the self-Fourier cavity[85], [135], which is designed to have a single longitudinal frequency.

To our knowledge, this is the first first-principles derivation for the coupled Lang-Kobayashi rate equations for a set of more than two external-cavity coupled semiconductor laser diodes. The purpose of this derivation was initially to verify that the model developed in section 2.2 is consistent. However, the result of the derivation is a new way of understanding how to rigorously integrate traditional first-principles coupled resonator mode modeling [45], [56], [57], [83], [87], [136] with the more recent nonlinear systems approaches used to understand diode laser arrays[12], [39], [59], [106], [128].

2.5 Transverse modes of coupled nonlinear oscillator arrays

In systems of coupled nonlinear oscillators, network topology often determines whether the oscillators will synchronize[6], [90]. Master Stability Function (MSF) [90] provides a framework to understand how perfect synchronization in coupled systems occurs. MSF theory has also been used to understand cluster and group synchronization[91], [93], [97], [137], [138]. While it was alluded to the original paper[90], the MSF has not been used to find the stability of non-phase-synchronous transverse modes. These are states where the relative phases of the oscillators are spatially dependent. Our results show that it is possible to use a simple extension of MSF theory to find the stability of non-phase-synchronous transverse modes in systems of coupled nonlinear oscillators. Transverse mode dynamics are important in a variety of systems such as lasers[1], [65], [88] and neural networks[34], [4], [139]. MSF theory might be a simple way to predict and understand this type of non-synchronous behavior. In this paper, we provide details on how MSF theory can be used to calculate the stability of transverse modes in coupled oscillators and show an application of this theory to arrays of coupled semiconductor lasers.

The problem of synchronization of semiconductor lasers for coherent beam combining is important not only for its applications in laser engineering, but in the study of synchronization in delay-coupled nonlinear dynamical systems. Many solutions of this problem work for very small arrays of lasers[140]–[143], require very specific coupling topologies[97], [106], or result in out-of-phase synchronization[59], [62]. It remains an open problem whether synchronization can be robustly experimentally achieved with large numbers of lasers[12]. Here, we show how understanding of transverse modes and mode selection in lasers can allow us to find ranges of coupling topologies which result in synchrony or spatially organized non-synchronous transverse mode behavior.

We first describe in detail the derivation of stability functions for transverse modes of coupled oscillator arrays. We do this derivation for two systems: a system with additive coupling, which is the simplest case; and a system with time-delayed coupling, which is the case for semiconductor lasers. We then show how this theory can be applied to semiconductor lasers.

We begin by describing in detail how to derive equations for transverse modes in general systems of coupled oscillators. We then provide the derivation of transverse mode stability equations. This derivation is similar to the derivation of the master stability function[90]. Finally, we demonstrate how transverse mode stability can be calculated in systems with time-delayed diffusive coupling, as is the case for many nonlinear systems including semiconductor lasers. This derivation illustrates the key conditions for having a strong transverse mode structure in a coupled oscillator system.

Finding the transverse modes in systems with additive coupling

Consider a coupled oscillator system with M oscillators:

$$\dot{X}_i = F(X_i) + \kappa^f \sum_j K_{ij} C(X_j)$$

Here, C is a $n \times 1$ vector function with n being the dimension of the single oscillator. K determines which parameters of the oscillator give and receive feedback and which feedback function the oscillator uses. $\mathbf{K}$ is an $M \times M$ matrix which describes the coupling between any two oscillators. The single oscillator with only self-feedback has the equation of motion: $\dot{X} = F(X) + \kappa^f C(X)$. We include self-feedback in the $\mathbf{K}$ matrix, making the diagonal elements nonzero. κ^f is the feedback strength. We will only consider diagonalizable matrices $\mathbf{K}$ in this paper. The coupling matrix, if it is diagonalizable, can be decomposed into a set of singular matrices through an eigenvalue decomposition (note that from here, † superscript represents complex conjugate transpose and * superscript represents only complex conjugation). We should be able to find an appropriate basis for this decomposition unless the matrix is defective:

$$\mathbf{K} = \sum_{i=1}^{N} \lambda_i \mathbf{A}_i$$

$$\mathbf{A}_i = V_i U_i^\dagger .$$

where V_i are the right eigenvectors of $\mathbf{K}$ and U_i are the left eigenvectors of $\mathbf{K}$. This way the eigenvalue λ_i determines the contribution of $\mathbf{A}_i$ to $\mathbf{K}$.

If we let $\mathbf{U}$ be a matrix whose columns are U_i and let $\mathbf{V}$ be a matrix whose columns are V_i. We observe that

$$\mathbf{U}^\dagger \mathbf{K} = \mathbf{U}^\dagger \sum_i \lambda_i V_i U_i^\dagger = \mathbf{D}\mathbf{U}^\dagger ,$$

where $\mathbf{D}$ is a diagonal matrix whose entries are the eigenvectors λ_i of $\mathbf{K}$. The full system can have the form:

$\dot{\mathbf{x}} = F(\mathbf{x}) + \kappa^f [\mathbf{K} \otimes \mathbf{I}_n] C(\mathbf{x})$.

where $\mathbf{x} = (X_1,...,X_M)^T$, $F(\mathbf{x}) = (F(X_1),...,F(X_M))^T$, and $C(\mathbf{x}) = (C(X_1),...,C(X_M))^T$. We assume that there is a solution to which each oscillator converges and that the dynamics can be described by small deviations from those oscillations. Therefore we look at the variational equation for the set of variations from synchrony $\xi = (\xi_1,...\xi_M)$, by taking the Taylor expansion of the system to first order with each oscillator synchronized on the solution $\vec{X}^*$ and letting $\xi_i = \vec{X}_i - \vec{X}^*$:

$$\dot{\xi} = [\mathbf{I}_M \otimes D\mathbf{F} + \kappa^f \mathbf{K} \otimes D\mathbf{C}]\xi \qquad (2.38)$$

So the ξ_i represents distance of the ith oscillator from the synchronous solution.

We will now change notation and let $\mathbf{V}_i^j := V_i \otimes e_j^n$ and $\mathbf{U}_i^j := U_i \otimes e_j^n$ (where e_j^n is the unit vector in the j th coordinate's direction in an n-dimensional space). Clearly, $\mathbf{V}_i^j$ form a basis for the space for $\mathbf{K} \otimes \mathbf{C}$. So

$$\xi = \sum_{j=1}^{n} \sum_{i=1}^{M} \delta_i^j \mathbf{V}_i^j$$

Here, $(\delta_i^1,...,\delta_i^n)$ is a vector representing the ith mode's components in the system.

Let $\mathbf{U}' = \mathbf{U} \otimes \mathbf{I}_n$ and let $\mathbf{V}' = \mathbf{V} \otimes \mathbf{I}_n$. We can now transform the system in Equation (2.38) into the basis of the coupling transverse modes.
The ith block of the transformed variational vector is:
$(\mathbf{U}'^{\dagger}\xi)_{(i-1)n+1,(i-1)n+2,...,in} = (\delta_i^1,...,\delta_i^n)$.
Also,
$\mathbf{U}'^{\dagger}[\mathbf{K} \otimes \mathbf{C}] = \mathbf{D}\mathbf{U}^{\dagger} \otimes D\mathbf{C}$
$\mathbf{U}'^{\dagger}[\mathbf{I}_M \otimes D\mathbf{F}] = \mathbf{U}^{\dagger} \otimes D\mathbf{F}$.
So the full multiplication gives a coupled system. We let $\delta_j = (\delta_j^1,...,\delta_j^n)$.

$$\dot{\delta}_j = (\vec{U}_j \otimes \mathbf{I}_n)^{\dagger}(\mathbf{1}_M \otimes D\mathbf{F}) \sum_{i=1}^{M} (V_i \otimes \delta_i) + \kappa^f (\lambda_j U_j^{\dagger} \otimes D\mathbf{C}) \sum_{i=1}^{M} (V_i \otimes \delta_i)$$

This simplifies to
$\dot{\delta}_j = [D\mathbf{F} + \kappa^f \lambda_j D\mathbf{C}]\delta_j$

This shows the variations the system in the direction of its j th transverse mode. If the matrix $[D\mathbf{F}+\kappa^f\lambda_j D\mathbf{C}]$ commutes with its time derivative, then we can use simple linear stability analysis to find its stability: Synchrony is stable with respect to perturbations in the j th mode's direction if all eigenvalues of the matrix $[D\mathbf{F}+\kappa^f\lambda_j D\mathbf{C}]$ have negative real part. However, if the matrix does not commute with its time derivative, then stability can only be determined by finding leading Lyapunov exponent. The leading Lyapunov exponent value as a function of the eigenvalue λ_j is the MSF for the system. If the leading Lyapunov exponent of all modal variational functions are negative, then the synchronized mode should be stable.

Finding the transverse modes in systems with delayed diffusive coupling

In order to better understand semiconductor laser dynamics, we have to ascertain how the MSF changes when we introduce time-delayed feedback and a diffusive coupling term. While in some cases, a system with diffusive coupling can easily be transformed into one with additive coupling, it is not always possible. The time-delay in the system also complicates the calculation of the leading Lyapunov exponent. We begin with the equation:

$$\dot{X}_i = F(X_i)+\kappa^f\sum_{j=1}^{M}K_{ij}C(X_j(t-\tau),X_i)\,.$$

When we linearize this equation, we consider derivative with respect to each variable at time $t-\tau$ as well. It is convenient that time delay is only in the first argument of $C(X_j(t-\tau),X_i(t))$. Then, the variational equation becomes:

$$\dot{\xi}_i = D_i\mathbf{F}\xi_i+\kappa^f\sum_{j=1}^{M}K_{ij}D_1\mathbf{C}\xi_i+\kappa^f\sum_{j=1}^{M}K_{ij}D_2\mathbf{C}\xi_j(t-\tau)$$

Let $\mathbf{G}$ be a diagonal matrix whose ii th entry is the i th row-sum $\sum_{j=1}^{M}K_{ij}$. The variational equation for the full array becomes:

$$\dot{\xi}=[\mathbf{I}_M\otimes D\mathbf{F}+\kappa^f\mathbf{G}\otimes D_1\mathbf{C}]\xi+\kappa^f[\mathbf{K}\otimes D_2\mathbf{C}]\xi(t-\tau)$$

We again use the $\mathbf{U}'$ matrix for transformation, considering its operation on $\mathbf{G}\otimes D\mathbf{C}$. Again, if the row sums of $\mathbf{K}$ are a constant γ^{sum}, then $\mathbf{U}^\dagger\mathbf{G}=\mathbf{Q}=\gamma^{sum}\mathbf{U}^\dagger$ and we have:

$$\dot{\delta}_j=[D\mathbf{F}+\kappa^f\gamma^{sum}D_1\mathbf{C}]\delta_j(t)+[\kappa^f\lambda_jD_2\mathbf{C}]\delta_j(t-\tau) \qquad (2.39)$$

When the row sums are not the same, consider the effect of the operator $\mathbf{Q}$ on mutual orthogonality of the eigenvectors (i.e. $U_i^\dagger\mathbf{Q}V_j$). If the effect is small and $U_i^\dagger\mathbf{Q}V_j=\delta_{ij}$ so that orthogonality is maintained, then we can use Equation (2.39)

for stability analysis. When the linear operator in Equation (2.39) commutes with its time-derivative, we can use the eigenvalues z of the Jacobian matrix, modified to incorporate delay. We find roots of the following transcendental equation in z [144]:

$$\det\left[z\mathbf{I}_n - [D\mathbf{F} + \kappa^f \gamma^{sum} D_1\mathbf{C}] - [\kappa^f \lambda_l D_2\mathbf{C}]\exp(-\tau z)\right] = 0$$

When the roots are in the left side of the complex plane, then the transverse modes decay to zero.

Application: Semiconductor lasers

In order to describe the feedback in coupled semiconductor lasers we use the following equations for dynamics of semiconductor laser arrays[58]:

$$\dot{\mathbf{X}}_i(t) = \mathbf{F}(\mathbf{X}_i(t)) + \kappa^f \sum_{j=1}^{M} K_{ij}\mathbf{C}(\mathbf{X}_j(t-\tau), \mathbf{X}_i(t)) . \tag{2.40}$$

$\mathbf{X}_i$ is the state of the ith laser:

$$\mathbf{X}_i = \begin{bmatrix} r_i(t) \\ \phi_i(t) \\ N_i(t) \end{bmatrix}$$

r_i is the field magnitude, ϕ_i is the phase, and N_i is the number of carriers in the gain medium. The electric field in the ith laser is $E_i = r_i(t)e^{i\phi_i(t)}$. $\mathbf{F}(\mathbf{X})$ is the expression for the time-evolution of the uncoupled laser[58]:

$$\mathbf{F}(\mathbf{X}_i) = \begin{bmatrix} \frac{1}{2}\left(g\frac{N_i(t)-N_0}{1+sr_i^2(t)} - \gamma\right)r_i(t) \\ \frac{\alpha}{2}\left(g\frac{N_i(t)-N_0}{1+sr_i^2(t)} - \gamma\right) + \omega_i \\ J_0 - \gamma_n N_i(t) - g\frac{N_i(t)-N_0}{1+sr_i^2(t)}r_i^2(t) \end{bmatrix}$$

$$\mathbf{C}(\mathbf{X}_j(t-\tau), \mathbf{X}_i(t)) = \begin{bmatrix} r_j\cos(\phi_j(t-\tau) - \phi_i(t)) \\ \frac{r_j(t-\tau)}{r_i(t)}\sin(\phi_j(t-\tau) - \phi_i(t)) \\ 0 \end{bmatrix}.$$

In the equations, α is the line-width enhancement factor, γ is photon decay rate, γ_n is carrier decay rate, J_0 is the injected current level, which is set to a times the threshold current to turn on the laser. The delay time is τ, κ^f is the

feedback strength, g is the differential gain coefficient N_0 is the number of carriers at transparency, and s is the gain saturation coefficient. For identical lasers, $\omega_j = 0$ for all j. We show the values of these parameters in Table 2.1.The value for κ^f is treated as an order parameter, so we specify its value for each computation. We assume that the lasers are weakly coupled, so that the coupling can be added as a linear perturbation with magnitude κ^f, and that there is just a single time-delay for the entire external cavity. We also assume here that the lasers are identical, although it is still possible to apply MSF theory and our extension to it when the lasers have detuned frequencies. Details of application of MSF theory to slightly disordered systems can be found in [108] and it is straightforward to combine this procedure with the one in this paper.

Table 2.1. Parameters of semiconductor laser model

Parameter	**Value**
α	5
γ	0.5ps^{-1}
γ_n	0.5ns^{-1}
a	4.0
τ	3.0ns
g	1.5*10^{-8} ps
s	2*10^{-7}
N_0	1.5*10^{8}

Here, we consider a decayed non-local coupling matrix for M lasers where $K_{ij} = \frac{1}{M} d_x^{|i-j|}$.

We can linearize and transform the equation as we did in the previous section to get the modal variational function for the j th mode. Note that for our purposes, we will use $\gamma^{sum} = \lambda_1$.

$$\dot{\delta}_j = [D\mathbf{F} + \kappa^f \lambda_1 D_1 \mathbf{C}]\delta_j(t) + [\kappa^f \lambda_j D_2 \mathbf{C}]\delta_j(t-\tau) \quad (2.41)$$

Here, we note that the linearized equation for the single semiconductor laser with self-feedback κ' is:

$\dot{\xi} = [D\mathbf{F} + \kappa' D_1 \mathbf{C}]\xi(t) + [\kappa' D_2 \mathbf{C}]\xi(t-\tau)$.

This means that the modal variational equation for the first mode (with eigenvalue λ_1) is the same as the variational equation of a single laser with feedback strength $\kappa' = \kappa^f \lambda_1$. Consequently, in order to determine the modal

stability in the laser system we need to calculate the eigenvalue and eigenvector spectrum of the matrix $\mathbf{K}$.

In Figure 2.15, we show the eigenvalues of the matrix $\mathbf{K}$ for a 60 laser array with varying d_x value. It is clear that when $d_x \in (0,1)$, the eigenvalues are positive and ordered. We can arrange the eigenvalues and vectors in such a way that $\lambda_1 > \lambda_2 > ... > \lambda_M$. It is clear that when $d_x \to 1$, all eigenvalues $\lambda_{i\neq 1}$ go to zero while $\lambda_1 \to 1$. When $d_x = 0$, the matrix becomes an identity matrix and $\lambda_i = \frac{1}{M}$ for all i. Since the considered matrix $\mathbf{K}$ is symmetric positive definite, the left eigenvectors are the same as the right eigenvectors and the eigenvectors are mutually orthogonal.

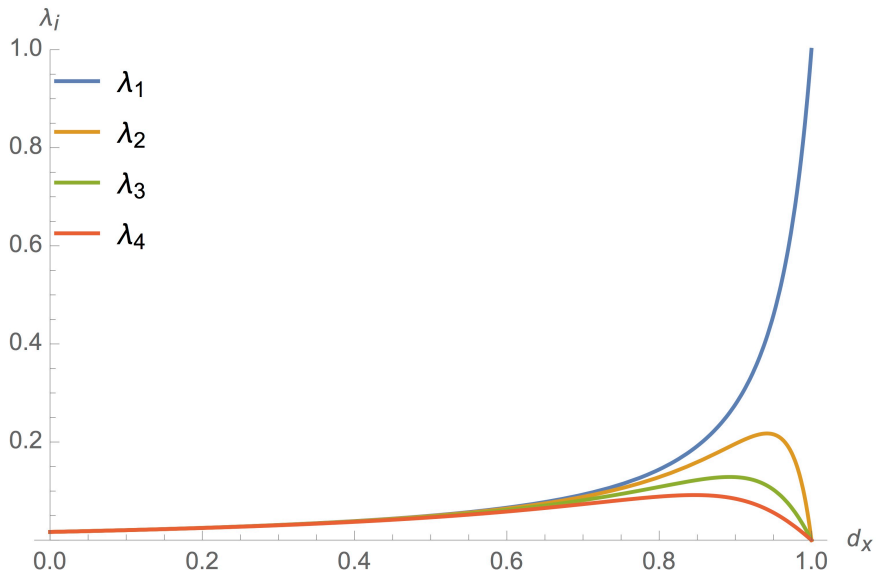


Figure 2.15. First four coupling eigenvalues λ_{1-4} as a function of d_x for a 60 laser array. For $d_x < 1$, $\lambda_1 < M$ and $\gamma^{sum} < 1$. We can see that when $d_x = 1$ the coupling matrix becomes singular and the coupling is perfectly all-to-all.

Figure 2.16 shows the corresponding first four eigenvectors V_{1-4} of an array with $d_x = .3$. The first mode is curved, but we observe that the curvature of the mode is such that the array remains close to synchrony on this mode. We also observe that the ith mode has i extrema. The higher modes for $i > 4$ behave in the same way as the first four modes, i.e. the nth mode has n extrema.

For our analysis, we consider the single laser fixed-intensity fixed-frequency

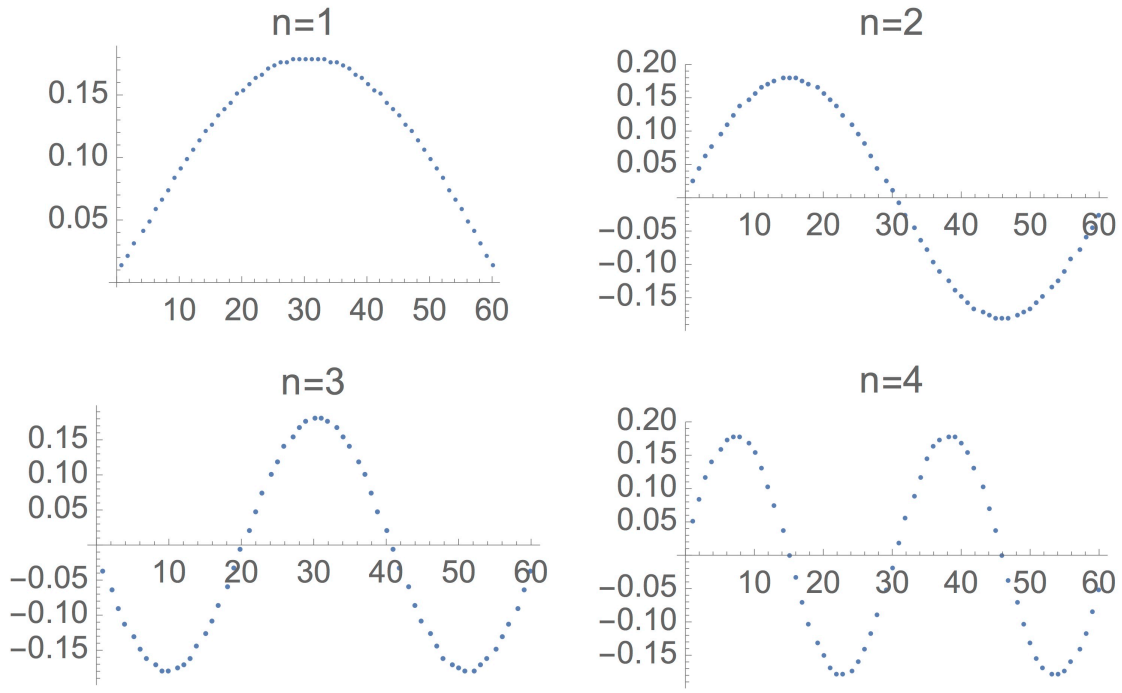


Figure 2.16. The first four eigenvectors of for a 60 laser array with $d_x = .3$. The horizontal axis represents the position in the array and the vertical axis is the value of the vector array entry for that laser. The modes are similar for other values of d_x. We denote the modes by an approximate wavenumber n with the leading mode (with largest in magnitude eigenvalue) being the $n = 1$ mode. Since the matrix G is a symmetric matrix, these modes are orthogonal.

solution to Equation (2.40) with $M = 1$. Since there is a single laser, we use $X_i = X_j$. In finding solutions we drop subscript. There exists a solution with constant $N = N^*$, constant $r = r^*$ and a fixed frequency $\dot{\phi} = \Omega$. This can be found by setting derivatives to zero and solving in the usual way. The solution satisfies the following system of equations:

$$r^* = \sqrt{\frac{g(N^* - N_0)}{\gamma s - 2s\kappa^f \cos(-\Omega\tau)} - \frac{1}{s}} \tag{2.42}$$

$$N^* = \frac{a\gamma_n(N_0 + \frac{\gamma}{g}) + \frac{gN_0 r^{*2}}{1 + sr^{*2}}}{\gamma_n + \frac{gr^{*2}}{1 + sr^{*2}}} \tag{2.43}$$

$$\Omega = \frac{\alpha}{2}(g\frac{N^* - N_0}{1 + sr^{*2}} - \gamma) + \kappa^f \sin(-\Omega\tau) \tag{2.44}$$

We linearize about this solution to derive a numerical form of the modal variational function for all of the modes, the functional form of which is given in Equation (2.41). In Figure 2.17, we plot the leading stability eigenvalue (that with the largest real part) of the linear operator $[D\mathbf{F} + \kappa^f \lambda_1 D_1 \mathbf{C}] + [\kappa^f \lambda_j D_2 \mathbf{C}]$. Here, derivatives are evaluated at the solution given in Equations (2.42), (2.43), (2.44).

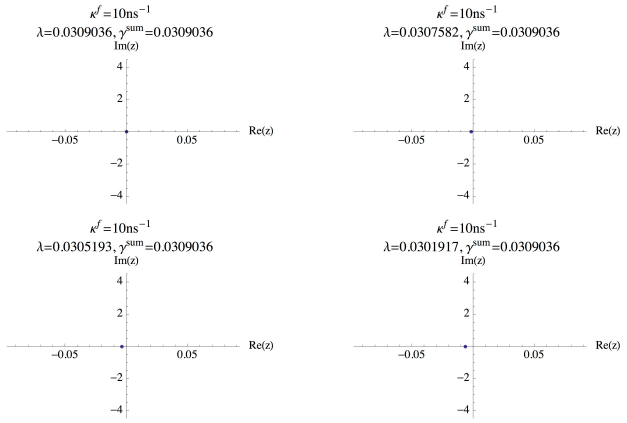


Figure 2.17. Root loci of first four mode stability functions of a 60 laser array with $d_x = .3$ and $\kappa^f = 10\,\mathrm{ns}^{-1}$. λ_i denotes the eigenvalue and $\gamma^{sum} = \lambda_1$ denotes average row sum. The eigenvalues are ordered in decreasing order. The first mode has the largest eigenvalue and the last mode has the least eigenvalue.

We make this calculation for $j = 1,2,3,4$. The figure shows that all modes have stability eigenvalues with negative leading real part. The first mode has a zero

stability eigenvalue, implying that the first mode is either neutrally stable or decaying.

It is important to note two observations. First, only the first mode has a possibly non-decaying solution implying that the dynamics of the laser array that are parallel to the first eigenvector do not decay. Second, the stability of a mode, as given by solving Equation (2.41) does not depend on the eigenvector associated with the mode, but rather only the eigenvalue. To test the theory, we will therefore create alternate matrices that have the same eigenvalue spectrum as $\mathbf{K}$ but different eigenvector spectrum. We can decompose the coupling matrix $\mathbf{K}$ into a set of bi-orthogonal eigenvectors. In this case the eigenvectors of $\mathbf{K}$ and $\mathbf{K}^{\dagger}$ are the same, since $\mathbf{K}$ is symmetric. We call these eigenvectors V_i with eigenvalues λ_i. The decomposition is of the following form:

$$\mathbf{K} = \sum_{i=1}^{M} \lambda_i V_i V_i^{\dagger} = \lambda_i \mathbf{A}_i$$

where $\mathbf{A}_i$ is a projection matrix for the i th mode. So the leading mode for $\mathbf{K}_i$ has the i th eigenvector.

If we re-weight the projection matrices $\mathbf{A}_i$ which compose $\mathbf{K}$ by switching the eigenvalues, we can make n th eigenvector correspond to the largest (first) eigenvalue. We do this by switching the n th and the first eigenvalues:

$$\mathbf{K}_n = \lambda_n \mathbf{A}_1 + \lambda_1 \mathbf{A}_n + \sum_{i=2}^{n-1} \lambda_i \mathbf{A}_i + \sum_{i=n+1}^{M} \lambda_i \mathbf{A}_i .$$

Using this re-weighted matrix $\mathbf{K}_n$, we force the lasers in the array to configure themselves according to the leading eigenvector V_n. This is shown in Figure 2.18. The analytical results presented in Figure 2.17 show that the mode with the largest eigenvalue should be the only non-decaying mode in the dynamics. In Figure 2.18, we simulate arrays of 60 lasers using the coupling matrices $\mathbf{K}_{1-4}$. The results confirm the analytical results.

In Figure 2.18 we can observe that regardless of the leading eigenvector form in the coupling matrix, the mode with the largest eigenvalue (i.e. the only mode that has neutral stability) appears in the relative phases of the lasers in the array. Furthermore, we can observe that using the original $\mathbf{K}_1$ coupling matrix, the phases appear to be perfectly synchronized. Even though the first eigenvector does not represent perfectly synchronous mode, the phases of the lasers do synchronize almost perfectly. There is a very slight curvature in the phases, but it is orders of magnitude smaller than the period of the phasing so it does not significantly affect coherence. This type of approximate synchronization might be

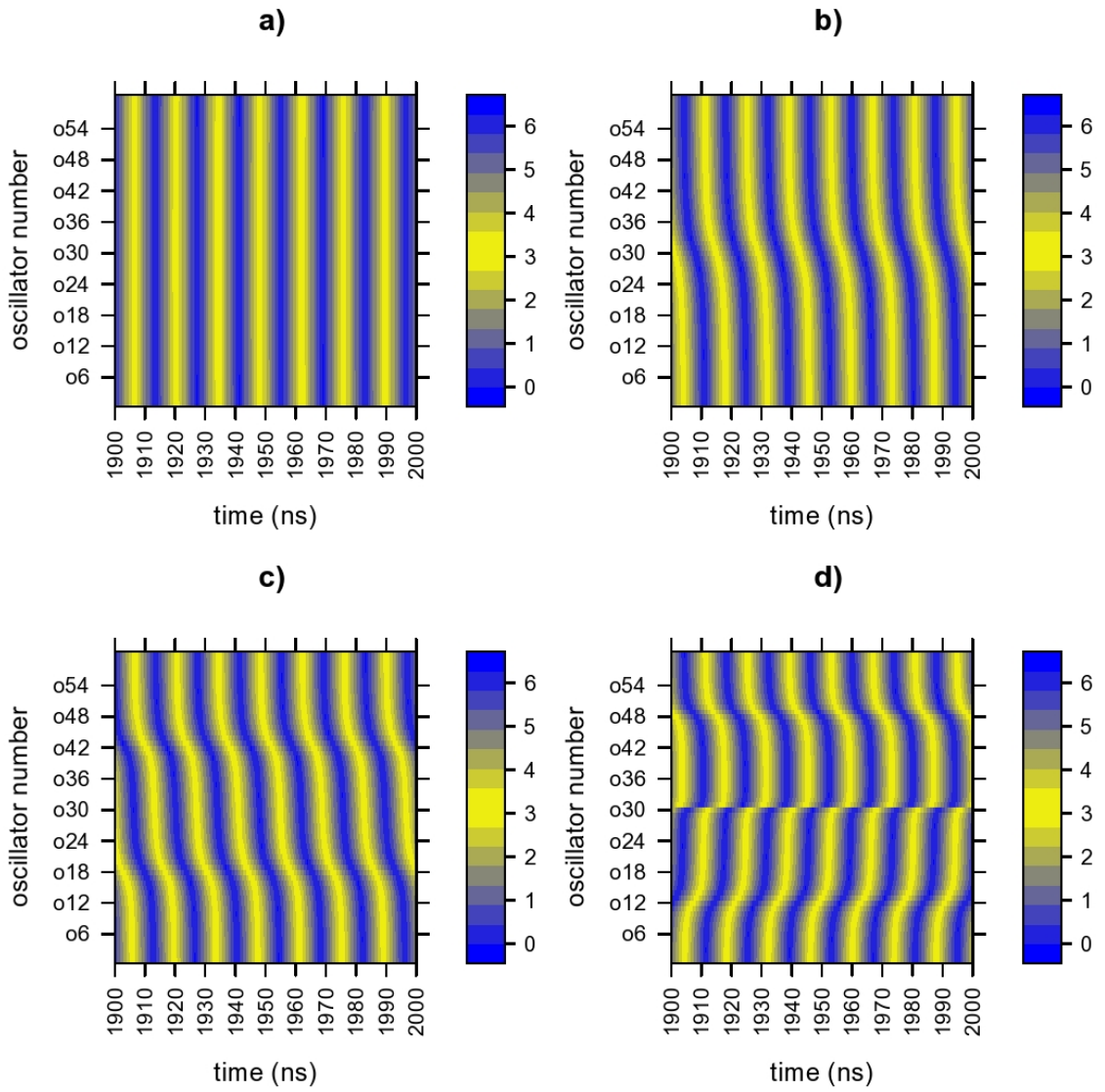


Figure 2.18. Phase plots of arrays of 60 lasers coupled by (a) $\mathbf{K}_1$, (b) $\mathbf{K}_2$, (c) $\mathbf{K}_3$, and (d) $\mathbf{K}_4$. Here, $d_x = .3$ and $\kappa^f = 10\,\mathrm{ns}^{-1}$. The color represents phase value between 0 and 2π. Note that the convergence to the leading mode is not exact; there is just resemblance in clustering.

a step towards solving the problem of synchronization of large arrays of lasers.

Conclusions

We have shown how to apply MSF theory to determine the stability of non-phase-synchronous transverse mode states of coupled oscillator arrays. This is a very simple extension of the theory, but it might be useful in understanding and predicting the behavior of larger coupled oscillator networks.

It is well-known for external cavity coupled lasers that the resonator modes of the external cavity can be used to define the phase behavior of the array as long as the lasers are identical and the nonlinearities in the gain medium of the lasers are not too strong[1], [45], [65], [88]. The mode with the least loss should last while the others decay. However, the connection between this type of mode selection in laser cavities and mode selection in coupled nonlinear oscillators has never been discussed to our knowledge. Furthermore, mode selection has not been understood through the lens of MSF theory.

2.6 An application to associative memory dynamics

Neurons are often modeled or understood as arrays of coupled oscillators (ordinary differential equations)[20], [145]. It has been shown that by using the phase response curves some neuron models can be reduced to simpler phase oscillator models such as Kuramoto model [7], [37], [43], [89], [146] when the system operates on a stable limit cycle[37], [147]. Many theories of how neurons compute involve Hebb's rule that ``neurons that fire together wire together'' [148], [149]. Experiment based coding theories of spike correlations have been derived from experimental results, but with little connection to more mechanistic dynamical models[150], [151]. Attempts have also been made at using physical oscillator systems to implement Hebb's rule with oscillator-based Hopfield type networks[34], [139], [152]. This might be useful for building hardware systems of oscillatory pattern recognizers with systems like lasers or analog circuits (many instances of which have also been tried or proposed)[88], [153], [154]. Here, we (1) show how Hebb's rule could manifest itself in networks of actively coupled Hindmarsh-Rose neurons or Kuramoto oscillators[89], [145], and (2) propose a new method for associative pattern recognition, implemented on Kuramoto oscillators, which is similar to[88], but elucidates the pattern recognition mechanism perhaps more directly.

Mode selection in oscillatory neuron networks

Our motivation is to understand how the behavior of oscillatory neuron networks could produce associative memory. Hebb's rule is usually thought of as the statement that firing together implies wiring together. Firing together likely means

in-phase synchronization. In this paper, we consider a different type of synchronization (i.e. not in-phase) that may arise due to the coupling (wiring) in the network. So the wiring in the network may result in correlations between the elements of the network. Wiring, or synaptic connections, can be mathematically represented by the coupling matrix used to connect the system of oscillators. In particular, we can visualize the correlations by looking at the eigenvectors of the connectivity matrix.

In many cases (i.e. unless the matrix is defective) the connectivity matrix $\mathbf{K}$ can be decomposed into a set of outer products (its eigenvalue decomposition):

$$\mathbf{K} = \sum_{j=1}^{N} \lambda_j \vec{U}_j \vec{V}_j^T. \tag{2.45}$$

where N is the number of neurons, and λ_j is replaced by zero for eigenvectors in the null space of $\mathbf{K}$. Here, $\vec{U}_j$ are eigenvectors of $\mathbf{K}$ and $\vec{V}_j$ are eigenvectors of $\mathbf{K}^T$. Here, we consider an idealized system where $\vec{U} = \vec{V}$ so that the coupling matrix is symmetric. We use $\mathbf{K} = [k_{ij}] = [\frac{1}{N} d^{|i-j|}]$, where $d = .9$. This coupling gives strong local activity with weak, but existent nonlocal activity. Such a coupling form has been used to synchronize laser arrays because of this property [39]. We expect that our results will also be valid for non-symmetric coupling.

We consider two networks. First, a network of actively coupled Hindmarsh-Rose oscillators described by Equations (2.46) and (2.47) [145]. In these equations, we neglect the usual damping term z so that all oscillations are self-sustaining[145]:

$$\dot{x}_i = a x_i^2 - x_i^3 + y_i + I_i + \kappa_x \sum_{j=1}^{N} k_{ij}(x_j - x_i) \tag{2.46}$$

$$\dot{y}_i = 1 - b x_i^2 - y_i + \kappa_y \sum_{j=1}^{N} k_{ij}(y_j - y_i) \tag{2.47}$$

where the coordinates are dimensionless. Here, x_j is the membrane potential of the j th neuron and y_j is the ion current across the membrane. κ_x and κ_y are global coupling strengths and k_{ij} represent synaptic connectivity between the i th and j th neurons. k_{ij} is the ij th element of the matrix $\mathbf{K}$. I_j is the external current, and a and b are constant parameters. We use $a = 1$, $b = 3$, $\kappa_x = \kappa_y = 1$, and $I_j = 4$ for all j.

The second network we consider is a network of Kuramoto oscillators[89]. We use the same coupling matrix $\mathbf{K}$. For simplicity, we use the $\sin$ function for a phase resetting curve. The oscillator equation is:

$$\dot{\theta}_i = \Omega + \sum_{j=1}^{N} k_{ij} \sin(\theta_j - \theta_i). \quad (2.48)$$

where $\vec{\theta}$ is the state vector with ith element $\theta_i \in [0, 2\pi)$. $\Omega = 1$ is the natural frequency for the Kuramoto oscillator.

The dynamics of the Hindmarsh-Rose, Kuramoto, and other models, when at a limit cycle, can be decomposed into a set of modes, described by the eigenvectors $\vec{V}_i$, and correspond to different types of synchronization. When λ_j are real (from Equation (2.45)), the largest eigenvalue λ_1 (we impose this ordering) tends to dominate-- that is, the first transverse mode appears in the dynamics of both oscillator systems. This can be understood through an extension of master stability function theory[3], [90]. We do not include this analysis here. We illustrate this behavior with numerical simulations. The matrix $\mathbf{K} = [k_{ij}]$ is a symmetric matrix with leading eigenvectors with simple mode structure shown in Figure 2.19 parts a-1,b-1, and c-1. The modes shown in Figure 2.19 are from the matrices $\mathbf{K}_j$ with the j th forced leading mode by switching eigenvalues and eigenvectors as follows:

$$\mathbf{K}_j = \lambda_1 \vec{V}_j \vec{V}_j^T + \lambda_j \vec{V}_1 \vec{V}_1^T + \sum_{i=1, i\neq j}^{N} \lambda_i \vec{V}_i \vec{V}_i^T$$

The systems converge to modes that are represented by the eigenvector of the matrix with the largest eigenvalue. For the Hindmarsh-Rose neurons, we show this in Figure 2.19 parts a-2,b-2,c-2. For the Kuramoto oscillators, this is in Figure 2.19 parts a-3, b-3, and c-3. So a system with matrix $\mathbf{K}_j$ converges to a mode that approximates the structure of $\vec{V}_j$. We have also found that changing the parameters a and b in the Hindmarsh-Rose neurons and applying a sinusoidal current can also lead to in- and out- of phase bursting patterns, while still adhering to the basic transverse mode structure dictated by the leading eigenvectors. We show this behavior in Figure 2.20. This is to illustrate that mode selection is a general property.

We can use the Karhunen-Loeve (KL) decomposition to observe exactly how the phasing and connectivity are correlated[155]. The KL eigenvectors are the eigenvectors of the correlation matrix for the vector $\vec{x} = (x_1, ..., x_N)$ in the Hindmarsh-Rose case and $\vec{\theta} = (\theta_1, ..., \theta_N)$ in the Kuramoto case. Figure 2.21 shows the leading KL eigenvectors $\vec{v}_1^h$ of the x value time series and $\vec{v}_1^k$ of the θ value time series plotted with the leading eigenvectors $\vec{V}_1$ of the coupling matrix. We can see that the continuous mode structure is qualitatively discretized

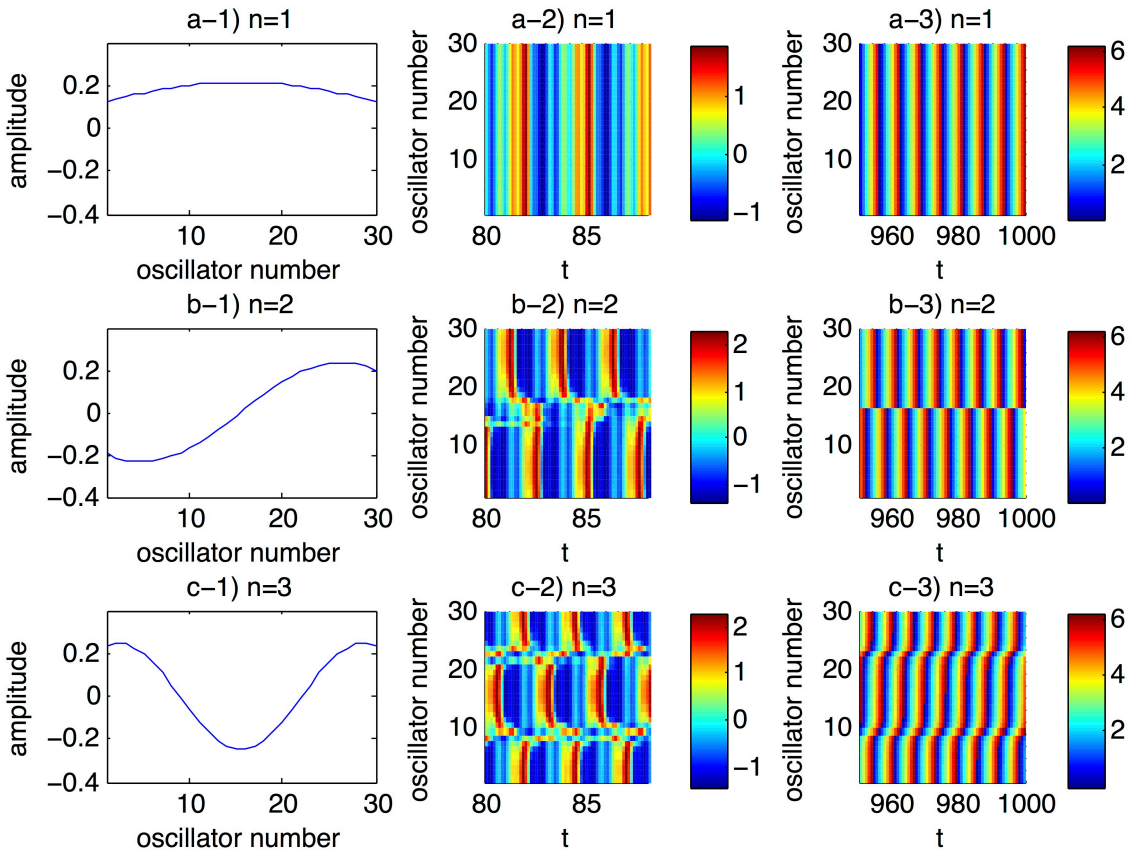


Figure 2.19. The first eigenvectors of the matrices $\mathbf{K}_n$ for $n=1$ (a-1), $n=2$ (b-1), and $n=3$ (c-1) are shown with corresponding Hindmarsh-Rose simulations ((a-2), (b-2), and (c-2)) and the corresponding Kuramoto oscillator simulations ((a-3), (b-3), and (c-3)) using these matrices. Note that the mode structure corresponds to the number of synchronized clusters.

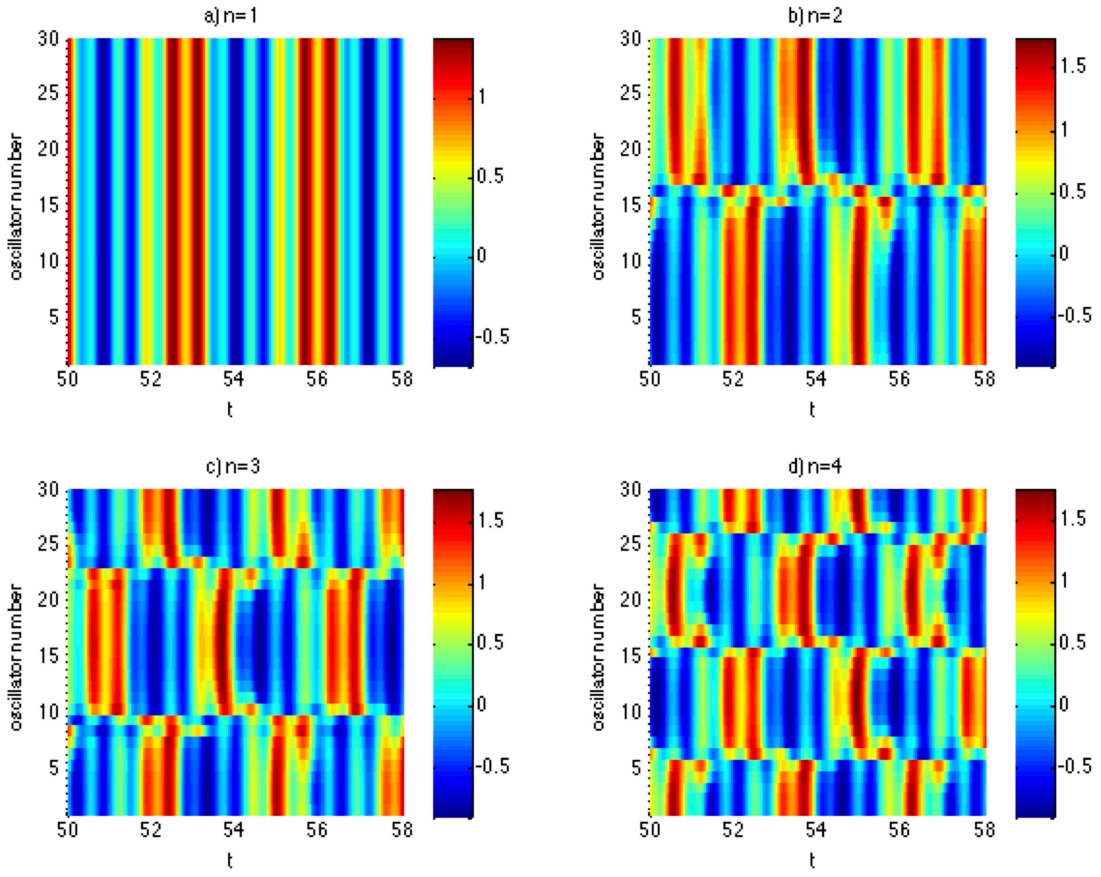


Figure 2.20. The x time-series for 30 neurons are plotted with $a = 3$ and $b = 5$, illustrating two-spike bursting in synchronized clusters, using the first four mode adjacency matrices $\mathbf{K}_n$, $n = 1,...,4$. Note that the mode structure corresponds to the number of synchronized clusters.

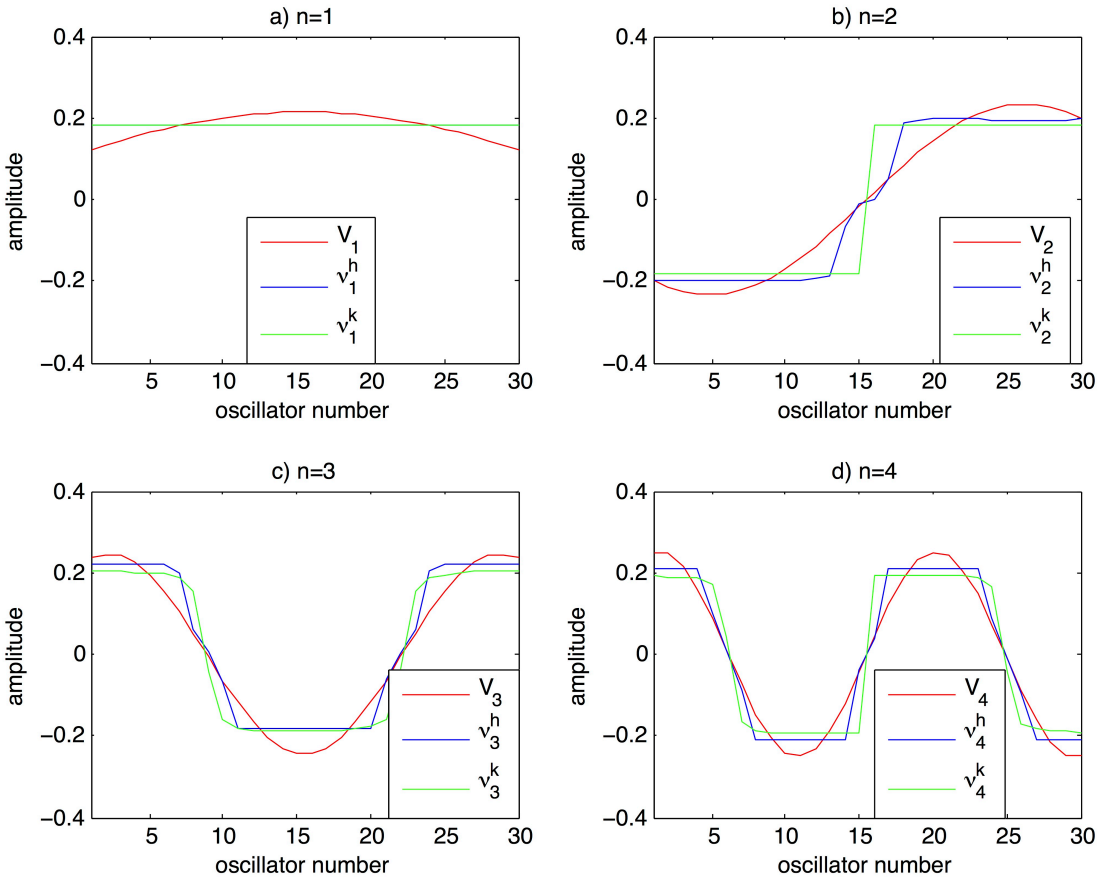


Figure 2.21. The first four eigenvectors of the matrices $\mathbf{K}_n$ for $n=1$ (a), $n=2$ (b), $n=3$ (c) and $n=4$ (d) are shown with corresponding KL eigenvectors v_i^h (for Hindmarsh-Rose) and v_i^k (for Kuramoto) calculated from simulations. In all of these cases, the correlation matrices are very close to singular. In fact, the only KL eigenvectors that correspond to any of the matrix eigenvectors $\vec{V}_i$ are the dominant ones-- that is, the system selects only the leading mode; not a superposition of leading modes.

naturally by both Hindmarsh-Rose neurons and Kuramoto oscillators. This is interesting because it could mean that `fuzzy' states between in- and out-of-phase are not dynamically preferred with these neurons when they are in this simple non-bursting state. Computationally, this could mean that there is a preference for *binary* memory vectors in these cases.

Associative memory model

In the Hindmarsh-Rose neuron networks and the simpler Kuramoto oscillator networks, we have shown that the correlations in the dynamics of the neurons correspond to the structure in the eigenvectors of the connectivity matrix-- we have observed a simple instance of Hebb's rule taking place.
Therefore, we model Hebbian associative memory using binary memory vectors, in a similar way as Hopfield[34]. Both the Kuramoto model and the Hindmarsh-Rose model exhibit mode selection. Here, we use the only the Kuramoto model for our implementation. The oscillator equation is as in Equation (2.48). In order to implement Hebb's rule, we let k_{ij} come from a matrix $\mathbf{K}$ of the form:

$$\mathbf{K} = \sum_{j=1}^{N} \lambda_j(t) \vec{V}_j \vec{V}_j^T$$

The eigenvalues depend on the inner products of the binary `memory' vectors $\vec{V}_j$ with a normalized state vector $\frac{1}{2\pi}\vec{\theta}$. Despite the fact these memory vectors are not necessarily orthogonal, we will continue to refer to the set as eigenvalue and vector pairs for simplicity of notation.

$$\lambda_k(t) = \frac{1}{2}(1 - \cos(\pi \chi_k(t))) \tag{2.49}$$

where

$$\chi_k(t) = | \vec{V}_k^T \frac{\vec{\theta}(t)}{2\pi} |$$

and is the normalized inner product between the memory and state. Essentially, χ_k tells us how much the current state of the system resembles the k th memory. Equation (2.49) is chosen because it maps the interval [0,1] to [0,1] with $\lambda(x) \geq x$ for $x \in [.5,1]$ and $\lambda(x(t)) \leq x(t)$ for $x(t) \in [0,.5]$. Because of the normalization $\chi_k \in [0,1]$. This function is somewhat arbitrary, and other, functions that are physiologically more relevant could be chosen.

As shown in the previous section, the modes to which the neurons converge are represented by the largest eigenvalue. This model of associative memory takes advantage of this property by allowing the connectivity matrix eigenvalue

spectrum to mirror the eigenvalue spectrum (in the basis of the memory vectors) of the state vector.

We simulate the ODE in Equation (2.48) with $\Omega = 1$ for 2000 oscillations (we measure time by `oscillations' since the units of this equation are dimensionless and frequency is normalized to 1). We use the simple forward Euler scheme to do the simulations. This system has an interesting property that, for randomly generated binary memory vectors, patterns are stable for very high numbers of imprinted memories. That is, when we start on one of the patterns $\vec{V}_i$, it persists, losing information very slowly, but is still totally readable after 2000 oscillations. This happens simply because if $\vec{\theta} / 2\pi \| \vec{V}_i$, then clearly $\lambda_i = 1$ and $\lambda_{j \neq i} < 1$, so the selected mode dominates. Figure 2.22 shows this behavior.

To illustrate the fact that pattern recognition does indeed occur with this network, we consider a network of 40 neurons. We select a pattern and let the initial condition $\vec{\theta}_0 = 2\pi\vec{V}_i + \vec{\eta}$, where $\vec{\eta}$ is a vector of bit-flip errors (magnitude π) with a specified number of errors (Hamming distance). We measure convergence by taking the signs of the dominant KL eigenvector $\text{sign}(\vec{v}_i)$ and comparing this to the signs of the memory $\vec{V}_i$ from which the initial condition was corrupted. Figure 2.23 shows this for various values of M, number of memories. This is a test of network's ability to complete patterns and do pattern association.

Having 10 memorized patterns stably working in a 40 neuron network would seem to give a ratio which is greater than the .138 ratio calculated to be the capacity of a traditional Hopfield network [156]. However, given that the associative property of the eigenvalue is forced, this might be expected. A more rigorous calculation of memory capacity for this sort of network is necessary in order to understand how useful this type of system could be in artificial intelligence. However, we have shown that this form of pattern recognition works properly and is relatively stable for binary valued memories. The fact that this system works significantly better for binary valued memories than for memories with less ordered phase differences highlights the fact that continuum systems can display discrete behavior and that, in fact, binary behavior could take place in the same way in actual neural systems.

Conclusion

We have shown that in networks of Hindmarsh-Rose neurons, Hebb's outer product rule functions in an obvious way, in that we can force convergence to the a state corresponding to the leading eigenvector of the connectivity matrix by weighting the eigenvalues accordingly. We have also presented a method of Hebbian learning through a sort of eigenvalue modification where connectivity is

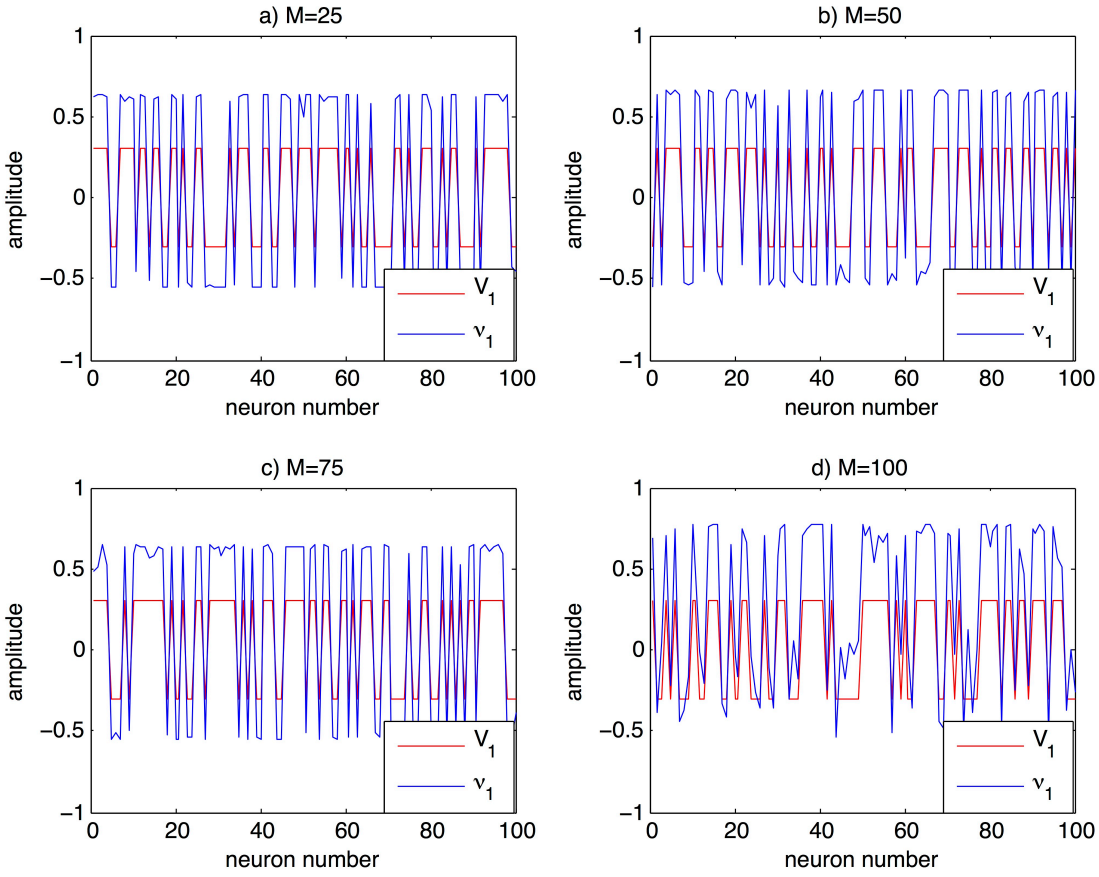


Figure 2.22. Initial state eigenvectors $\vec{V}_1$ and dominant Karhunen-Loeve eigenvectors for the last 10 oscillations ν_1 are plotted for various numbers of imprinted memories M. The memories are randomly generated from uniform distributions of binary values. The initial vector corresponds to one of the memories. Note that in all cases, the memory remains stable, despite the distortion for $N = 100$ (d). In this case, $\text{sign}(\cos(\vec{\theta})) = \text{sign}(\vec{V}_1))$, though it is difficult to see.

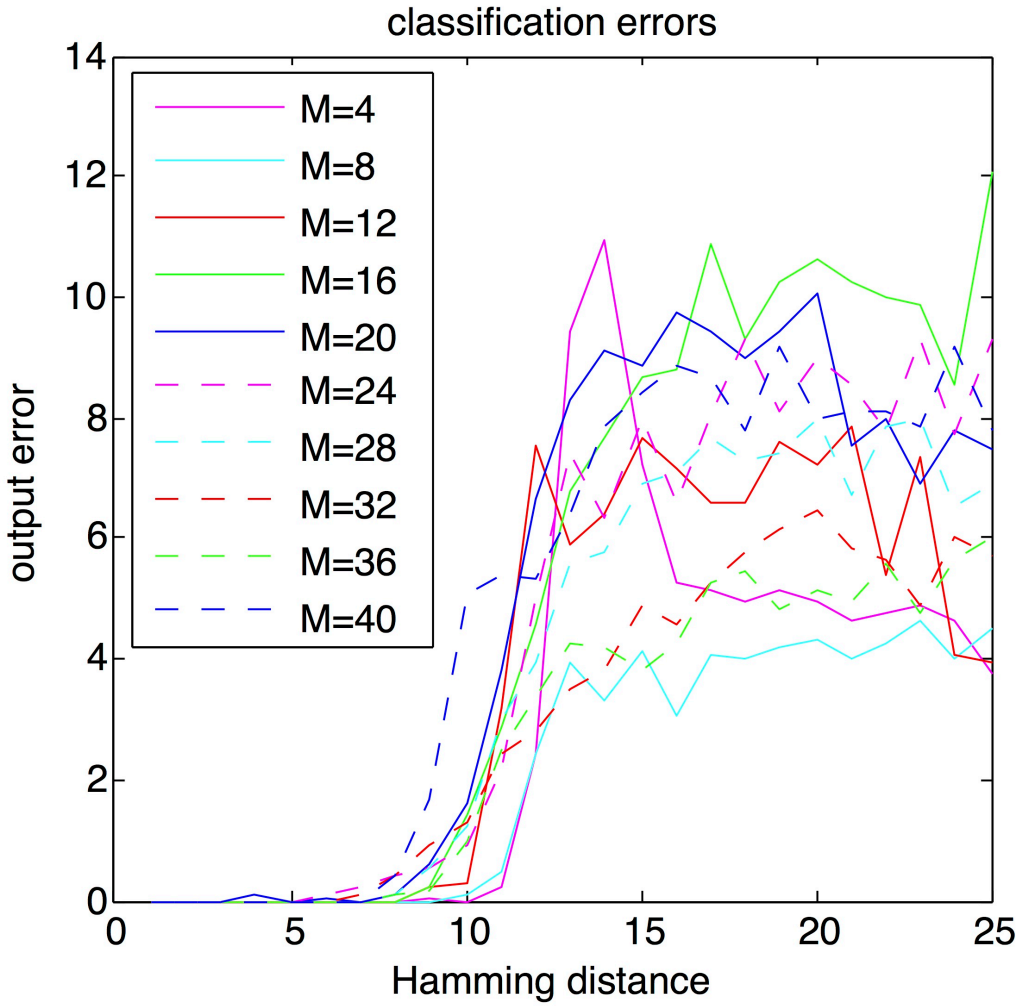


Figure 2.23. The average classification error is shown against number of flipped bits in the initial condition (averaged over 50 trials). We can see that for up to 5 flipped bits, convergence still occurs perfectly for most values of M. Also, convergence seems to be more accurate with lower values of M.

modified based on the correlation between the memory vector and the state of the neuronal network.

These models are simple, but they exhibit rich and useful dynamics. In fact, the modification of transverse modes of Hindmarsh-Rose neurons give an extremely simple way to understand neural rhythm formation. The asynchronous, but phase-locked states also give a simple basis for the proposed `central pattern generator' networks and other sources of neural rhythms[157]. Our result shows also that the relationship between eigenvectors of the network (which could be measured via Karhunen-Loeve decomposition of correlations between neurons) could be deeply connected to pattern recognition and mental states, as observed in[158]. It might be useful to look for a mathematical connection between this simple mechanism for Hebbian associative memory and the more complex, but more biologically accurate method of spike-timing-dependent synaptic plasticity[149].

CHAPTER THREE

CRYOGENIC COMPUTING WITH JOSEPHSON JUNCTIONS

This chapter is based on work that the author of this dissertation has been co-author on [159], [160]. Section 3.2 is an edited version of a submitted paper that the author has written [161].

3.1 Motivation

Design of an efficient cryogenic computing system seems to be a possible way of achieving energy-efficient exascale computing [162]–[164]. Cryogenic computers are based on superconducting circuits that operate at around 4 Kelvin. They are now being considered as a possible alternative to CMOS computing because the time-scale and energy-scale in which the circuits operate are both very small (~1ps and ~10^-19 J respectively)[164].

Rapid single flux quantum (RSFQ) computing is a digital electronic technology that stores information in the form of magnetic flux quanta in superconductor loops. The quanta are transferred between circuits as single flux quantum (SFQ) voltage pulses. A family of RSFQ circuits has been developed to perform all basic logic operations to build a functioning computer [165]. These logic operations involve passing the SFQ pulses through circuits between clock pulses which can operate at frequencies of over 700 GHz [164], [166]. A key challenge in designing RSFQ based computers is random access memory storage (RAM). Memory units of up to 4kb have been demonstrated[167]–[170]. However, it has been difficult to build units larger than this because of energy dissipation problems in current memory cell design.

In this chapter, we will introduce a new design for a ternary superconducting memory circuit that is compatible with SFQ logic that has properties that suggest that it is more energy efficient than current designs. This circuit is based on fixed-point states of an array of three Josephson junctions. Though its operation is simple, it is an elegant and potentially very useful application of classic fixed-point analysis of a nonlinear system.

3.2 Background: Josephson junctions and the model for a resistively shunted Josephson junction

Below a critical temperature, dependent on materal properties, many metals can become superconductors—the electrical resistance in the metal goes to zero. Therefore, little energy is dissipated when sending electrical signals through

superconducting wires. A Josephson junction is (usually) comprised of a thin insulating layer between two superconducting wires. When there is a voltage across the junction, it is possible for electrons (Cooper pairs) to tunnel through the barrier[171], [172]. To introduce the dynamics of small Josephson junctions, we derive the equations of motion for a resistively shunted small Josephson junction. This derivation follows from [171] and uses ideas from [173], [174] to complete the derivation. Though this is a well-known derivation, it is useful to present in order to understand the meaning of the RSJ equations that we rely on in this chapter.

Derivation of the Resistively Shunted Junction (RSJ) equation

Consider a Josephson junction with a voltage $V(t)$ applied across the insulating layer. The macroscopic wave-function [171], [175], [176] of the Cooper pair population in this system (the two superconducting sides and the insulator) can be written as $\Psi = \psi_1 |1\rangle + \psi_2 |2\rangle$. The state $|i\rangle$ represents a state where all electrons are on one side of the junction. We are assuming that both sides are of identical material and that there are no external magnetic fields. The two amplitudes ψ_1, ψ_2 ($\in \mathbb{C}$) evolve by the time-dependent Schrödinger equation:

$$i\hbar \frac{\partial \psi_1}{\partial t} = U_1 \psi_1 + K\psi_2$$

$$i\hbar \frac{\partial \psi_2}{\partial t} = U_2 \psi_2 + K\psi_1 \qquad (3.1)$$

where K is a term characteristic to the junction (related to its material properties) and U_i is the potential energy of the ith state. We can let $\psi_i = \sqrt{\rho}_i e^{i\theta_i}$, where ρ_i is the particle probability density of the Cooper pairs in the i state and θ_i is the phase of the ith wavefunction. Simplifying equations (3.1) using this representation, we have

$$\frac{\partial \psi_i}{\partial t} = \frac{1}{2\sqrt{\rho_i}} \frac{d\rho_i}{dt} e^{i\theta_i} + i \frac{d\theta_i}{dt} \sqrt{\rho_i} e^{i\theta_i}$$

so that the wavefunction evolution is

$$i\hbar \frac{1}{2\sqrt{\rho_i}} \frac{d\rho_i}{dt} e^{i\theta_i} - \hbar \frac{d\theta_i}{dt} \sqrt{\rho_i} e^{i\theta_i} = U_i \sqrt{\rho_i} e^{i\theta_i} + K\rho_j e^{i\theta_j}$$

Simplifying and separating real and imaginary parts, we can find equations for $\dot{\rho}_i$ and $\dot{\theta}_i$.

$$\dot{\rho}_i = \frac{2K}{\hbar} \sqrt{\rho_i \rho_j} \sin(\theta_j - \theta_i) \qquad (3.2)$$

$$\dot{\theta}_i = -\frac{U_i}{\hbar} - \frac{K}{\hbar}\sqrt{\frac{\rho_j}{\rho_i}}\cos(\theta_j - \theta_i) \tag{3.3}$$

We can then let $\phi = \theta_2 - \theta_1$. So clearly, $\frac{d\phi}{dt} = \frac{d\theta_2}{dt} - \frac{d\theta_1}{dt}$. This term ϕ represents the phase-difference between the two macroscopic wave-functions. Then (3.3) becomes:

$$\frac{d\phi}{dt} = \frac{U_1 - U_2}{\hbar} + \frac{K}{\hbar}\left(\sqrt{\frac{\rho_2^2 - \rho_1^2}{\rho_1\rho_2}}\right)\cos(\phi) \tag{3.4}$$

We now make the assumption that $|\rho_1| \approx |\rho_2| \approx |\rho_0|$ where ρ_0 is the average electron density of the superconducting material. However, this assumption does not preclude the sign of the $\dot{\rho}_i$ from changing (i.e. the fluctuations are small). This can be explained by the fact that there is a nonzero current across the Junction caused by the potential $V(t)$. The current across the junction should then be proportional to the change in electron density $\dot{\rho}_i$ (note that $\dot{\rho}_i = -\dot{\rho}_j$:

$$I_{\sup} = \frac{2K}{\hbar}\sqrt{\rho_1\rho_2}\sin(\phi) \approx \frac{2K}{\hbar}\rho_0\sin(\phi) = I_c\sin(\phi) \tag{3.5}$$

Here, I_c is referred to as the critical current of the junction. The electrical potential difference across the junction is $V(t)$. So for a cooper pair with charge $q = 2e$, the potential energy difference across the junction is $qV(t) = U_1 - U_2$.

From (3.4) we have (including the assumption of the fixed magnitude of ρ_i):

$$\frac{d\phi}{dt} = \frac{2eV(t)}{\hbar} \Rightarrow V(t) = \frac{\hbar}{2e}\frac{d\phi}{dt} \Rightarrow \frac{dV}{dt} = \frac{\hbar}{2e}\frac{d\phi}{dt}.$$

Now we will assume that the junction also has some capacitance (as it is indeed two conductors with an insulator in between). The current through the junction due to capacitance C should then be

$$I_{cap} = C\frac{dV}{dt} = \frac{\hbar}{2e}\frac{d^2\phi}{dt^2} \tag{3.6}$$

Further, there should be physical imperfections in a real Josephson junction that would allow some conductance $G = \frac{1}{R}$ through the insulator material. The current due to this conductance (i.e. resistive shunt) should be

$$I_{res} = GV = \frac{V}{R} = \frac{\hbar}{2eR}\frac{d\phi}{dt}. \tag{3.7}$$

Then the total current through the junction can be written as the sum of the tunneling-force-induced current (3.5), the capacitive contribution (3.6), and the resistive contribution (3.7):

$$I_{in} = I_c + I_r + I_s = C\frac{dV}{dt} + \frac{1}{R}V + I_c \sin(\phi)$$

In terms of the phase variable ϕ, this becomes

$$C\frac{\hbar}{2e}\frac{d^2\phi}{dt^2} + \frac{1}{R}\frac{\hbar}{2e}\frac{d\phi}{dt} + I_c \sin\phi = I_{in}$$

This equation describes the relationship between a classical observable, I_{in} which is the current through the junction, and the quantum phase variable ϕ.

Inductively coupled Josephson junctions

In this work, we use inductively coupled junctions. Therefore, it is necessary to show how coupling can be performed between junctions that are coupled via an inductor. We suppose that there are two Josephson junctions, independently biased, that are connected by an inductor. Each end of the inductor is connected to a terminal of one of the Josephson junctions such that the voltage across an inductor that connects junction i and j is (from current-voltage relations of inductors):

$$V_j - V_i = L\frac{dI_{ij}}{dt}$$

which means that the current flowing into the ith junction from the jth junction, I_{ij} is

$$I_{ij} = \frac{1}{L}\int (V_j - V_i)dt = \frac{\hbar}{2eL}\int (\frac{d\phi_j}{dt} - \frac{d\phi_i}{dt})\,dt = \frac{\hbar}{2eL}(\phi_j - \phi_i)$$

Since I_{ij} contributes to the 'input' current through the Josephson junction (the current to which the junction phase reacts), the current and voltage dynamics across the junction i are

$$I_{in,i} + I_{ij} = I_{in,i} + \frac{1}{L}\int (V_j - V_i)dt = C\frac{dV_i}{dt} + \frac{1}{R}V_i + I_c \sin\phi_i$$

In terms of the phase, this is

$$C\frac{\hbar}{2e}\frac{d^2\phi_i}{dt^2} + \frac{1}{R}\frac{\hbar}{2e}\frac{d\phi_i}{dt} + I_c \sin\phi_i = \frac{\hbar}{2eL}(\phi_j - \phi_i) + I_{in,i}$$

If we then suppose that the junction is inductively coupled to many junctions, we can write the equations of motion for a set of inductively coupled junctions as:

$$C\frac{\hbar}{2e}\frac{d^2\phi_i}{dt^2} + \frac{1}{R}\frac{\hbar}{2e}\frac{d\phi_i}{dt} + I_c \sin\phi_i = I_{in,i} + \sum_{j\neq i}\frac{\hbar}{2eL_{ij}}(\phi_j - \phi_i)$$

where $L_{ij} = L_{ji}$ is the inductance of the inductor connecting the i and j junctions.

3.3 A ternary memory circuit

Superconducting digital logic circuits show promise in advancing high performance computing[165], [177]. However, design of superconducting random access memory (RAM) that can store and recall data as efficiently as logic operations take place is still a largely unsolved problem [164]. Proposed solutions to this problem include magnetic RAM designs involving using magnetic Josephson junctions[178]–[180], hybrid superconducting-CMOS designs[168], [181], and others [163]. The key challenges associated with developing a functional RAM are reducing power dissipation, increasing memory read/write speed, and reducing chip size [162]–[164].

Memory units of up to 4kb have been demonstrated using SFQ-based designs [167], [169], [170]. However, it has been difficult to build units larger than this because of energy dissipation and memory access problems [170]. For instance, the memory cells used in the most successful cryogenic RAM designs [167], [170] are based on the vortex transition cell [182]. This cell is limited by the fact that it takes a bipolar control current (i.e. the current inputs need to have both positive and negative peaks), which requires some extra peripheral processing to interface with most unipolar cryogenic logic circuits. Hybrid superconducting-CMOS designs interface between the SFQ circuitry and room-temperature CMOS circuitry[168], [181]. However, this approach introduces a significant amount of latency for memory access [168].

The largest source of power consumption in SFQ-based memory systems currently is known to not be simply the memory cell itself, but rather peripheral circuits that access memory [169], [170], [183], [184]. It therefore may be useful to consider designs that allow for less peripheral circuitry for memory cells. A memory cell that holds more than two states could be such a design, since it allows the same amount of peripheral circuitry to be connected to a unit with more information capacity. Radix 3 number systems are theoretically the most efficient (of integer radix) for digital representation of numbers[185]. Assuming that a trit does not require more energy to operate than a bit of the same type, this means that the trit should be significantly more energy efficient as a memory storage unit than a bit. Ternary memory units [186] and peripheral circuitry based on these units [187], [188] have been proposed for Josephson junctions, however these are not currently being developed.

In this paper, we present a ternary memory cell based on three coupled Josephson junctions. We show how a memory cell can be designed and present the dynamics of the cells from WRspice simulations [189]. This cell is very similar in design to recent binary memory designs [159], [160], [190]. Reading and writing can be performed using SFQ pulses to change the states and trigger output from the cell for reading the state.

The cell we present operates such that it is possible to access any state from any other state with a single pulse. A diagram of the states and possible transitions between the states is shown in Figure 3.1. The memory cell is such that in order to write a state into the cell, it is not necessary to know the previous state of the cell. Further, we will show that reading the state can be accomplished by writing '0.'

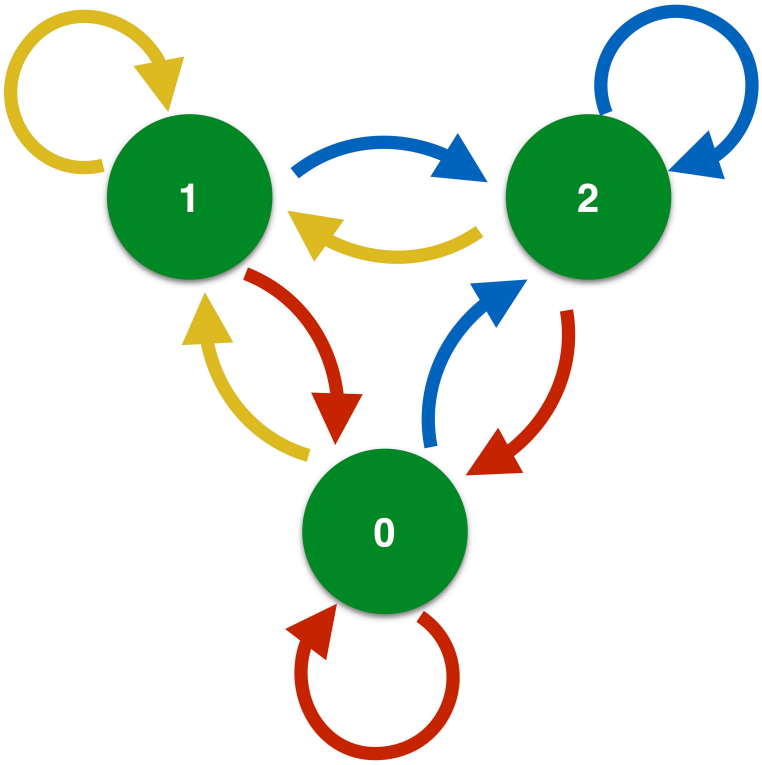


Figure 3.1. State transition diagram for a trit. Red arrows correspond to the 'write 0' command, golden arrows correspond to the 'write 1' command, and blue arrows correspond to the 'write 2' command. Each state is accessible from any other state and can overwrite itself.

Memory cell operation

In Figure 3.2 we present the schematic of the ternary memory cell. In this system, the component parameters are chosen in agreement with the SFQ5ee process[191]. The junction diameter is $1\mu\mathrm{m}^2$ so that the critical current is $I_c = .1\mathrm{mA}$, the gap voltage is $\Delta V = .08\mathrm{mV}$, the subgap resistance is $R_{sg} = 144\Omega$, the junction resistance is $R_N = 16\Omega$, and the junction capacitance is $C_N = 0.07\mathrm{pF}$. This circuit is designed for SFQ pulses with 2ps pulse-width as the inputs. State

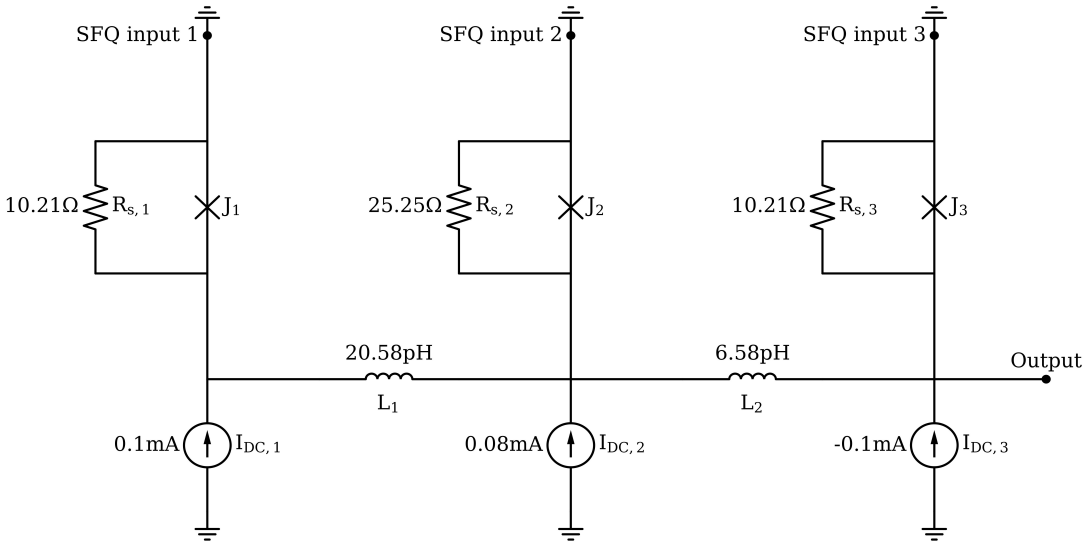


Figure 3.2. A ternary memory cell based on three inductively coupled Josephson junctions. The appropriate inputs for this circuit are SFQ pulses of 2ps width. Note that the shunt resistances $R_{s,i}$ specify only the *added* parallel resistances to the junctions, which include default resistance and capacitances.

transitions between 0, 1, and 2 states are achieved by sending SFQ pulses into the input terminals.

The dynamics of voltage across a small Josephson junction of the type we consider in this paper follow the resistively shunted junction (RSJ) model:

$$\begin{aligned} &C_N \frac{dV}{dt} + \frac{1}{R(V)} V + I_c \sin(\phi) \\ &= C_N \frac{\hbar}{2e} \ddot{\phi} + \frac{\hbar}{2eR(V)} \dot{\phi} + I_c \sin(\phi) = I_{in} \end{aligned} \tag{3.8}$$

where $R(V)$ is a piecewise linear resistance[192]:

$$R(V) = \begin{cases} \dfrac{R_s R_{sg}}{R_s + R_{sg}} & \text{if} \quad V < \Delta V \\ \dfrac{R_s R_N}{R_s + R_N} & \text{if} \quad V > \Delta V \end{cases}$$

The inductive coupling shown in Figure 3.2 is part of the I_{in} term in Equation (3.8). The current from junction j into junction i is then

$$I_{ij} = \frac{1}{L_{ij}} \int (V_j - V_i) dt = \frac{\hbar}{2eL_{ij}} \int (\dot{\phi}_j - \dot{\phi}_i) dt = \frac{\hbar}{2eL_{ij}} (\phi_j - \phi_i) \tag{3.9}$$

so that the junctions are coupled by their phase differences such that the full equations of motion are:

$$\begin{aligned} &C_{N,1} \frac{\hbar}{2e} \ddot{\phi}_1 + \frac{\hbar}{2eR_1(V)} \dot{\phi}_1 + I_c \sin(\phi_1) = I_{in,1} + I_{DC,1} + \frac{\hbar}{2eL_{12}} (\phi_2 - \phi_1) \\ &C_{N,2} \frac{\hbar}{2e} \ddot{\phi}_2 + \frac{\hbar}{2eR_2(V)} \dot{\phi}_2 + I_c \sin(\phi_2) = I_{in,2} + I_{DC,2} + \frac{\hbar}{2eL_{12}} (\phi_1 - \phi_2) + \frac{\hbar}{2eL_{23}} (\phi_3 - \phi_2) \\ &C_{N,3} \frac{\hbar}{2e} \ddot{\phi}_3 + \frac{\hbar}{2eR_3(V)} \dot{\phi}_3 + I_c \sin(\phi_3) = I_{in,3} + I_{DC,3} + \frac{\hbar}{2eL_{23}} (\phi_2 - \phi_3) \end{aligned} \tag{3.10}$$

where $I_{in,i}$ is the current from the SFQ input shown in Figure 3.2 and $I_{DC,i}$ is the bias current. The memory states for this memory cell are fixed-point solutions of (3.10). Each state is a solution of junction phases (ϕ_1, ϕ_2, ϕ_3) such that the currents through the coupling inductors, as described in (3.9) is non-zero. The memories are therefore stored as states of the zero-voltage super-current frozen between the junctions.

Since the fixed-point states are stable at zero voltage (below the gap voltage), we can simply use the sub-gap resistance and shunt resistance values instead of the piecewise linear resistance function (which is still included in all simulations in this paper). We can therefore consider the simplified non-dimensionalized

equations shown in Equation (3.11). The non-dimensional equations of motion for this system are then:

$$\begin{aligned}
&\ddot{\phi}_1 + \gamma_1\dot{\phi}_1 + \sin(\phi_1) = i_{DC,1} + i_{in,1} + \kappa_1(\phi_2 - \phi_1) \\
&\ddot{\phi}_2 + \gamma_2\dot{\phi}_2 + \sin(\phi_2) = i_{DC,2} + i_{in,2} + \kappa_1(\phi_1 - \phi_2) + \kappa_2(\phi_3 - \phi_2) \\
&\ddot{\phi}_3 + \gamma_3\dot{\phi}_3 + \sin(\phi_3) = i_{DC,3} + i_{in,3} + \kappa_2(\phi_2 - \phi_3)
\end{aligned} \tag{3.11}$$

where the non-dimensionalized parameters are $\kappa_i = \frac{\hbar}{2eI_cL_i}$, $i_{DC,i} = I_{DC,i}/I_c$, $\gamma_i = \sqrt{\frac{\hbar}{2eI_cC_N}}(R_{sg}^{-1} + R_{s,i}^{-1})$. The time-derivatives are with respect to the non-dimensionalized time $\tau = \sqrt{\frac{2eJ_c}{\hbar C_N}}t$. To find the fixed-points, we can set the derivatives and time-dependent terms to zero and solve for solutions (ϕ_1, ϕ_2, ϕ_3):

$$\begin{aligned}
&\sin(\phi_1) = i_{DC,1} + \kappa_1(\phi_2 - \phi_1) \\
&\sin(\phi_2) = i_{DC,2} + \kappa_1(\phi_2 - \phi_1) + \kappa_2(\phi_3 - \phi_2) \\
&\sin(\phi_3) = i_{DC,3} + \kappa_2(\phi_2 - \phi_3)
\end{aligned} \tag{3.12}$$

The stable solutions of (3.12) are the memory states. As in [159], [160], [190], the solutions are not exactly at these phase values, but simply close to these values. For our parameters, there are three exponentially stable states. A state for this system can be defined by a vector three integers, one for each junction, (n_1, n_2, n_3) where the phase of the ith junction is $\phi_i = 2\pi n_i + \theta_i$. Here, $|\theta_i| < \pi$ such that θ_i is the phase of the ith junction relative to its own sinusoidal potential well. In this paper, we will consider three stable states: $(0,0,0)$, $(1,0,0)$, and $(1,1,0)$. We will denote the $(0,0,0)$ state as '0,' the $(1,0,0)$ as '1,' and the $(1,1,0)$ state as '2.'

We present the details of these solutions in Table 1 (calculated by numerically solving (3.12)). Determining stability of a solution is done by diagonalizing the Jacobian matrix of (3.11) evaluated at the solution and checking if the eigenvalues have negative real part. The solutions we describe all can be shown to be exponentially stable.

Each of the fixed-points in Table 3.1 is robust to some variations in bias current. In order to be physically realizable the solutions must exist if there are small errors in current. However, when there is a spike in bias current (as in a read or write function) the solutions should destabilize so that the state can change. We show how the solutions become unstable with variations in bias currents in Figure 3.3. The DC current parameters we have chosen for this system ensure

Table 3.1. Properties of fixed-point states of the circuit

State label	(n_1, n_2, n_3)	$\phi_1 / 2\pi$	$\phi_2 / 2\pi$	$\phi_3 / 2\pi$	Current across L_1	Current across L_2	Write command
0	(0,0,0)	0.1757	0.0691	–0.0858	$10.71\mu A$	$48.66\mu A$	2ps SFQ pulse to input 3
1	(1,0,0)	1.0251	0.1857	–0.0446	$84.32\mu A$	$72.36\mu A$	2ps SFQ pulse to input 1
2	(1,1,0)	1.1248	0.8321	0.2071	$29.40\mu A$	$196.38\mu A$	2ps SFQ pulse to input 2

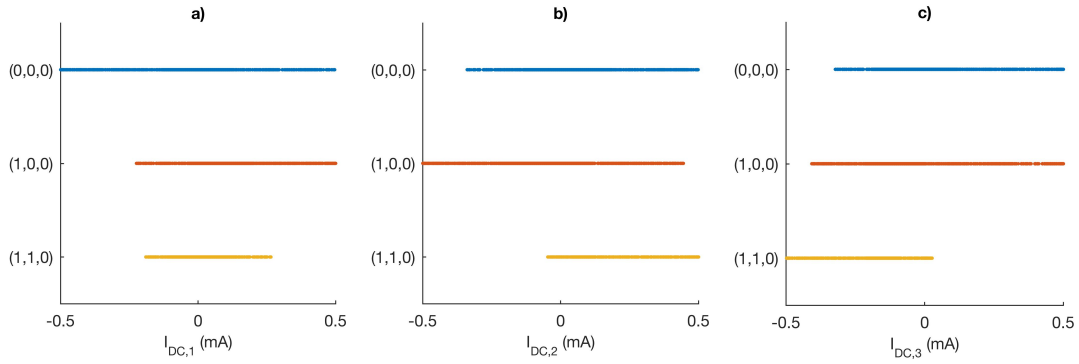


Figure 3.3. Regions of stability are plotted for three states as the DC bias current is varied (one at a time) for each junction. The parameters we have chosen ($I_{DC,1} = 0.1\text{mA}$, $I_{DC,2} = 0.08\text{mA}$, and $I_{DC,3} = -0.1\text{mA}$) are such that small variances in DC (on the order of 0.05mA) should not destabilize any state.

that if the DC currents vary within 50% of their values, the three states should exist and be stable.

To write the '0' state, a 2ps SFQ pulse is sent into the SFQ input 3 (i.e. the right-most junction). In Figure 3.4, we show results from WRspice simulations of how the 2ps SFQ pulse changes the phase relationships between the three junctions. We plot the phase differences with respect to that of the second (center) junction (scaled by 2π). In Figure 3.4(a) the initial condition of the circuit is the '0' state, where there is $10.71\mu A$ stored in L_1 and $48.66\mu A$ stored in L_2 and all junctions are in the zero phase potential well, i.e. the state is (0,0,0). When a pulse is sent to the third junction, there is transient behavior in the circuit, but the state does not change. In Figure 3.4(b), the initial condition of the circuit is the '1' state, where there is $84.32\mu A$ in L_1 and $72.36\mu A$ in L_2 and the first junction has a phase of approximately 2π with respect to the other two junctions, i.e. the state is (1,0,0). When a pulse is sent to the third junction, the transient behavior results in a change of state back to the '0,' which is (0,0,0). In Figure 3.4(c), the initial condition of the circuit is in the '2' state, where there is $29.40\mu A$ in L_1 and $196.38\mu A$ in L_2 and the first two junctions have approximately 2π phase difference with respect to the third junction. When a pulse is sent to the third junction, the third junction's phase is shifted by approximately 2π resulting in a change of state to the (0,0,0) or '0' state.

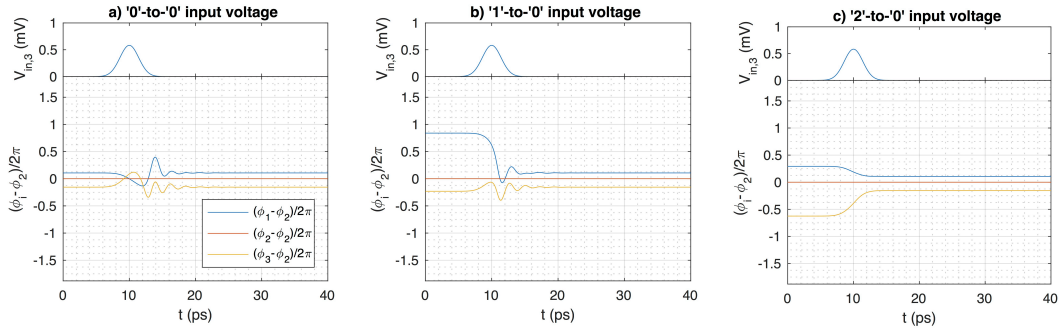


Figure 3.4. The input voltages are plotted above phases relative to that of the second junction for the command to write '0.' Writing '0' is accomplished by sending an SFQ pulse into the third junction in the circuit. The time-series are generated from WRSpice simulations.

To write the '1' state, a 2ps SFQ pulse is sent into the SFQ input 1 (i.e. the left-most junction). In Figure 3.5, we show how the 2ps SFQ pulse changes the phase relationships between the three junctions. In Figure 3.5(a) the initial condition of the circuit is the (0,0,0) or '0' state, where the phases are all close to zero. When a pulse is sent to the first junction, the phase in the first junction is

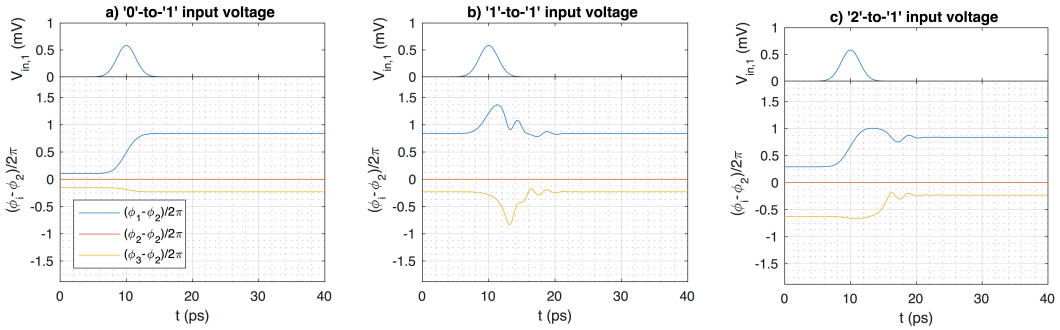


Figure 3.5. The input voltages are plotted above phases relative to that of the second junction for the command to write ‘1.’ Writing ‘1’ is accomplished by sending an SFQ pulse into the first junction in the circuit. The time-series are generated from WRSpice simulations.

shifted by approximately 2π and the state changes to the (1,0,0) or '1' state. In Figure 3.5(b), the initial condition of the circuit is the '1' state. When a pulse is sent to the first junction, there is transient behavior, but it does not result in a change of state. In Figure 3.5(c), the initial condition of the circuit is in the (1,1,0) or '2' state. When a pulse is sent to the first junction, the transient behavior results in a change of state to the (1,0,0) or '1' state.

To write the '2' state, a 2ps SFQ pulse is sent into the SFQ input 2 (i.e. the middle junction). In Figure 3.6, we show how the 2ps SFQ pulse changes the phase relationships between the junctions in the circuit. In Figure 3.6(a) the initial condition of the circuit is the '0' state. When a pulse is sent to the middle junction, the phase of the second junction is shifted by approximately 2π and the phase of the first junction follows, leading to the (1,1,0) or '2' state. In Figure 3.6(b), the

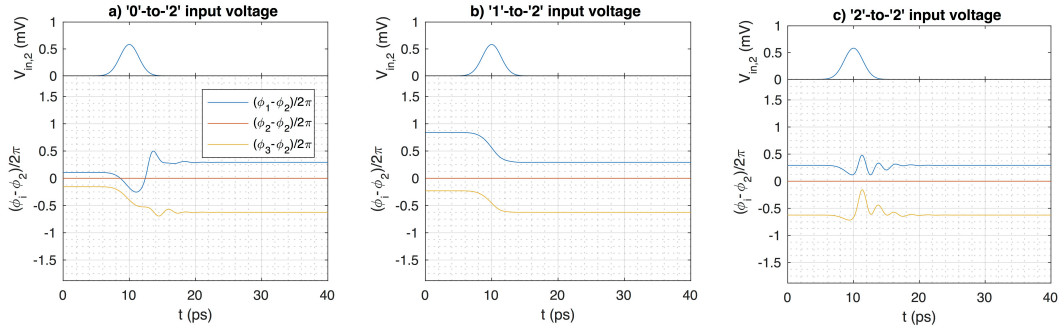


Figure 3.6. The input voltages are plotted above phases relative to that of the second junction for the command to write '2.' Writing '2' is accomplished by sending an SFQ pulse into the middle junction in the circuit. The time-series are generated from WRSpice simulations.

initial condition of the circuit is the '1' state. When a pulse is sent to the middle junction, the phase of the junction is shifted by approximately 2π placing the system into the (1,1,0) or '2' state. In Figure 3.6(c), the initial condition of the circuit is already in the '2' state. When a pulse is sent to the middle junction, there is transient behavior, but it does not lead to a state change.

A destructive read function can be implemented by simply using one of the write functions. It is possible to use any of the three write functions as a read function, but it seems like using the write '0' command is optimal since it results in output pulses of the largest variety. We show the outputs (i.e. the voltage measured at the output node of the circuit) of WRspice simulations for reading using each of the write commands in Figure 3.7.

In order for this system to be suitable for computing, the energy of switching should be sufficiently low. We can calculate the switching energy for a state

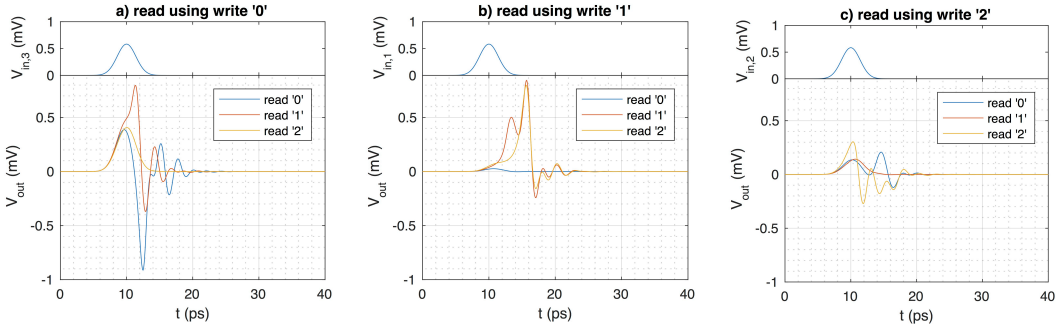


Figure 3.7. The input voltages are plotted above the resulting output voltages. In (a) a 2ps SFQ pulse is sent into the third junction for the write ‘0’ command and the output is plotted for simulations with initial condition in the ‘0,’ ‘1,’ and ‘2’ states. In (b) a 2ps SFQ pulse is sent into the first junction for the write ‘1’ command and the output is plotted for simulations with initial condition in the ‘0,’ ‘1,’ and ‘2’ states. In (c) a 2ps SFQ pulse is sent into the second junction for the write ‘2’ command and the output is plotted for simulations with initial condition in the ‘0,’ ‘1,’ and ‘2’ states.

transition using the following integral:

$$E_{switch} = \sum_{j=1}^{3} \int_{state1}^{state2} |V_j| |I_j| dt$$

We numerically calculate the integral from WRSpice simulations. The energies are reported in Table 3.2. Note that this a measure of the energy dissipated during the switching process in the circuit.

Table 3.2. Numerically calculated access energies for all possible state transitions of the circuit. These values were calculated from WRspice simulations.

	Write '0'	Write '1'	Write '2'
Start '0'	.2128 aJ	.1061 aJ	.1215 aJ
Start '1'	.2128 aJ	.0407 aJ	.0959 aJ
Start '2'	.0819 aJ	.0675 aJ	.1872 aJ

We also calculate numerically the access times for switching between states. This is done by measuring the time between the start of a pulse (taken to be 15 ps before the pulse center for a 2ps pulse) and the end of transient behavior in the circuit. The end of transient behavior is numerically defined here as when current values across the inductors have permanently reached within $.1\mu A$ of their steady-state values for the end state. The values are reported in Table 3.3.

Table 3.3. Numerically calculated access times for all possible state transitions of the circuit. These values were calculated from WRspice simulations.

	Write '0'	Write '1'	Write '2'
Start '0'	32.6 ps	20.3 ps	32.4 ps
Start '1'	30.2 ps	32.5 ps	22.2 ps
Start '2'	21.0 ps	32.6 ps	32.7 ps

Non-destructive readout

In this Section we show the principles of how to implement a non-destructive readout (NDRO) for a ternary memory cell. Non-destructive readout principle is based on the premise that the output voltage amplitudes in response to the applied to the memory cell pulses will be different for each memory state, even if the pulse amplitude is too small to change the memory state. Consequently, these differences can be recorded and distinguished by a circuit that read the output voltages. Dependent on the system parameters, the output voltage amplitude differences for different memory states could be small but distinguishable and parameter optimization is required to optimize the cell to its best optimal performance.

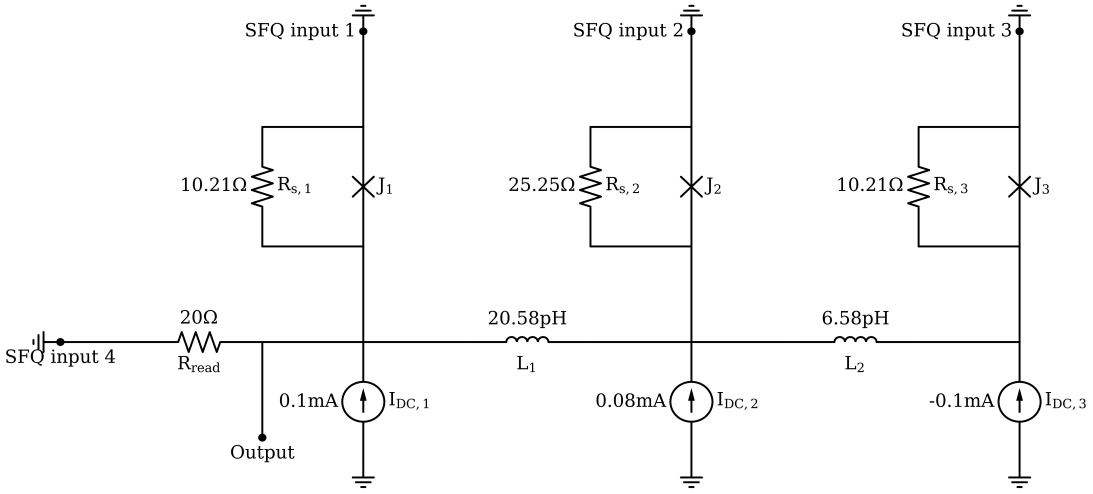


Figure 3.8. A ternary memory cell with NDRO is shown. Write functions and ‘0,’ ‘1,’ and ‘2,’ states are the same as in the DRO circuit, however the read function and output node is different. Reading is accomplished by sending an SFQ pulse (2ps width) into the point labeled ‘SFQ input 4.’

The memory cell circuit is shown in Figure 3.8. This almost is the same circuit as that in Figure 3.2, except it has a fourth input. The resistor between the input and the circuit leads to an attenuation of the input pulse such that the pulse is not strong enough to destabilize the state of the system. The non-destructive read is accomplished by sending an SFQ pulse of 2ps width (the same as used for write functions) into the input labeled ‘SFQ input 4.’

The NDRO works by disturbing the system with a voltage pulse. However the pulse is attenuated by the resistor R_{read} so that it is not large enough to cause any full phase rotations of the junction phases. The behavior of the circuit is plotted in Figure 3.9. When the read pulse is sent, the state (i.e. the current stored in the inductors) does not change after a transient disturbance.

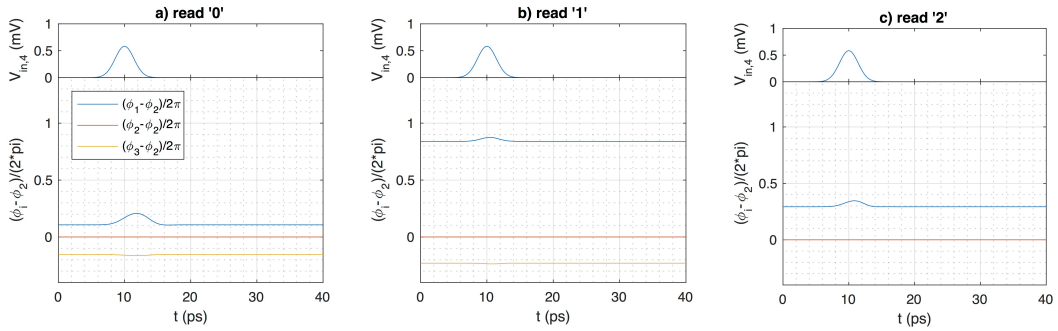


Figure 3.9. The input voltages are plotted above phases relative to that of the second junction. In each plot, an SFQ pulse is sent into the read input node. In (a) the cell is in the ‘0’ state. In (b) the cell is in the ‘1’ state. In (c) the cell is in the ‘2’ state. Note that the states do not change when the pulse is sent. The read function is therefore non-destructive.

To show that the NDRO works as an operational read function, we plot the output voltages measured from the ‘Output’ node in Figure 3.10. From each state, the output voltage has unique amplitude. This ensures that it is possible to read each state without disturbing the state itself. This NDRO is perhaps easier to implement than the DRO for the ternary circuit since each output voltage function has unique amplitude.

Conclusions

We have shown a simple energy-efficient design for a ternary Josephson-junction-based memory cell, described how it operates, and presented the principles upon which it operates. Memory is stored via super-current in the inductors between the Josephson junctions and consequently, via array phase state combinations. Writing a state is accomplished by sending an SFQ pulse

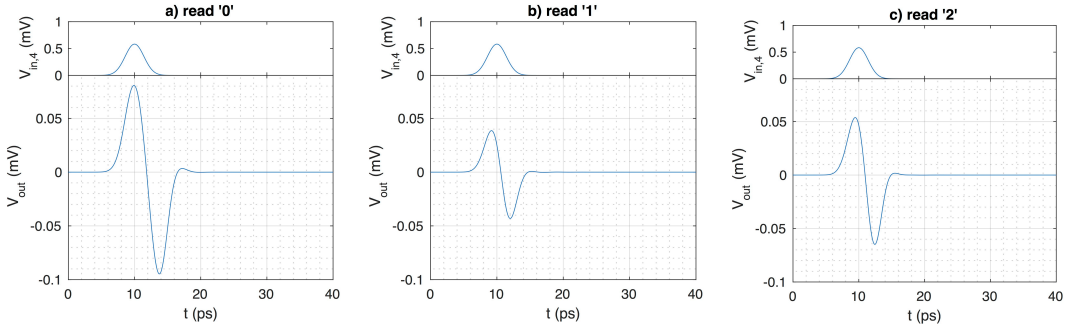


Figure 3.10. The input voltages are plotted above the resulting output voltages. In each plot, an SFQ pulse is sent into the read input node. In (a) the cell is in the ‘0’ state. In (b) the cell is in the ‘1’ state. In (c) the cell is in the ‘2’ state. Note that the resulting output voltage amplitude is different for each state. This ensures that this read function works correctly.

into one of the inputs of the cell. Reading can be accomplished by measuring the output voltage when applying a pulse to any one of the three states. We have further described a possible design for a non-destructive readout for the ternary system. Using these same principles memory cells with larger numbers of states (i.e. N-ary memory) can similarly be designed. For minimization of interconnects and the associated bias currents, higher-state memory state systems could be useful.

CHAPTER FOUR
DISCUSSION

4.1 Coherent beam combining of laser diode arrays

By studying laser arrays using two theoretical approaches, we have found a principle for synchrony of large arrays of semiconductor diode lasers. Though mode selection is not a new phenomenon in laser physics, there has been no way to show how it can occur in weakly coupled semiconductor laser diode arrays. This is largely because the theoretical treatments of these systems (for the purposes of beam combining) have been focused on achieving perfect synchronization between the lasers' phases rather than achieving a stable and coherent collective mode that may not have perfect synchrony. By showing that it is possible to use MSF theory to find stability of non-synchronous modes, we have presented a way to understand whether, and why, and under what conditions a given coupling matrix will allow for a coherent and stable almost-synchronous mode. The results imply that it might be possible to synchronize very large arrays of hundreds or even thousands of lasers using external cavities that can have a decayed non-local coupling structure.

We have also developed a new way to realistically derive the cold-cavity modes of compound resonators (i.e. large external cavity coupled laser arrays) and also developed (but not numerically simulated) a coupled mode theory model using these cold-cavity modes. Further, we have shown how to use this new model to rigorously derive a coupled Lang-Kobayashi model using the rigorously derived cold cavity modes. This should enable studies of more realistic (i.e. experimentally relevant) external cavity designs using the Lang-Kobayashi equations, to augment the large body of knowledge that exists for these equations in which phenomenological matrix representations of external cavities are used.

Since our studies of the Lang-Kobayashi equations showed specifically how modal properties of the cavity affect synchronization properties, an obvious avenue of research would be to theoretically study how fully realistic external cavity designs (such as the self-Fourier or Talbott cavity) work with very large arrays of heterogeneous lasers using the Lang-Kobayashi equations.

In linear dynamical systems, the eigenvalue and eigenvector (or eigenfunction) spectrum—the mode structure—of the time evolution operator are typically the most basic way to understand its properties. However when systems become

nonlinear, it becomes less clear how the eigenvectors are important in the dynamics or whether they are important in the dynamics. Laser physicists have used coupled mode theory to study both the behavior of single lasers and coupled lasers since the beginning of laser physics[193]. There are also mechanical uses of coupled mode type theories, where the vibrational modes of a mechanical system are coupled through nonlinearities[194]. However, little work has been done to understand generically how mode coupling occurs in coupled nonlinear oscillator systems, likely because the presence of nonlinearity in nonlinear oscillators at the surface would seem to preclude using linear analysis. This work done in this part of the dissertation should serve as an example of why it could be useful to understand mode coupling and mode dynamics of coupled nonlinear oscillator systems.

4.2 Cryogenic memory circuits

Though inductively coupled Josephson junction-based circuits are mathematically also coupled nonlinear oscillator systems, they cannot be treated using a coupled mode formulation as with lasers or neurons. In this work, control of these circuits is accomplished by a combination of understanding a circuit's set of fixed-point states and understanding what types of inputs can be used to map between these fixed-point states. The ability to control this switching behavior allowed us to use this type of circuit for binary and ternary memory cell designs. We have presented such a ternary memory cell design in this work, shown that it is robust to imperfections in bias current, presented schematics and operational instructions for both destructive and non-destructive readout versions of the circuit, and shown using WRspice simulations that it can function realistically.

Typically, designs for cryogenic Josephson-junction-based for memory cells rely on single localized fluxons stored in circuit loops or inductors between Josephson junctions. Though the design we present follows this paradigm, it is slightly different because the fluxon is non-local and is stored across the three-junction circuit. This non-locality allows the fluxon to be stored in different ways within the three-junction circuit. Therefore, there can be more than two states that comprise of a single fluxon in the circuit, which allows the system to have three states: one with no stored flux, and two with a single stored fluxon. It follows that in similarly designed arrays of Josephson junctions with more junctions, there might be more ways to store a single fluxon, leading to a larger number of states. If two fluxon states are considered as well as single fluxon states, the possibilities expand further.

The difficulty in designing these more complex circuits would in fact be in read-out and writing. We have still not developed a rigorous way to find read and write functions for each state. While it is very straightforward solve for the stable fixed-

points of the Josephson-junction array, as shown in section 3.2, finding write functions is so far accomplished by trial and error, with only intuition as a guide. If larger (N-ary) circuits were to be designed, it would be useful to have a systematic way to look for write and read functions.

WORKS CITED

[1] N. Nair, E. J. Bochove, A. B. Aceves, M. R. Zunoubi, and Y. Braiman, “Resonator modes and mode dynamics for an external cavity-coupled laser array,” in *Proceedings of SPIE - The International Society for Optical Engineering*, 2015, vol. 9343.
[2] N. Nair, E. Bochove, and Y. Braiman, “Phase-locking of arrays of weakly coupled semiconductor lasers,” *[Forthcoming] Opt. Exp.*, 2018.
[3] N. Nair, E. Bochove, and Y. Braiman, “Transverse Modes of Coupled Nonlinear Oscillator Arrays,” in *Proceedings of the 4th International Conference on Applications in Nonlinear Dynamics (ICAND 2016)*, 2017, pp. 277–288.
[4] N. Nair, E. Bochove, and Y. Braiman, “Associative memory in phasing neuron networks,” in *Proceedings of the 2014 Biomedical Sciences and Engineering Conference - 5th Annual ORNL Biomedical Sciences and Engineering Conference: Collaborative Biomedical Innovations - The Multi-Scale Brain: Spanning Molecular, Cellular, Systems, Cognitive, Behavi*, 2014.
[5] H. Haken, *Synergetics*. Springer-Verlag, 1983.
[6] A. Pikovsky, M. Rosenblum, and J. Kurths, *Synchronization*. Cambridge University Press, 2003.
[7] A. T. Winfree, *The geometry of biological time*. New York: Springer Verlag, 1980.
[8] F. Cucker and S. Smale, “On the mathematics of emergence,” *Japanese J. Math.*, vol. 2, no. 1, pp. 198–227, 2007.
[9] W. Bialek *et al.*, “Statistical mechanics for natural flocks of birds,” *Proc. Natl. Acad. Sci.*, vol. 109, no. 13, pp. 4786–4791, 2012.
[10] K. Tunstrøm, Y. Katz, C. C. Ioannou, C. Huepe, M. J. Lutz, and I. D. Couzin, “Collective States, Multistability and Transitional Behavior in Schooling Fish,” *PLoS Comput. Biol.*, vol. 9, no. 2, 2013.
[11] A. El Hady and B. B. Machta, “Mechanical surface waves accompany action potential propagation,” *Nat. Commun.*, vol. 6, pp. 1–7, 2015.
[12] M. C. Soriano *et al.*, “Complex photonics: Dynamics and applications of delay-coupled semiconductors lasers,” *Rev. Mod. Phys.*, vol. 85, no. 1, pp. 421–470, Mar. 2013.
[13] J. Zamora-Munt, C. Masoller, J. Garcia-Ojalvo, and R. Roy, “Crowd synchrony and quorum sensing in delay-coupled lasers,” *Phys. Rev. Lett.*, vol. 105, no. 26, p. 264101, 2010.
[14] H. Haken, R. Der Agobian, and M. Pauthier, “Theory of laser cascades,” *Phys. Rev.*, vol. 140, no. 2A, 1965.
[15] H. Haken, “Theory of coherence of laser light,” *Phys. Rev. Lett.*, vol. 13, no. 11, pp. 329–331, 1964.
[16] J. Cowan, *Neural Fields*. 2014.

[17] T. Mora and W. Bialek, “Are Biological Systems Poised at Criticality?,” *J. Stat. Phys.*, vol. 144, no. 2, pp. 268–302, 2011.
[18] P. Fries, “A mechanism for cognitive dynamics: Neuronal communication through neuronal coherence,” *Trends Cogn. Sci.*, vol. 9, no. 10, pp. 474–480, 2005.
[19] M. Breakspear, “Dynamic models of large-scale brain activity,” *Nat. Neurosci.*, vol. 20, no. 3, pp. 340–352, 2017.
[20] C. Koch, *Biophysics of Computation: Information Processing in Single Neurons (Computational Neuroscience)*, 1st ed. Oxford University Press, 1998.
[21] V. Rottschafer and B. Krauskopf, “The ECM-backbone of the Lang-Kobayashi equations: a geometric picture,” *Int. J. Bifurc. Chaos*, vol. 17, no. 5, pp. 1575–1588, 2007.
[22] A. K. Jain, K. K. Likharev, J. E. Lukens, and J. E. Sauvageau, “Mutual phase-locking in Josephson junction arrays,” *Phys. Rep.*, vol. 109, no. 6, pp. 309–426, 1984.
[23] Y. Braiman, W. L. Ditto, K. Wiesenfeld, and M. L. Spano, “Disorder-enhanced synchronization,” *Phys. Lett. A*, vol. 206, no. 1–2, pp. 54–60, 1995.
[24] C. Huygens, “Correspondance 1664-1665,” in *Ouvres completes de Christiaan Huygens vol. V*, M. In Nijhoff, Ed. The Hague: La Societe Hollandaise des Sciences, 1893.
[25] J. Pena Ramirez, L. A. Olvera, H. Nijmeijer, and J. Alvarez, “The sympathy of two pendulum clocks: Beyond Huygens’ observations,” *Sci. Rep.*, vol. 6, no. March, pp. 1–16, 2016.
[26] H. M. Oliveira and L. V. Melo, “Huygens synchronization of two clocks,” *Sci. Rep.*, vol. 5, pp. 1–12, 2015.
[27] B. Van Der Pol and J. Van Der Mark, “Frequency Demultiplication,” *Nature*, vol. 120, no. 3019, pp. 363–364, 1927.
[28] J. M. Ginoux and C. Letellier, “Van der Pol and the history of relaxation oscillations: Toward the emergence of a concept,” *Chaos*, vol. 22, no. 2, 2012.
[29] J. W. S. B. Rayleigh, *The Theory of Sound*, no. v. 2. Macmillan, 1896.
[30] H. Bouasse and M. Fouché, *Instruments à vent: par H. Bouasse avec la collaboration expérimentale de M. Fouché*, no. v. 1. Delagrave, 1929.
[31] J. Sawicki, M. Abel, and E. Schöll, “Synchronization of organ pipes,” *Eur. Phys. J. B*, vol. 91, no. 2, pp. 1–6, 2018.
[32] J. Buck and E. Buck, “Biology of synchronous flashing of fireflies,” *Nature*, vol. 211, no. 5049, pp. 562–564, 1966.
[33] S. H. Strogatz and I. Stewart, “Coupled Oscillators and Biological Synchronization,” *Sci. Am.*, vol. 269, no. 6, pp. 102–109, 1993.
[34] J. J. Hopfield, “Neural networks and physical systems with emergent collective computational abilities,” *Proc. Natl. Acad. Sci.*, vol. 79, no. 8, pp. 2554–2558, 1982.

[35] N. Axmacher, F. Mormann, G. Fernández, C. E. Elger, and J. Fell, “Memory formation by neuronal synchronization,” *Brain Res. Rev.*, vol. 52, no. 1, pp. 170–182, 2006.
[36] A. T. Winfree, “Biological rhythms and the behavior of populations of coupled oscillators,” *J. Theor. Biol.*, vol. 16, no. 1, pp. 15–42, 1967.
[37] G. B. Ermentrout, R. F. Galán, and N. N. Urban, “Relating Neural Dynamics to Neural Coding,” *Phys. Rev. Lett.*, vol. 99, no. 24, p. 248103, Dec. 2007.
[38] A. E. Motter, S. A. Myers, M. Anghel, and T. Nishikawa, “Spontaneous synchrony in power-grid networks,” *Nat. Phys.*, vol. 9, no. 3, pp. 191–197, 2013.
[39] B. Liu *et al.*, “Nonlinear dynamics and synchronization of an array of single mode laser diodes in external cavity subject to current modulation,” *Opt. Commun.*, vol. 324, no. 0, pp. 301–310, 2014.
[40] D. J. Watts and S. H. Strogatz, “Collective dynamics of ‘small-world’ networks,” *Nature*, vol. 393, no. 6684, pp. 440–442, 1998.
[41] J. a Yorke and W. N. Anderson, “Predator-Prey Patterns,” *Proc. Natl. Acad. Sci.*, vol. 70, no. 7, pp. 2069–2071, 1973.
[42] J. D. Murray, “On a model for the temporal oscillations in the Belousov-Zhabotinsky reaction,” *J. Chem. Phys.*, vol. 61, no. 9, pp. 3610–3613, 1974.
[43] Y. Kuramoto, *Chemical Oscillatons, Waves, and Turbulence*. Dover Publications Inc., 1984.
[44] T. Y. Fan, “Laser beam combining for high-power, high-radiance sources,” *IEEE J. Sel. Top. Quantum Electron.*, vol. 11, no. 3, pp. 567–577, May 2005.
[45] A. E. Siegman, *Lasers*. University Science Books, 1986.
[46] A. Sanchez-Rubio *et al.*, “Wavelength Beam Combining for Power and Brightness Scaling of Laser Systems,” *Lincoln Lab. J.*, vol. 20, no. 2, p. 15, 2014.
[47] E. J. Bochove, “Theory of spectral beam combining of fiber lasers,” *IEEE J. Quantum Electron.*, vol. 38, no. 5, pp. 432–445, 2002.
[48] M. Haas, A. Killi, C. Tillkorn, S. Ried, M. Ginter, and H. Zimer, “Thin-film filter, wavelength-locked, multi-laser cavity for dense wavelength beam combining of broad-area laser diode bars,” *Opt. Lett.*, vol. 40, no. 17, p. 3949, 2015.
[49] E. Bochove, B. Neschke, N. Nair, P. Delgado, and Y. Braiman, “Phase dynamics of high radiance fiber laser arrays with active phase control,” in *Proceedings of SPIE - The International Society for Optical Engineering*, 2015, vol. 9343.
[50] T. Wu, W. Chang, A. Galvanauskas, and H. Winful, “Model for passive coherent beam combining in fiber laser arrays,” *Opt. Exp.*, vol. 17, no. 22, pp. 19509–19518, 2009.
[51] A. A. Ishaaya, N. Davidson, and A. A. Friesem, “Passive laser beam

combining With intracavity interferometric combiners," *IEEE J. Sel. Top. Quantum Electron.*, vol. 15, no. 2, pp. 301–311, 2009.
[52] C. J. Corcoran and F. Durville, "Passive coherent combination of a diode laser array with 35 elements," *Opt. Express*, vol. 22, no. 7, pp. 8420–8425, Apr. 2014.
[53] C. J. Corcoran and F. Durville, "Passive Phasing in a Coherent Laser Array," *IEEE J. Sel. Top. Quantum Electron.*, vol. 15, no. 2, pp. 294–300, Mar. 2009.
[54] T. Wu, W. Chang, A. Galvanauskas, and H. G. Winful, "Dynamical, bidirectional model for coherent beam combining in passive fiber laser arrays," *Opt. Express*, vol. 18, no. 25, pp. 25873–25886, Dec. 2010.
[55] B. Liu, Y. Liu, and Y. Braiman, "Coherent beam combining of high power broad-area laser diode array with a closed-V-shape external Talbot cavity," *Opt. Express*, vol. 18, no. 7, pp. 7361–7368, Mar. 2010.
[56] M. Sargent, M. O. Scully, and W. E. Lamb, *Laser Physics*. Addison-Wesley, 1974.
[57] M. Spencer and W. Lamb, "Theory of two coupled lasers," *Phys. Rev. A*, vol. 5, no. 2, pp. 893–898, 1972.
[58] R. Lang and K. Kobayashi, "External optical feedback effects on the semiconductor injection laser properties," *IEEE J. Quantum Electron.*, vol. 16, no. 3, pp. 347–355, 1980.
[59] H. G. Winful, "Instability threshold for an array of coupled semiconductor lasers," *Phys. Rev. A*, vol. 46, no. 9, pp. 6093–6094, 1992.
[60] S. Li, Y. Guo, and Y. Braiman, "Synchronizing coupled semiconductor lasers under general coupling topologies," *Am. Control Conf. 2013*, pp. 1231–1236, 2013.
[61] S. Yanchuk, A. Stefanski, T. Kapitaniak, and J. Wojewoda, "Dynamics of an array of mutually coupled semiconductor lasers," *Phys. Rev. E*, vol. 73, no. 1, p. 16209, 2006.
[62] M. Nixon, E. Ronen, A. A. Friesem, and N. Davidson, "Observing geometric frustration with thousands of coupled lasers," *Phys. Rev. Lett.*, vol. 110, no. 18, p. 184102, 2013.
[63] M. Yamada, "Theoretical analysis of nonlinear optical phenomena taking into account the beating vibration of the electron density in semiconductor lasers," *J. Appl. Phys.*, vol. 66, no. 1, pp. 81–89, 1989.
[64] R. Lang, M. O. Scully, and W. E. Lamb, "Why is the laser line so narrow? A theory of single-quasimode laser operation," *Phys. Rev. A*, vol. 7, no. 5, pp. 1788–1797, 1973.
[65] E. Kapon, J. Katz, and A. Yariv, "Supermode analysis of phase-locked arrays of semiconductor lasers," *Opt. Lett.*, vol. 9, no. 4, pp. 125–127, 1984.
[66] C. Cherng and M. Osinski, "Coupled broad-area mode theory of gain-guided laser arrays," *J. Appl. Phys.*, vol. 70, no. 8, pp. 4617–4619, 1991.
[67] M. Lichtner, V. Tronciu, and A. Vladimirov, "Theoretical investigation of

striped and non-striped broad area lasers with off-axis feedback," *IEEE J. Quantum Electron.*, vol. 48, no. 3, pp. 353–360, 2012.
[68] A. Pimenov, G. Kozyreff, V. Z. Tronciu, and A. G. Vladimirov, "Theoretical analysis of a multi-stripe laser array with external off-axis feedback," in *Proc. SPIE 8432, Semiconductor Lasers and Laser Dynamics V*, 2012, vol. 8432.
[69] M. Wrage *et al.*, "Experimental and numerical determination of coupling constant in a multicore fiber," *Opt. Commun.*, vol. 175, no. 1–3, pp. 97–102, 2000.
[70] F. Prati, D. Vecchione, and G. Vendramin, "Frequency locking of supermodes and stability of the out-of-phase-locked state in one-dimensional and two-dimensional arrays of vertical-cavity surface-emitting lasers," *Opt. Lett.*, vol. 22, no. 21, pp. 1633–1635, 1997.
[71] A. Hardy and E. Kapon, "Coupled-mode formulations for parallel-laser resonators with application to vertical-cavity semiconductor-laser arrays," *Opt. Lett.*, vol. 32, no. 6, pp. 966–971, 1996.
[72] H. Erzgräber, S. Wieczorek, B. Krauskopf, H. Erzgraber, S. Weiczorek, and B. Krauskopf, "Dynamics of two laterally coupled semiconductor lasers: Strong- and weak-coupling theory," *Phys. Rev. E*, vol. 78, no. 6, p. 66201, Dec. 2008.
[73] H. Erzgraber, S. Weiczorek, B. Krauskopf, H. Erzgräber, S. Wieczorek, and B. Krauskopf, "Locking of three coupled lasers," in *Proc. SPIE*, 2010, vol. 7597, p. 75971O–75971O–9.
[74] A. Hardy and W. Streifer, "Coupled mode theory of parallel waveguides," *J. Light. Technol.*, vol. 3, no. 5, pp. 1135–1146, 1985.
[75] A. Kireev and T. Graf, "Vector coupled-mode theory of dielectric waveguides," *IEEE J. Quantum Electron.*, vol. 39, no. 7, pp. 866–873, 2003.
[76] T. Pertsch, T. Zentgraf, U. Peschel, A. Bräuer, and F. Lederer, "Anomalous Refraction and Diffraction in Discrete Optical Systems," *Phys. Rev. Lett.*, vol. 88, no. 9, p. 93901, Feb. 2002.
[77] S. Wieczorek and W. W. Chow, "Global view of nonlinear dynamics in coupled-cavity lasers – a bifurcation study," *Opt. Commun.*, vol. 246, no. 4–6, pp. 471–493, 2005.
[78] J. Rogers, S. Peles, and K. Wiesenfeld, "Model for high-gain fiber laser arrays," *IEEE J. Sel. Top. Quantum Electron.*, vol. 41, no. 6, pp. 767–773, 2005.
[79] W. Ray, K. Wiesenfeld, and J. L. Rogers, "Refined fiber laser model," *Phys. Rev. E*, vol. 78, no. 4, p. 46203, 2008.
[80] M. Khajavikhan and J. R. Leger, "Modal analysis of path length sensitivity in superposition architectures for coherent laser beam combining," *IEEE J. Sel. Top. Quantum Electron.*, vol. 15, no. 2, pp. 281–290, Mar. 2009.
[81] J. D. Jackson, *Classical Electrodynamics*, 3rd ed. New York, {NY}: Wiley, 1999.

[82] W. A. Hamel and J. P. Woerdman, “Nonorthogonality of the longitudinal eigenmodes of a laser,” *Phys. Rev. A*, vol. 40, no. 5, pp. 2785–2787, Sep. 1989.
[83] A. E. Siegman, “Orthogonality properties of optical resonator eigenmodes,” *Opt. Comm.*, vol. 31, no. 3, pp. 369–373, 1979.
[84] C. H. Henry, “Theory of the linewidth of semiconductor lasers,” *IEEE J. Quantum Electron.*, vol. 18, no. 2, pp. 259–264, Feb. 1982.
[85] E. J. Bochove and C. J. Corcoran, “In-phase supermode selection in a multicore fiber laser array by means of a self-Fourier external cavity,” *Appl. Opt.*, vol. 46, no. 22, pp. 5009–5018, Aug. 2007.
[86] C. Corcoran and F. Durville, “Experimental demonstration of a phase-locked laser array using a self-fourier cavity,” *Appl. Phys. Lett.*, vol. 86, no. 20, p. 201118, 2005.
[87] A. G. Fox and T. Li, “Resonant modes in a maser interferometer,” *Bell Syst. Tech. J.*, vol. 40, no. 2, pp. 453–488, Mar. 1961.
[88] E. J. Bochove, N. Nair, A. B. Aceves, and M. R. Zunoubi, “New tools for the dynamical description of laser arrays and other complex systems,” in *Proceedings of SPIE - The International Society for Optical Engineering*, 2013, vol. 8885.
[89] J. A. Acebrón, L. L. Bonilla, C. J. P. Vicente, F. Ritort, and R. Spigler, “The Kuramoto Model: A simple paradigm for synchronization phenomena,” *Rev. Mod. Phys.*, vol. 77, no. 1, pp. 137–182, 2005.
[90] L. M. Pecora and T. L. Carroll, “Master Stability Functions for Synchronized Coupled Systems,” *Phys. Rev. Lett.*, vol. 80, no. 10, pp. 2109–2112, 1998.
[91] L. M. Pecora, F. Sorrentino, A. M. Hagerstrom, T. E. Murphy, and R. Roy, “Cluster synchronization and isolated desynchronization in complex networks with symmetries,” *Nat. Commun.*, vol. 5, no. May, pp. 1–8, 2014.
[92] D. Abrams and S. Strogatz, “Chimera states for coupled oscillators,” *Phys. Rev. Lett.*, vol. 93, no. 17, p. 174102, 2004.
[93] T. Dahms, J. Lehnert, and E. Schöll, “Cluster and group synchronization in delay-coupled networks,” *Phys. Rev. E*, vol. 86, no. 1, p. 16202, 2012.
[94] F. Sorrentino, L. M. Pecora, A. M. Hagerstrom, T. E. Murphy, and R. Roy, “Complete characterization of the stability of cluster synchronization in complex dynamical networks,” *Sci. Adv.*, vol. 2, no. 4, 2016.
[95] L. M. Pecora and T. L. Carroll, “Synchronization in chaotic systems,” *Phys. Rev. Lett.*, vol. 64, no. 8, pp. 821–824, Feb. 1990.
[96] J. D. Hart, K. Bansal, T. E. Murphy, and R. Roy, “Experimental observation of chimera and cluster states in a minimal globally coupled network,” *Chaos An Interdiscip. J. Nonlinear Sci.*, vol. 26, no. 9, p. 94801, 2016.
[97] C. R. S. Williams, T. E. Murphy, R. Roy, F. Sorrentino, T. Dahms, and E. Schöll, “Experimental observations of group synchrony in a system of chaotic optoelectronic oscillators,” *Phys. Rev. Lett*, vol. 110, no. 6, p. 64104, 2013.
[98] H. G. Winful and L. Rahman, “Synchronized chaos and spatiotemporal

chaos in arrays of coupled lasers," *Phys. Rev. Lett.*, vol. 65, no. 13, p. 1990, 1990.
[99] R. -d. Li and T. Erneux, "Preferential instability in arrays of coupled lasers," *Phys. Rev. A*, vol. 46, no. 7, pp. 4252–4260, 1992.
[100] B. Kim, N. Li, A. Locquet, and D. S. Citrin, "Experimental bifurcation-cascade diagram of an external-cavity semiconductor laser," *Opt. Exp.*, vol. 22, no. 3, pp. 2348–2357, 2014.
[101] R. L. Davidchack, Y.-C. Lai, A. Gavrielides, and V. Kovanis, "Chaotic transitions and low-frequency fluctuations in semiconductor lasers with optical feedback," *Phys. D*, vol. 145, no. 1, pp. 130–143, 2000.
[102] A. Argyris, M. Bourmpos, and D. Syvridis, "Experimental synchrony of semiconductor lasers in coupled networks," *Opt. Express*, vol. 24, no. 5, pp. 5600–5614, Mar. 2016.
[103] S. H. Strogatz, *Nonlinear Dynamics and Chaos: With Applications to Physics, Biology, Chemistry and Engineering*, vol. 272. Westview Press, 2000.
[104] B. Kim, N. Li, D. Choi, A. Locquet, and D. S. Citrin, "Bifurcation diagram of an external-cavity semiconductor laser: Experiment and theory," *Proc. SPIE - Int. Soc. Opt. Eng.*, vol. 9134, no. 12, pp. 965–972, 2014.
[105] T. Erneux and P. Glorieux, *Laser Dynamics*. Cambridge University Press, 2010.
[106] G. Kozyreff, A. G. Vladimirov, and P. Mandel, "Global coupling with time delay in an array of semiconductor lasers," *Phys. Rev. Lett.*, vol. 85, no. 18, pp. 3809–3812, 2000.
[107] Y. Braiman and K. Wiesenfeld, "Global stabilization of a Josephson-junction array," *Phys. Rev. B*, vol. 49, no. 21, pp. 15223–15226, 1994.
[108] S. Acharyya and R. E. Amritkar, "Synchronization of nearly identical dynamical systems: Size instability," *Phys. Rev. E*, vol. 92, no. 5, p. 52902, 2015.
[109] B. Liu and Y. Braiman, "Coherent beam combining of high power broad-area laser diode array with near diffraction limited beam quality and high power conversion efficiency," *Opt. Express*, vol. 21, no. 25, pp. 31218–31228, Dec. 2013.
[110] B. Liu, P. Colet, and Y. Braiman, "4 - Semiconductor laser beam combining," in *Semiconductor Lasers*, A. Baranov and E. Tourni√©, Eds. Woodhead Publishing, 2013, pp. 121–148.
[111] K. Hirosawa, F. Shohda, T. Yanagisawa, and F. Kannari, "In-phase synchronization of array laser using intra-Talbot-cavity second harmonic generation," *Proc. SPIE*, vol. 9342, pp. 934216–934217, 2015.
[112] B. Liu and Y. Braiman, "Coherent addition of high power broad-area laser diodes with a compact VBG V-shaped external Talbot cavity," *Opt. Commun.*, vol. 414, no. February, pp. 202–206, 2018.
[113] E. Kapon, C. Lindsey, J. Katz, S. Margalit, and A. Yariv, "Coupling mechanism of gainguided integrated semiconductor laser arrays," *Appl.*

Phys. Lett., vol. 44, no. 4, pp. 389–391, Feb. 1984.
[114] R. Waarts, D. Mehuys, D. Nam, D. Welch, W. Streifer, and D. Scifres, “High-power, cw, diffraction-limited, GaAlAs laser diode array in an external Talbot cavity,” *Appl. Phys. Lett.*, vol. 58, no. 23, pp. 2586–2588, 1991.
[115] I. Hassiaoui *et al.*, “Very compact external cavity diffraction-coupled tapered laser diodes,” *Appl. Opt.*, vol. 47, no. 6, pp. 746–750, Feb. 2008.
[116] F. Sorrentino, “Synchronization of hypernetworks of coupled dynamical systems,” *New J. Phys.*, vol. 14, no. 3, p. 33035, 2012.
[117] D. Irving and F. Sorrentino, “Synchronization of dynamical hypernetworks: Dimensionality reduction through simultaneous block-diagonalization of matrices,” *Phys. Rev. E - Stat. Nonlinear, Soft Matter Phys.*, vol. 86, no. 5, pp. 1–8, 2012.
[118] F. Sorrentino and E. Ott, “Network synchronization of groups,” *Phys. Rev. E*, vol. 76, no. 5, p. 56114, 2007.
[119] C. Masoller, “Comparison of the effects of nonlinear gain and weak optical feedback on the dynamics of semiconductor lasers,” *IEEE J. Quantum Electron.*, vol. 33, no. 5, 1997.
[120] G. Agrawal, “Gain nonlinearities in semiconductor lasers: Theory and application to distributed feedback lasers,” *IEEE J. Quantum Electron.*, vol. 23, no. 6, pp. 860–868, Jun. 1987.
[121] C. Masoller, “Implications of how the linewidth enhancement factor is introduced on the Lang and Kobayashi model,” *IEEE J. Quantum Electron.*, vol. 33, no. 5, pp. 795–803, 1997.
[122] M. Soriano, T. Berkvens, G. Van der Sande, G. Verschaffelt, J. Danckaert, and I. Fischer, “Interplay of Current Noise and Delayed Optical Feedback on the Dynamics of Semiconductor Lasers,” *IEEE J. Quantum Electron.*, vol. 47, no. 3, pp. 368–374, 2011.
[123] G. V. M. Yousefi D. Lenstra, M. Yousefi, D. Lenstra, and G. Vemuri, “Carrier Inversion Noise Has Important Influence on the Dynamics of a Semiconductor Laser,” *IEEE J. Sel. Top. Quantum Electron.*, vol. 10, no. 5, pp. 955–960, 2004.
[124] D. Brunner and I. Fischer, “Reconfigurable semiconductor laser networks based on diffractive coupling,” *Opt. Lett.*, vol. 40, no. 16, p. 3854, Aug. 2015.
[125] C. Masoller and N. B. Abraham, “Stability and dynamical properties of the coexisting attractors of an external-cavity semiconductor laser,” *Phys. Rev. A.*, vol. 57, no. 2, pp. 1313–1322, 1998.
[126] J. Mork, B. Tromborg, and J. Mark, “Chaos in semiconductor lasers with optical feedback: theory and experiment,” *IEEE J. Quantum Electron.*, vol. 28, no. 1, pp. 93–108, Jan. 1992.
[127] M. J. Adams, N. Li, B. R. Cemlyn, H. Susanto, and I. D. Henning, “Effects of detuning, gain-guiding, and index antiguiding on the dynamics of two laterally coupled semiconductor lasers,” *Phys. Rev. A*, vol. 95, no. 5, pp. 1–15, 2017.

[128] S. Wang and H. Winful, “Dynamics of phase-locked semiconductor laser arrays,” *Appl. Phys. Lett.*, vol. 52, no. 21, p. 1774, 1988.
[129] M. Nixon, M. Fridman, E. Ronen, A. A. Friesem, N. Davidson, and I. Kanter, “Controlling synchronization in large laser networks,” *Phys. Rev. Lett.*, vol. 108, no. 21, pp. 1–5, 2012.
[130] J. Shena, J. Hizanidis, P. Hövel, and G. P. Tsironis, “Multiclustered chimeras in large semiconductor laser arrays with nonlocal interactions,” *Phys. Rev. E*, vol. 96, no. 3, pp. 3–7, 2017.
[131] J. Shena, J. Hizanidis, V. Kovanis, and G. P. Tsironis, “Turbulent chimeras in large semiconductor laser arrays,” *Sci. Rep.*, vol. 7, no. January, pp. 1–8, 2017.
[132] V. Flunkert, “Lang Kobayashi Laser Equations,” in *Delay-Coupled Complex Systems*, 2011, pp. 111–119.
[133] G. P. Agrawal and N. K. Dutta, *Semiconductor Lasers*, 2nd ed. Boston: Kluwer Academic Publishers, 1993.
[134] R. Lang, “Injection Locking Properties of a Semiconductor Laser,” *IEEE J. Quantum Electron.*, vol. 18, no. 6, pp. 976–983, 1982.
[135] C. J. Corcoran and K. A. Pasch, “Modal analysis of a self-Fourier laser cavity,” *J. Opt. A - Pure Appl. Op.*, vol. 7, no. 5, p. L1, 2005.
[136] A. E. Siegman, “Exact cavity equations for lasers with large output coupling,” *Appl. Phys. Lett.*, vol. 36, no. 6, pp. 412–414, 1980.
[137] A. Singh, S. Jalan, and J. Kurths, “No Title,” *Phys. Rev. E*, vol. 87, no. Rapid Communications, p. 30902, 2013.
[138] R. Suresh, V. Senthilkumar, M. Lakshmanan, and J. Kurths, “No Title,” *Phys. Rev. E*, vol. 86, no. 1, p. 16212, 2012.
[139] F. C. Hoppensteadt and E. M. Izhikevich, “Pattern recognition via synchronization in phase-locked loop neural networks.,” *IEEE Trans. Neural Netw. Learn. Syst.*, vol. 11, no. 3, pp. 734–738, 2000.
[140] T. Heil, I. Fischer, W. Elsässer, J. Mulet, and C. R. Mirasso, “Chaos Synchronization and Spontaneous Symmetry-Breaking in Symmetrically Delay-Coupled Semiconductor Lasers,” *Phys. Rev. Lett.*, vol. 86, no. 5, pp. 795–798, 2001.
[141] I. Fischer, Y. Liu, and P. Davis, “Synchronization of chaotic semiconductor laser dynamics on subnanosecond time scales and its potential for chaos communication,” *Phys. Rev. A*, vol. 62, no. 1, p. 11801, 2000.
[142] T. Deng, G.-Q. Xia, Z.-M. Wu, X.-D. Lin, and J.-G. Wu, “Chaos synchronization in mutually coupled semiconductor lasers with asymmetrical bias currents,” *Opt. Express*, vol. 19, no. 9, pp. 8762–8773, 2011.
[143] M. C. Soriano, F. Ruiz-Oliveras, P. Colet, and C. R. Mirasso, “Synchronization properties of coupled semiconductor lasers subject to filtered optical feedback,” *Phys. Rev. E*, vol. 78, no. 4, p. 46218, 2008.
[144] K. Green and W. T., “No Title,” *J. Comp. Appl. Math.*, vol. 196, pp. 567–578, 2006.

[145] J. L. Hindmarsh and R. M. Rose, “A Model of Neuronal Bursting Using Three Coupled First Order Differential Equations,” *Proc. R. Soc. London. Ser. B, Biol. Sci.*, vol. 221, no. 1222, pp. 87–102, 1984.
[146] S. H. Strogatz, “From Kuramoto to Crawford: exploring the onset of synchronization in populations of coupled oscillators,” *Phys. D*, vol. 143, no. 1–4, pp. 1–20, 2000.
[147] M. A. Schwemmer and T. J. Lewis, “The Theory of Weakly Coupled Oscillators,” in *Phase Response Curves in Neuroscience*, vol. 6, N. W. Schultheiss, A. A. Prinz, and R. J. Butera, Eds. Springer New York, 2012, pp. 3–31.
[148] D. O. Hebb, *The Organization of Behavior: A Neuropsychological Theory*, New. New York: Wiley, 1949.
[149] S. Song, K. D. Miller, and L. F. Abbott, “Competitive {H}ebbian Learning Through Spike-Timing-Dependent Synaptic Plasticity,” *Nat. Neurosci.*, vol. 3, pp. 919–926, 2000.
[150] B. B. Averbeck, P. E. Latham, and A. Pouget, “Neural correlations, population coding and computation,” *Nat Rev Neurosci*, vol. 7, no. 5, pp. 358–366, May 2006.
[151] S. J. Tripathy, K. Padmanabhan, R. C. Gerkin, and N. N. Urban, “Intermediate intrinsic diversity enhances neural population coding,” *Proc. Natl. Acad. Sci.*, vol. 110, no. 20, pp. 8248–8253, 2013.
[152] T. Nishikawa, F. Hoppensteadt, and Y. Lai, “Oscillatory associative memory network with perfect retrieval,” *Phys. D Nonlinear Phenom.*, vol. 197, no. 1–2, pp. 134–148, Oct. 2004.
[153] F. C. Hoppensteadt and E. M. Izhikevich, “Synchronization of laser oscillators, associative memory, and optical neurocomputing,” *Phys. Rev. E*, vol. 62, no. 3, p. 4010, 2000.
[154] D. Psaltis and N. Farhat, “Optical information processing based on an associative-memory model of neural nets with thresholding and feedback,” *Opt. Lett.*, vol. 10, no. 2, pp. 98–100, Feb. 1985.
[155] E. N. Lorenz, “Empirical Orthogonal Functions and Statistical Weather Prediction,” 1956.
[156] J. Hertz, R. G. Palmer, and A. S. Krogh, *Introduction to the Theory of Neural Computation*, 1st ed. Perseus Publishing, 1991.
[157] M. Golubitsky, I. Stewart, P.-L. Buono, and J. J. Collins, “Symmetry in locomotor central pattern generators and animal gaits,” *Nature*, vol. 401, no. 6754, pp. 693–695, Oct. 1999.
[158] K. Friston, J. Phillips, D. Chawla, and C. Büchel, “Nonlinear PCA: Characterizing Interactions between Modes of Brain Activity,” *Philos. Trans. Biol. Sci.*, vol. 355, no. 1393, pp. 135–146, 2000.
[159] Y. Braiman, N. Nair, J. Rezac, and N. Imam, “Memory cell operation based on small Josephson junctions arrays,” *Supercond. Sci. Technol.*, vol. 29, no. 12, p. 124003, 2016.
[160] Y. Braiman, B. Neschke, N. Nair, N. Imam, and R. Glowinski, “Memory

states in small arrays of Josephson junctions," *Phys. Rev. E*, vol. 94, no. 5, 2016.
[161] N. Nair and Y. Braiman, "Ternary memory cell design using small Josephson junction array," *Prep.*, 2018.
[162] M. A. Manheimer, "Cryogenic computing complexity program: Phase 1 introduction," *IEEE Trans. Appl. Supercond.*, vol. 25, no. 3, pp. 10–13, 2015.
[163] D. S. Holmes, A. L. Ripple, and M. A. Manheimer, "Energy-Efficient Superconducting Computing—Power Budgets and Requirements," *IEEE Trans. Appl. Supercond.*, vol. 23, no. 3, pp. 1701610–1701610, 2013.
[164] S. K. Tolpygo, "Superconductor digital electronics: Scalability and energy efficiency issues," *Low Temp. Phys.*, vol. 42, no. 5, pp. 361–379, 2016.
[165] K. K. Likharev and V. K. Semenov, "RSFQ Logic/Memory Family: A New Josephson-Junction Technology for Sub-Terahertz-Clock-Frequency Digital Systems," *IEEE Trans. Appl. Supercond.*, vol. 1, no. 1, pp. 3–28, 1991.
[166] V. K. Semenov, Y. A. Polyakov, and S. K. Tolpygo, "AC-Biased Shift Registers as Fabrication Process Benchmark Circuits and Flux Trapping Diagnostic Tool," *IEEE Trans. Appl. Supercond.*, vol. 27, no. 4, 2017.
[167] S. Nagasawa, Y. Hashimoto, H. Numata, and S. Tahara, "A 380 ps, 9.5 mW Josephson 4-Kbit RAM Operated at a High Bit Yield," *IEEE Trans. Appl. Supercond.*, vol. 5, no. 2, pp. 2447–2452, 1995.
[168] T. Van Duzer *et al.*, "64-kb hybrid Josephson-CMOS 4 Kelvin RAM with 400 ps access time and 12 mW read power," *IEEE Trans. Appl. Supercond.*, vol. 23, no. 3, pp. 8–11, 2013.
[169] S. Nagasawa, H. Numata, Y. Hashimoto, and S. Tahara, "High-frequency clock operation of josephson 256-word x 16-bit rams," *IEEE Trans. Appl. Supercond.*, vol. 9, no. 2 PART 3, pp. 3708–3713, 1999.
[170] T. Ortlepp and T. Van Duzer, "Access Time and Power Dissipation of a Model 256-Bit Single Flux Quantum RAM," *IEEE Trans. Appl. Supercond.*, vol. 24, no. 4, 2014.
[171] R. P. Feynman, R. B. Leighton, and M. Sands, *The Feynman lectures on physics. Vol. 3: Quantum mechanics*. Addison-Wesley Publishing Co., Inc., Reading, Mass.-London, 1965.
[172] B. D. Josephson, "Possible new effects in superconductive tunnelling," *Phys. Lett.*, vol. 1, no. 7, pp. 251–253, 1962.
[173] D. E. McCumber, "Effect of ac impedance on dc voltage-current characteristics of superconductor weak-link junctions," *J. Appl. Phys.*, vol. 39, no. 7, pp. 3113–3118, 1968.
[174] D. E. McCumber, "Tunneling and weak-link superconductor phenomena having potential device applications," *J. Appl. Phys.*, vol. 39, no. 6, pp. 2503–2508, 1968.
[175] K. Gavroglu and Y. Goudaroulis, "Understanding macroscopic quantum phenomena: The history of superfluidity 1941-1955," *Ann. Sci.*, vol. 45, no.

4, pp. 367–385, 1988.
[176] M. Tinkham, *Introduction to Superconductivity: Second Edition*. Dover Publications, 2004.
[177] K. K. Likharev, “Superconductor digital electronics,” *Phys. C Supercond. its Appl.*, vol. 482, pp. 6–18, 2012.
[178] I. V. Vernik *et al.*, “Magnetic josephson junctions with superconducting interlayer for cryogenic memory,” *IEEE Trans. Appl. Supercond.*, vol. 23, no. 3, pp. 1–8, 2013.
[179] B. Baek *et al.*, “Magnetic barrier structures for superconductingmagnetic hybrid Josephson junctions,” *2013 IEEE 14th Int. Electron. Conf. ISEC 2013*, no. 2, pp. 13–15, 2013.
[180] L. Ye *et al.*, “Spin-transfer switching of orthogonal spin-valve devices at cryogenic temperatures,” *J. Appl. Phys.*, vol. 115, no. 17, pp. 10–13, 2014.
[181] O. A. Mukhanov, A. F. Kirichenko, T. V. Filippov, and S. Sarwana, “Hybrid semiconductor-superconductor fast-readout memory for digital RF receivers,” *IEEE Trans. Appl. Supercond.*, vol. 21, no. 3 PART 1, pp. 797–800, 2011.
[182] S. Tahara, I. Ishida, Y. Ajisawa, and Y. Wada, “Experimental vortex transitional nondestructive read-out Josephson memory cell,” *J. Appl. Phys.*, vol. 65, no. 2, pp. 851–856, 1989.
[183] A. F. Kirichenko, I. V Vernik, S. Member, O. A. Mukhanov, and T. A. Ohki, “ERSFQ 4-to-16 Decoder for Energy-Efficient RAM,” vol. 25, no. 3, pp. 4–7, 2015.
[184] W. H. Henkels and H. H. Zappe, “An Experimental 64-Bit Decoded Josephson NDRO Random Access Memory,” *IEEE J. Solid-State Circuits*, vol. 13, no. 5, pp. 591–600, 1978.
[185] S. L. Hurst, “Multiple-Valued Logic: Its Status and its Future,” *IEEE Trans. Comput.*, vol. C-33, no. 12, pp. 1160–1179, 1984.
[186] M. Morisue, J. Endo, T. Morooka, N. Shimizu, and M. Sakamoto, “A Josephson ternary memory circuit,” *Proceedings. 1998 28th IEEE Int. Symp. Mult. Valued Log. (Cat. No.98CB36138)*, vol. 2, pp. 9–11, 1998.
[187] T. Higuchi and M. Kameyama, “Static-Hazard-Free T-Gate for Ternary Memory Element and Its Application to Ternary Counters,” *IEEE Trans. Comput.*, vol. C-26, no. 12, pp. 1212–1221, 1977.
[188] S. Hasuo, “High-speed digital circuits for a Josephson computer,” *[1992] Proc. Twenty-Second Int. Symp. Mult. Log.*, pp. 2–8, 1992.
[189] S. R. Whiteley, “Josephson Junctions in Spice3,” *IEEE Trans. Magn.*, vol. 27, no. 2, pp. 2902–2905, 1991.
[190] J. D. Rezac, N. Imam, and Y. Braiman, “Parameter optimization for transitions between memory states in small arrays of Josephson junctions,” *Phys. A Stat. Mech. its Appl.*, vol. 474, pp. 267–281, 2017.
[191] S. K. Tolpygo, V. Bolkhovsky, T. J. Weir, L. M. Johnson, M. A. Gouker, and W. D. Oliver, “Fabrication Process and Properties of Fully-Planarized Deep-Submicron NbAl-AlOxNB Josephson Junctions for VLSI Circuits,”

IEEE Trans. Appl. Supercond., vol. 25, no. 3, pp. 1–12, 2015.
[192] S. K. Tolpygo *et al.*, “Properties of Unshunted and Resistively Shunted Nb/AlO x -Al/Nb Josephson Junctions With Critical Current Densities from 0.1 mA/μm 2 to 1 mA/μm 2,” *IEEE Trans. Appl. Supercond.*, vol. 27, no. 4, 2016.
[193] W. E. Lamb, “Theory of an Optical Maser,” *Phys. Rev.*, vol. 134, no. 6A, pp. A1429–A1450, 1964.
[194] X. Chen A. and Kareem, “Dynamic Wind Effects on Buildings with 3-D Coupled Modes: Application of HFFB Measurements,” *J. Eng. Mech. ASCE*, vol. 131(11), no. November, pp. 1115–1125, 2005.

VITA

Niketh S. Nair was born in Knoxville, TN. He received his B.S. in 2012 from the University of Pittsburgh with majors in Physics and Mathematics. In the summer of 2012, he began an internship at Oak Ridge National Laboratory under mentorship of Dr. Yehuda Braiman. This internship led to him starting his graduate studies the following year in the Department of Mechanical, Aerospace, and Biomedical Engineering at the University of Tennessee under advisement of his ORNL mentor.